

FINITE ELEMENT MODEL OF STRUCTURES  
WITH PIEZOELECTRIC ELEMENTS

by

**Marcias Martinez M.Eng.**

A thesis submitted to the Faculty of Graduate Studies and Research  
in partial fulfillment of the requirements for the degree of

**Doctor of Philosophy**

Ottawa-Carleton Institute for Mechanical and Aerospace Engineering  
Department of Mechanical and Aerospace Engineering

Carleton University

Ottawa, Ontario

May 2006

© Copyright

2006, Marcias Martinez



Library and  
Archives Canada

Bibliothèque et  
Archives Canada

Published Heritage  
Branch

Direction du  
Patrimoine de l'édition

395 Wellington Street  
Ottawa ON K1A 0N4  
Canada

395, rue Wellington  
Ottawa ON K1A 0N4  
Canada

*Your file* *Votre référence*  
*ISBN: 978-0-494-18225-3*  
*Our file* *Notre référence*  
*ISBN: 978-0-494-18225-3*

#### NOTICE:

The author has granted a non-exclusive license allowing Library and Archives Canada to reproduce, publish, archive, preserve, conserve, communicate to the public by telecommunication or on the Internet, loan, distribute and sell theses worldwide, for commercial or non-commercial purposes, in microform, paper, electronic and/or any other formats.

The author retains copyright ownership and moral rights in this thesis. Neither the thesis nor substantial extracts from it may be printed or otherwise reproduced without the author's permission.

#### AVIS:

L'auteur a accordé une licence non exclusive permettant à la Bibliothèque et Archives Canada de reproduire, publier, archiver, sauvegarder, conserver, transmettre au public par télécommunication ou par l'Internet, prêter, distribuer et vendre des thèses partout dans le monde, à des fins commerciales ou autres, sur support microforme, papier, électronique et/ou autres formats.

L'auteur conserve la propriété du droit d'auteur et des droits moraux qui protègent cette thèse. Ni la thèse ni des extraits substantiels de celle-ci ne doivent être imprimés ou autrement reproduits sans son autorisation.

---

In compliance with the Canadian Privacy Act some supporting forms may have been removed from this thesis.

Conformément à la loi canadienne sur la protection de la vie privée, quelques formulaires secondaires ont été enlevés de cette thèse.

While these forms may be included in the document page count, their removal does not represent any loss of content from the thesis.

Bien que ces formulaires aient inclus dans la pagination, il n'y aura aucun contenu manquant.

  
**Canada**

# CARLETON UNIVERSITY

## Abstract

### FINITE ELEMENT MODEL OF STRUCTURES WITH PIEZOELECTRIC ELEMENTS

by Marcias Martinez

Chairperson of the Supervisory Committee: Dr. A. Artemev  
Department of Mechanical and Aerospace Engineering

A Finite Element Method (FEM) Solver has been developed to analyze three-dimensional structures with piezoelectric materials. Eight and twenty node brick elements, capable of simulating linear elastic and linear piezoelectric structures, are derived. The constitutive equations are presented in this thesis. A linear material matrix is derived from the thermodynamic principles and evaluated for PZT-5A. Our model assumes static conditions and the deformation of the structure occurs due to the effect that the electric field has over the displacement field by means of the polarization of the material. This thesis concentrates on the performance of actuated fiber composites (AFC). The FEM Solver also permits analysis of the sensing mechanisms typically used in piezoelectric structures. The data obtained from the model allow us to optimize the placement of piezoelectric patches on non-metallic matrices. Strain, stress, electric and displacement field are presented and compared to analytical results and experimental data. The use of this FEM solver allows for the understanding of the behavior of piezoelectric materials and actuated fiber composites (AFC) and their applications.

## ACKNOWLEDGMENTS

To my supervisor and friend Prof. Andrei Artemev, who has supported me and contributed to the implementation of this work, making this research a reality. I cannot thank you enough for your dedication and for believing in me even when I did not believe in myself.

I would like to thank my friend, Professor John Goldak, for his valuable knowledge in the area of finite element analysis. Thank you for always having an open door and an answer to my questions.

To Prof. Fred Nitzsche for establishing the relationship with the Swiss Federal Laboratories for Material Testing and Research (EMPA) allowing us to compare our finite element analysis results to experimental values. I would also like to thank Mark Melnykowycz, for sharing his experimental data on actuated fiber composite structures.

I would like to thank my wife for tolerating all the weekends that I spent at the university and not with my family. To my mother who constantly keeps me in her prayers and who kept reminding me that knowledge comes from God who provides it to us, for the service of humanity. I would like to thank all of my family who encouraged and supported me through this work, to which I am very thankful.

## TABLE OF CONTENTS

Abstract .....	iii
Acknowledgments .....	iv
Table of Contents .....	v
List of figures .....	ix
List of Tables .....	xiv
Abreviations .....	xvi
List of symbols .....	xviii
1.0 Introduction .....	1
1.1 Material properties of Piezoelectric & Ferroelectric materials .....	16
1.2 Actuated Composites .....	21
1.2.1 AFC with composite fibers .....	26
1.3 Main types of Piezoelectric Actuators .....	29
1.3.1 Stack Actuators .....	31
1.3.2 Laminar Actuator .....	32
1.3.3 Shear Actuator .....	33
1.3.4 Bimorph Actuator .....	33
1.3.5 Building Block Actuators .....	34
1.3.6 Lever Arm Actuators .....	35
1.3.7 Hydraulic Amplification Actuator .....	36
1.3.8 Flexensional Actuators .....	37
1.3.9 Frequency Leveraged Actuators .....	37

1.4 Summary .....	38
1.5 References for Chapter 1 .....	40
2.0 Introduction .....	46
2.1 Thermodynamics and constitutive relationships of piezoelectric materials.....	46
2.2 Weak Formulation of the Electro-Mechanical Equations .....	59
2.2.1 Mechanical Equilibrium equation.....	59
2.2.2 Electric equilibrium equation .....	60
2.2.3 Electromechanical Constitutive Equation .....	60
2.2.4 Weak formulation of the elastic mechanical equilibrium equation .....	61
2.2.5 Weak formulation of the electrical equilibrium equation.....	62
2.3 Total Weak formulation.....	63
2.4 References for Chapter 2.....	67
3.0 Introduction .....	68
3.1 Element Stiffness Matrix .....	69
3.1.1 The Jacobian Matrix.....	80
3.1.2 Abbreviated Stiffness Matrix .....	83
3.1.3 Unified B-Matrix Definition.....	83
3.2 Integration Scheme.....	84
3.3 Assembly Procedure.....	88
3.4 Application of Boundary Conditions .....	92
3.5 Solving.....	96
3.5.1 Gaussian Elimination with back substitution.....	98
3.5.2 Gauss Jordan elimination .....	99

3.5.3 Sparse Linear Systems.....	101
3.5.3.1 Sparse Matrix memory allocation.....	103
3.5.3.2 Conjugate Gradient Method for Sparse System.....	104
3.6 Post-Processing.....	105
3.6.1 Strain field.....	106
3.6.2 Stress field.....	107
3.7 Summary.....	108
3.8 References for Chapter 3.....	108
4.0 Introduction.....	110
4.1 Patch Test.....	111
4.2 Straight cantilever beam test.....	115
4.3 Flat sheet test.....	118
4.4 Summary of results for elastic problems.....	122
4.5 Validation of piezoelectric elements.....	123
4.5.1 Piezoelectric extension beam.....	124
4.5.2 Piezoelectric shear beam.....	125
4.5.3 Piezoelectric Bimorphic beam.....	126
4.5.4 Piezoelectric sensing problem.....	130
4.5.5 Summary of results for piezoelectric problems.....	132
4.6 References for Chapter 4.....	133
5.0 Introduction.....	134
5.1 FEM models of AFC systems.....	139
5.1.1 Unconstrained AFC with continuous fibers.....	140

5.1.2 AFC symmetrically constrained by GFRP layers (Constrained AFC) with continuous fibers .....	142
5.1.3 Unconstrained AFC with broken fibers (actuation tests) .....	143
5.1.4 Unconstrained AFC with broken fibers (sensing tests).....	145
5.1.5 Bi-layer AFC-GFRP system .....	145
5.1.6 End Constrained AFC.....	146
5.2 Results .....	149
5.2.1 Unconstrained AFC with continuous fibers .....	150
5.2.2 AFC symmetrically constrained by GFRP layers (Constrained AFC) with continuous fibers .....	152
5.2.3 Unconstrained AFC with broken fibers (actuation tests) .....	153
5.2.4 Unconstrained AFC with broken fibers (sensing tests).....	155
5.2.5 Unconstrained AFC with broken fibers model under shear actuation .....	161
5.2.6 Bi-layer AFC-GFRP system .....	163
5.2.7 Analytical model for the deformation of bi-layer system.....	165
5.2.8 End constrained AFC.....	171
5.3 AFC homogenization.....	173
5.4 References for Chapter 5.....	176
6.0 Discussion and Conclusions .....	178
6.1 References of Chapter 6 .....	184

## LIST OF FIGURES

<b>Number</b>	<b>Page</b>
Figure 1.1: Shape Memory Effect .....	3
Figure 1.2: (a-c) One Way Shape Memory Effect, (d-g) Two Way Shape Memory Effect .....	4
Figure 1.3: (a) Magneto Rheological Fluids under no magnetic field, (b) under a magnetic field.	6
Figure 1.4: (a) Magnetostrictive material under a compression load, (b) magnetostrictive material under a magnetic field .....	7
Figure 1.5: Ferroelectric regions. ....	10
Figure 1.6: Poling of a piezoelectric material .....	11
Figure 1.7: Strain vs. Electric Field for a piezoelectric material at the poled domain .....	12
Figure 1.8: Composite Structures .....	15
Figure 1.9: Crystal Structure of barium titanate .....	17
Figure 1.10: Polarization vs. Electric Field Hysteresis Loop .....	18
Figure 1.11: Strain vs. Electric Field in piezoelectric materials .....	19
Figure 1.12: Strain vs. E-field behaviors for various electromechanical ceramics .....	20
Figure 1.13: Simple piezoelectric composite .....	21
Figure 1.14: AFC Components .....	23
Figure 1.15: MFC <sup>TM</sup> piezoelectric fiber sheet fabrication .....	23
Figure 1.16: MFC <sup>TM</sup> Actuator electrode pattern (dimensions in inches) .....	24
Figure 1.17: LaRC MFC <sup>TM</sup> Fabrication .....	25
Figure 1.18: Completed Assembly of LaRC MFC .....	25
Figure 1.19 Manufacturing of Feed rods .....	27

Figure 1.20 Fiber Extrusions .....	27
Figure 1.21: Burnout and Sintering .....	28
Figure 1.22: Electrodes on hollow fiber AFC .....	29
Figure 1.23: Stack Actuator .....	31
Figure 1.24: Laminar Actuation .....	32
Figure 1.25: Shear Actuation .....	33
Figure 1.26: Bimorph Actuation .....	34
Figure 1.27: Building Block Actuation .....	35
Figure 1.28: Stacked Linear Arm .....	36
Figure 1.29: Hydraulic Amplification Actuator .....	36
Figure 1.30: Flextentional Actuator .....	37
Figure 1.31: Frequency Inchworm Actuator .....	38
Figure 2.0: Compliance and Elastic matrix based on the crystal symmetry .....	55
Figure 2.1: Piezoelectric Material Matrix .....	56
Figure 2.2: Material Stiffness Matrix for tetragonal systems .....	58
Figure 3.0: (a) 20 node brick element, (b) 8 node brick element.....	70
Figure 3.1: 8 Node brick shape functions and the sample shape functions for 20-node brick element. ....	71
Figure 3.2: 8 and 20 node brick nodal shape distribution.....	74
Figure 3.3: Jacobian Matrix Transformation .....	81
Figure 3.4: Gauss Numerical Integration .....	85
Figure 3.5: Degree of freedom for a 20-node brick element and 8-node brick element.....	89
Figure 3.6: Assembly Procedure .....	90

Figure 3.7: Topology of a 5-element beam.....	91
Figure 3.8: Global stiffness matrix of a 5 element beam .....	92
Figure 3.9: Sparsity patterns .....	102
Figure 4.1: Patch Test .....	112
Figure 4.2: $\sigma_{xx}$ results on 20-node brick patch test. ....	114
Figure 4.3: $\tau_{xy}$ shear stress on 20-node brick patch test.....	114
Figure 4.4: Straight Cantilever Beam, a) with rectangular elements, b) with trapezoidal elements and c) with parallelogram elements.....	115
Figure 4.5: Shear Simulation with 1,200 8-node brick elements.....	117
Figure 4.6: Flat rectangular plate.....	118
Figure 4.7: Clamped plate under a uniform pressure.....	120
Figure 4.8: Concentrated load on a clamped plate (20-node brick).....	122
Figure 4.9: Laminar actuation . ....	124
Figure 4.10: Shear Actuation Test .....	125
Figure 4.11: Bimorphic actuation beam . ....	127
Figure 4.12: Bimorphic actuation beam. ....	127
Figure 4.13: Applied strain on the element.....	131
Figure 4.14: Electric potential in sensing problem.....	132
Figure 5.1: AFC Geometry, all dimensions in mm . ....	136
Figure 5.2: (a) deflection measurement of AFC on beam, (b) laser triangulation schematic ..	137
Figure 5.3: Clamped AFC setup . ....	138

Figure 5.4: (a) AFC with epoxy matrix, (b) Inner components of AFC, (c) Cross-sectional view of AFC at the electrodes with a 60° contact angle between the electrode and the PZT fiber.....	141
Figure 5.5: GFRP Constrained AFC.....	142
Figure 5.6: Constrained AFC.....	142
Figure 5.7: (a) AFC with transparent GFRP layers, (b) Transparent Kapton and GFRP layer of the constrained AFC.....	143
Figure 5.8: Non-continuous fiber model.....	144
Figure 5.9: AFC on GFRP beam.....	146
Figure 5.10: AFC pulling on a GFRP section of a beam due to an applied voltage.....	146
Figure 5.11: Extended fiber and electrode (deformation not to scale).....	150
Figure 5.12: Electric potential of unconstrained AFC.....	150
Figure 5.13: Computed strain field on unconstrained AFC.....	151
Figure 5.14: Electric potential through the constrained AFC.....	152
Figure 5.15: Strain, $\epsilon_{xx}$ in the constrained AFC at 900Volts.....	153
Figure 5.16: (a) Electric potential on AFC with continuous fibers. (b) Shows the electric potential on an AFC with 5 random 30 $\mu\text{m}$ gaps along the fiber length.....	154
Figure 5.17: The simulated actuation displacement, obtained in an AFC with discontinuous fibers shown as a percentage of displacement obtained in an AFC with continuous fibers, vs. number of gaps.....	155
Figure 5.18: Simulated effect of non-continuous fully polarized fibers on the voltage produced by an AFC under applied deformation.....	156
Figure 5.19: (a) AFC under an applied strain (b) AFC x-section near the gap.....	157

Figure 5.20: (a) AFC under an applied strain with fully polarized along the fiber length and 1 broken fiber. (b) AFC under an applied strain fully polarized along the fiber length and 1 broken fiber with a transparent epoxy matrix. ....	158
Figure 5.21: (a) AFC with 2 broken fibers and with depolarized regions at the gap interfaces with a transparent epoxy (b) AFC with 2 broken fibers and with depolarized region at the gap interfaces with the epoxy.....	159
Figure 5.22: Applied electric potential on AFC for shear actuation. ....	161
Figure 5.23: AFC displacement field, deformed in shear due to an electric field across the fiber diameter.....	162
Figure 5.24: Shear deformation displacement vs. gap fiber presence along the fiber length...	163
Figure 5.25: Displacement field of AFC on a GFRP beam at a 900V.....	164
Figure 5.26: AFC on a GFRP at 900V electric potential field.....	164
Figure 5.27: Strain, $\epsilon_{xx}$ of AFC on beam. ....	165
Figure 5.28: AFC on a lamella .....	166
Figure 5.29: Maximum deflection of an AFC on a Lamella .....	170
Figure 5.30: AFC pulling on GFRP X-Section.....	171
Figure 5.31: Displacement field on the deformed mesh.....	172
Figure 5.32: Effect of non-continuous fibers on displacement of the GFRP beam section...	173
Figure 5.33: RVE of an AFC .....	174
Figure 6.0: Normalized AFC extension and contraction displacement vs. the number of gaps.	183

## LIST OF TABLES

<b>Table No.</b>	<b>Page No.</b>
Table 1.0: Symbols of the 32 point groups in chrsytallography.....	9
Table 1.1: Piezoelectric constants for PZT-5A.....	32
Table 3.0: Gauss Points for an 8-node brick element.....	85
Table 3.1: Gauss Points and weight functions for 20-node brick elements obtained using and one dimensional gauss points and weight for n=3 from.....	87
Table 3.2: Example of strain output at one nodal point.....	107
Table 4.1: Location of the internal nodes in the patch test.....	113
Table 4.2: Straight cantilever beam for 20-node brick elements .....	116
Table 4.3: Straight cantilever beam for 8-node brick elements .....	117
Table 4.4: Displacement at the center of a rectangular plate under uniform pressure/ concentrated load for simple and clamped boundary conditions .....	119
Table 4.5: 8-node brick flat plate under a uniform pressure .....	119
Table 4.6: 20-node brick flat plate under a uniform pressure .....	120
Table 4.7: 8-node brick flat plate under a concentrated load .....	121
Table 4.8: 20 Node Brick under a concentrated load .....	121
Table 4.9: Piezoelectric extension test for 8-node brick elements .....	124
Table 4.10: Piezoelectric extension test 20-node brick elements.....	125
Table 4.11: Piezoelectric extension test 8-node brick elements.....	126
Table 4.12: Piezoelectric extension test 20-node brick elements.....	126

Table 4.13: Piezoelectric bimorphic actuation test .....	128
Table 5.1: Material properties for PZT-5A and epoxy .....	147
Table 5.2: Material properties for copper and negative polarized PZT-5A.....	148
Table 5.3: Material properties for GFRP .....	148
Table 5.4: $\epsilon_{xx}$ strain values computed by the FEM solver and $\epsilon_{xx}$ strain values measured at EMPA for an AFC under free strain conditions .....	151
Table 5.5: Summary of strain for EMPA's constrained AFC .....	153
Table 5.6: Voltage difference along the AFC for piezoelectric fibers poled along the fiber length for polarized and depolarized fibers .....	160
Table 5.7: Shows boundary conditions applied to the RVE in order to compute the effective material properties of the AFC unit cell.....	174

## ABBREVIATIONS

AFCs – Actuated Fiber Composites

Al – Aluminum

ASTM - American Society of Testing and Materials

B.C. – Boundary Conditions

CAD – Computer Aided Design

CCD – Charge Coupled Device

Co – Cobalt

Cu – Copper

DARPA – Defense Advanced Research Project Agency

dof – degrees of freedom

EMPA – Swiss Federal Laboratory for Material Testing and Research

FE – Finite Element

Fe – Iron

FEM – Finite Element Methods

GFRP – Glass Fiber Reinforced Polymer

IDE – Inter-digitized Electrodes

IMS – Intelligent Material Systems

LTS – Laser Triangulation Sensor

Ni – Nickel

Pd – Palladium

Pt –Platinum

PZT – Lead, Zirconium, Titanate (piezoelectric material).

SMA – Shape Memory Alloys

Ti – Titanium

Zn – Zinc

## LIST OF SYMBOLS

$P_s$	polarization
$\mu$	dipole moment per unit volume
$dv$	unit volume
$\varphi$	Voltage
$\Delta$	Piezoelectric Stroke
$C$	Coulomb charge unit
$N$	Unit of force in Newton
$G$	Gibbs free energy
$U$	Internal Energy
$\epsilon$	Strain
$\sigma$	Stress
$D$	Electric displacement
$E$	Electric field
$H$	Magnetic field
$B$	Magnetic induction vector
$\eta$	Entropy
$\theta$	Temperature
$\kappa$	Permittivity
$d$	Piezoelectric constant
$p_m$	Pyroelectric coefficient

$\alpha$	Thermal expansion coefficient
$c$	Specific heat
$C_{ij}$	Material matrix
$\nu$	Poissons ratio
Y.M.	Youngs Modulus of Elasticity
$D$	Unified material matrix
$\nabla \cdot$	Symmetric Divergence operator
$\nabla$	Gradient operator
$\rho$	Density
$u$	displacement vector
$p$	load vector
$\chi$	permittivity constant matrix in strain charge form
$\chi_{total}$	Total weak formulation of the mechanical and electrical equilibrium equation
$\phi$	Electric potential
$\delta\phi$	Virtual electric potential
$\delta u$	Virtual displacement
$V$	Volume
$\Gamma$	Surface
$n$	Normal unit vector
$e$	piezoelectric constant matrix in the stress charge form
$b$	Nodal electrical and body forces

$\bar{C}_{ij}$	Elastic compliance coefficient
$\bar{\kappa}_{mn}$	Permittivities
$\bar{d}_{mj}$	Piezoelectric constant
$\bar{p}_m$	Pyroelectric coefficients
$\alpha_{i\_thermal}$	Thermal Expansion coefficient
<b>D</b>	Unified Material Matrix
$\tau$	Traction force
Ni	Shape Functions
Gx	Derivative in x of the nodal shape functions
Gy	Derivative in y of the nodal shape functions
Gz	Derivative in z of the nodal shape functions
F	Faraday
m	meters
A	Amps
s	Seconds
Kg	Kilograms
C	Coulombs
N	Newton
J	Jacobian operator
det	Determinant operator
I	Moment of Inertia

## Chapter 1

### LITERATURE REVIEW

#### 1.0 Introduction

Intelligent material systems (IMS), also known as smart materials, have the unique properties of being able to modify their behavior in response to a signal. As seen in Figure 1.0, it is the combination of a controller, actuators, materials and sensors that create Intelligent Material Structures. For example, in the semiconductor industry, smart materials are used as valves in mass flow controllers. Many applications have been proposed for the use of smart materials, for example the use of smart materials in the instrumentation industry in the form of pressure transducers [1-4]. In the aerospace industry smart materials have been used for active damping of vibrations in large flexible structures [5-9] and in the biomedical industry, ionic polymer metal composites have been studied as possible materials for the development of artificial muscles [10, 11]. Many other applications of smart materials are currently being studied.

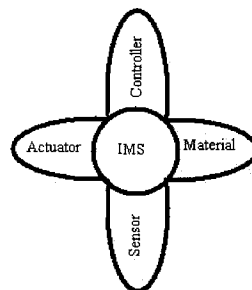


**Figure 1.0:** Intelligent Material Systems [12]

Materials that are commonly used to create IMS are:

- Shape memory alloys (SMA),
- Electro- and Magneto rheological fluids,
- Ionic Polymer Gels,
- Magnetostrictive materials and
- Piezoelectric materials.

In the next few paragraphs we will briefly describe some of these materials.

SMA have been considered for the design of IMS. SMA are materials that have a strong relationship between a temperature field and their deformation field. The shape memory effect relates plastic strain with temperature. Ti-Ni alloy was first discovered in 1963 to have a shape memory effect and super elasticity properties that other metal alloys did not have [13]. Since 1963, other materials with shape memory effects have been discovered, such as, certain copper alloys (Cu-Zn-Al and Cu-Al-Ni), Nitinol (Ni-Ti) and certain ferrous alloys (Fe-Pt, Fe-Pd, Fe-Ni-Co-Ti). SMA, have been investigated for space antenna applications, pipe coupling and recently are being investigated to act as actuators and sensors. An example of shape memory effect consists of a crumpled antenna in the form of a spherical ball that under the presence of solar heat will restore its original shape of a satellite dish. The shape effect occurs due to a martensitic phase transformation [13, 14]. Figure 1.1 describes the martensitic transformation where the parent phase suffers a shear mechanism creating domains **A** and **B** at a critical temperature. Domains **A** and **B** have the same crystallographic structure but different orientation. As seen in Figure 1.1, this mechanism is a diffusionless phase transformation. At a

higher temperature than the critical temperature, if the crystallographic arrangement is reversible (strain below a critical value), the martensite phase transformation becomes unstable reverting back to the parent phase. This reversible arrangement is known as one-way shape memory effect.

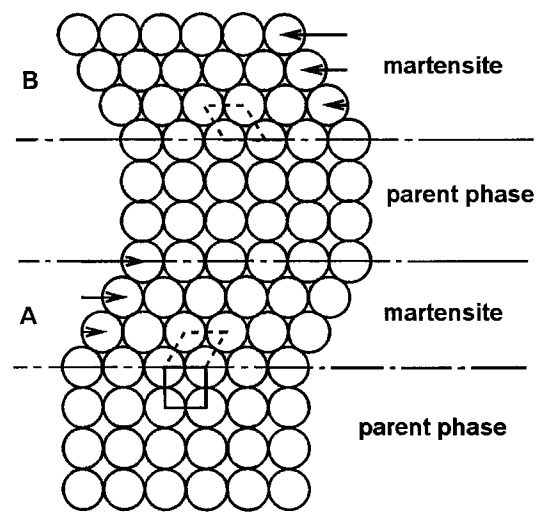


**Figure 1.1:** Shape Memory Effect [13]

Figure 1.2-a-c, shows one-way memory effect. In the one-way shape memory effect a spring, at 293K (figure 1.2-a-c), is applied small stress values (below the introduction of dislocations) followed by a re-heating that will cause it to regain its original shape (figure 1.2-c).

SMA, are also capable of remembering the shape of the martensitic phase transformation under certain conditions. When the applied strain is beyond a critical value (figure 1.2-d), dislocations are introduced into the SMA. When the temperature is raised above the reversed transformation temperature the shape memory alloy does not return to the original parent phase (figure 1.2-e). The induced dislocations are present in the parent phase even after the

reverse transformation heating. If the spring is cooled, the spring will stretch, as shown in figure 1.2-f. If the material is reheated it will take the shape in figure 1.2-g. Now, every time the spring is cooled and re-heated it will remember the shape shown in Fig. 1.2-f and g. This process is known as two-way shape memory effect.

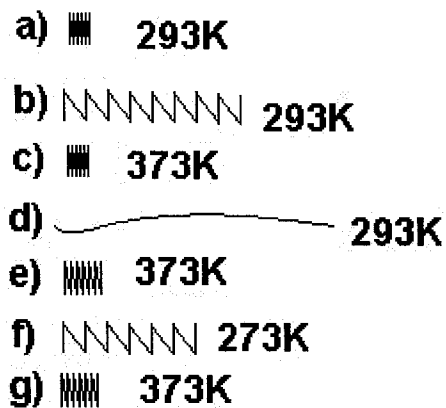


**Figure 1.2:** (a-c) One Way Shape Memory Effect, (d-g) Two Way Shape Memory Effect [13]

Shape memory alloys have proven to show large deformations and forces at low deformation frequencies. Thus, when high deformation frequency application of smart structures is required, SMA, are not necessarily the best choice. The complexity with high deformation frequency applications is mostly due to the difficulty in rapid temperature control changes.

SMA, also have other very unique properties that are still not well understood, an example of this is the rubber-like behavior of SMA. This behavior is described by Otsuka and Wayman as:

“When the alloy is deformed just after the martensitic transformation, the deformation behavior is plastic and it exhibits shape memory effect. However, when the alloy is aged in the

martensitic state for 12 hours or so, it becomes pseudoelastic. As far as the S-S curve is concerned, it is very similar to superelasticity, but it is quite different from the latter in that it occurs solely in the martensitic state.” [13, page 44]

Electro and Magneto rheological fluids are materials that are able to significantly change their rheological behavior under the presence of an electrical or magnetic field. Rheology is the study of deformation and flow of matter. These types of fluids have the capability of changing from a free flowing liquid to a solid under the presence of an electrical or magnetic field. Furthermore, the solids have controllable yield strength, dependent on the strength of the magnetic or electrical field. A typical Magneto rheological fluid consists of a 20-40% by volume of iron particles free floating in a liquid such as water, oil or glycol, as shown in figure 1.3-a. The particles are approximately 3-10 microns in diameter. Under a presence of a magnetic field the particles are aligned as shown in figure 1.3-b, thus creating a semi solid. Magneto rheological fluids have been used in dampers [15].

Winslow initially observed electro rheological effects in 1947, for which sometimes this change, from liquid to solid, is referred to as the Winslow effect [16]. Electro-rheological fluids can change their rheological behavior by creating a series of dipoles that act like chain structures along the direction of the electrical field. Electro and Magneto rheological fluids have the ability to change phase state from liquid to solid and vice versa in a few milliseconds. Electro and Magneto rheological fluids have potential to be a main contributor in the design of IMS for a very large number of engineering applications. Magneto-rheological fluids have many of the same types of rheological changes as Electro-rheological fluids, with the only

exception being that the changes in Magneto-rheological fluids are due to the application of a magnetic field [16].

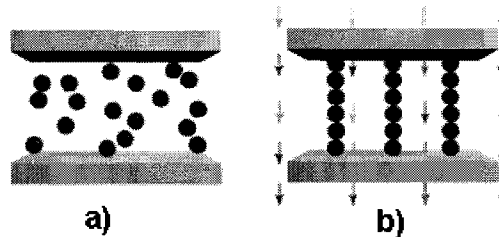


**Figure 1.3:** (a) Magneto Rheological Fluids under no magnetic field, (b) under a magnetic field.

Polymer gels have been considered as possible materials in smart material structures. Polymer gels are defined as three-dimensional networks of cross-linked macromolecular polyelectrolytes. These gels are capable of swelling or shrinking in aqueous solutions under the presence of an alkali or acid solution, respectively [17, 18]. The swelling and shrinking of these gels are due to changes in their environment, for example, a change in the pH of the solution they are immersed in [17,18]. A change in temperature or electric field of the solution has also been found to cause a swelling and/or shrinkage of these polymer gels [19].

Another type of material used in IMS are magnetostrictive materials. Magnetostrictive materials are materials that produce small values of strain when subjected to a magnetic field. Nickel, cobalt and iron are among some of the materials that exhibit magnetostrictive behavior. The magnetostrictive effect in ferromagnetic materials is due primarily to two main processes. The first process involves the displacement of magnetic domains, while the second process involves the rotation of magnetization on the magnetic domains. The two processes produce an overall deformation of the magnetostrictive material. Typical magnetostrictive

materials produce displacements in the range of  $100\mu$ . Recently, new materials have been discovered to have magnetostrictive properties capable of producing displacements in the range of  $1000\mu$ . These new found materials are known as giant magnetostrictive materials. Terfenol-D and  $\text{Ni}_2\text{MnGa}$  are known as giant magnetostrictive materials. These materials exhibit a large magnetostrictive strain under a magnetic field. This strain is induced by a martensitic transformation, near room temperature, induced by crystallographic arrangements as explained above for shape memory alloys. Due to this similarity between magnetostrictive materials and shape memory alloys some magnetostrictive materials are called Magnetic Shape Memory alloys or Ferromagnetic Shape Memory alloys [20-23]. Figure 1.4-a shows a magnetostrictive material under a compression load. The magnetic domains, as seen in this figure, orient themselves perpendicular to the applied compressive load. In figure 1.4-b, the same material is placed under a magnetic field, which causes the magnetic domains to re-align in the same direction as the magnetic field, causing an overall deformation of the magnetostrictive material.

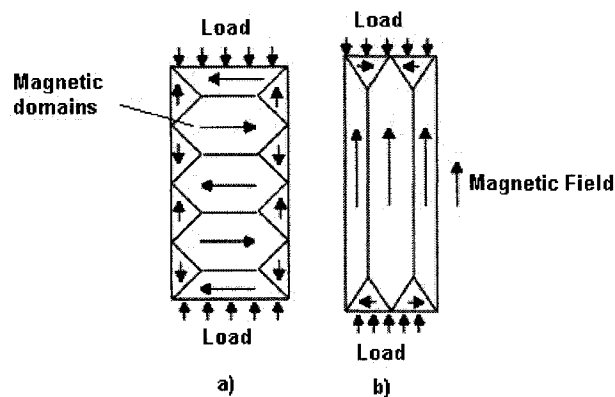


**Figure 1.4:** (a) Magnetostrictive material under a compression load, (b) magnetostrictive material under a magnetic field [24].

Piezoelectric materials are materials that have a link between an electrical field and the deformation field. Two effects can provide such links: piezoelectric and electrostrictive. Piezoelectric materials differ from electrostrictive materials, in that the relationship between the deformation field and the electrical field is linear, while in electrostrictive materials the relationship is quadratic. Piezoelectric materials also have the ability to produce an electrical field when the piezoelectric materials are deformed. Piezoelectric phenomena are closely related to ferroelectric behavior [12].

Piezoelectric effect depends on the lattice structure. It is considered that a crystallographic structure is symmetric when an operation (for example rotation) can be performed on the crystal structure, which does not change the physical parameter that is of interest (for example polarity). Thirty-two microscopic symmetry types (point groups) can summarize the lattice structure for thousands of crystals. The thirty-two crystal symmetries are outlined in Table 1.0. Of these thirty-two crystal symmetries outlined in Table 1.0, eleven are considered to have a center of symmetry. Crystals that have a center of symmetry do not have any polarization (indicated by a dash in Table 1.0). The remaining crystal symmetry groups (twenty one) have one or more unique directions. Two unique crystallographic directions cannot be made to coincide by symmetry operations, such as rotation, reflection mirror, and inversion center operations. A crystal structure that has only one unique direction axis, that does not have any mirror perpendicular to this axis and for which the direction axis is different from each opposite end, is said to be a polar crystal [25].

Polar crystals exhibit spontaneous polarization. These crystal symmetries total twenty, as indicated in the remarks column of Table 1.0. As seen also in the remarks column of Table 1.0,

certain crystals are ferroelectric crystals and have piezoelectric effects, while not all piezoelectric crystals are ferroelectric. Piezoelectric effects are produced due to a charge distribution at the nano-scale. Piezoelectric crystals have an overall charge distribution within the crystal structure creating an electrical dipole. This dipole is produced by a pair of positive and negative ions in the crystal structure with an electrical charge center. The movement of this electrical charge center results in the polarization of the crystal.

Table 1.0: Symbols of the 32-point groups in crystallography [25]

Crystal Systems	International Notation	Schönflies Notation	Remarks $\psi$
Triclinic	1	$C_1$	* +
	1	$C_1(S_2)$	-
Monoclinic	2	$C_2$	* +
	m(2)	$C_s(C_{1h})$	* +
	2/m	$C_{2h}$	-
Orthorhombic	2mm	$C_{2v}$	* +
	222	$D_2(V)$	*
	mmm	$D_{2h}(V_h)$	-
Tetragonal	4	$C_4$	* +
	4	$S_4$	*
	42m	$D_{2d}(V_d)$	*
	422	$D_4$	*
	4mm	$C_{4v}$	* +
	4/m	$C_{4h}$	-
	4/mmm	$D_{4h}$	-
Trigonal	3	$C_3$	* +
	3	$C_{3i}(S_6)$	-
	3m	$C_{3v}$	* +
	32	$D_3$	*
	3m	$D_{3d}$	-
Hexagonal	6	$C_6$	* +
	6	$C_{3h}$	*
	6mm	$C_{6v}$	* +
	6/m	$C_{6h}$	-
	622	$D_6$	*
	6m2	$D_{6h}$	*
	6/mmm	$D_{6h}$	-
Cubic	23	$T$	*
	43m	$T_d$	*
	m3	$T_h$	-
	43	$O$	-
	m3m	$O_h$	-

$\Psi$  The asterisk (\*) indicate that piezoelectric effect may be exhibited while the plus sign (+) indicate that pyroelectric and ferroelectric effects may be exhibited.

In most cases the alignment of dipoles are localized to certain regions of the material, as shown in Figure 1.5, while in other regions the dipoles may be aligned in other directions. A ferroelectric domain is a region of the material where all the dipoles are aligned in the same direction. It has not been clearly determined what causes the formation of these regions but two possible explanations exist. The first is that the domains form as to obtain a state of minimum free energy. The second possible explanation is that the dipoles do not align, due to material imperfections (defects). This second explanation is used in the case when there is no depolarizing field. Depolarization of a piezoelectric material causes the material to have no change in the dimension of the material under the influence of an electrical field.

Polarization can be calculated as follows:

$$P_s = \left( \iiint \mu dv \right) / \text{volume} \quad (1.1)$$

where  $\mu$  is the dipole moment per unit volume [25].

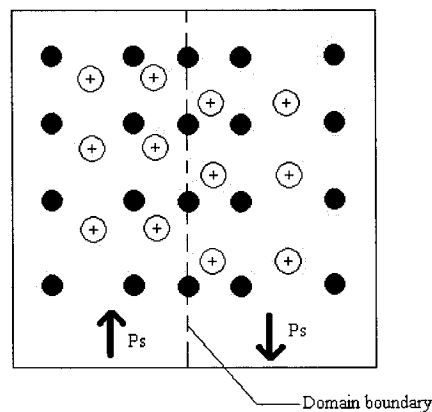


**Figure 1.5:** Ferroelectric regions. [25]

The ferroelectric regions can be observed by the following methods: Polarizing microscope [26,27], chemically etched samples observed by polarizing microscope, [28-30], X-rays [31], power pattern method [33,34] and liquid crystal display [35, 36].

Piezoelectric ceramics are polycrystalline. The domain, indicated by the arrows in figure 1.6-a, in a ceramic have no net polarization. When the ceramic material is placed under a strong electric field, and usually at a temperature below the Curie temperature, the domains align in the direction of the electric field. This alignment of the domains, in the direction of the electric field, is known as poling (figure 1.6-b). The removal of the electric field produces a remanent polarization in the piezoelectric materials close to the same direction as the applied electric field as shown in figure 1.6-c. The poling of piezoelectric materials allows for a change in the dimensions of the material under the influence of an electrical field. This change in dimension is dependent on the poling direction and the strength of the electrical field.

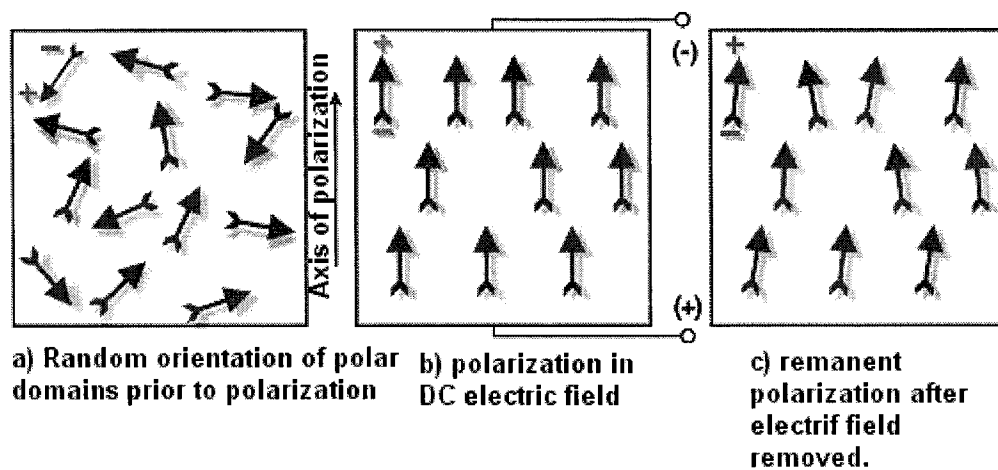


**Figure 1.6:** Poling of a piezoelectric material [37]

Poled piezoelectric materials are anisotropic since their mechanical and electrical properties are different along diverse directions. Prior to poling, poly-crystal piezoelectric materials are isotropic if they have a random orientation of grains. In poled piezoelectric materials, under a “small” electric field, the change in dimension of the piezoelectric material is linear with respect to the “small” electric field strength. As the field strength increases the change in dimensions of the electric field become non-linear. The non-linearity is due to the non-linear strain behavior of piezoelectric materials at high voltages.

Figure 1.7 shows the effect of the electric field over the material strain. At point (1) the material is poled along the negative direction of the electric field while a positive electric field is applied. The material will suffer shrinkage as the electric field is applied in the positive direction. At point (2) the strain reaches a minimum, which is the point when the electric field reaches coercive field strength. At the coercive field strength the polarization starts to change direction and the material starts to expand up to a maximum point (3). Once the electric field is removed the material remains polarized similar to the starting point but in opposite direction (4).

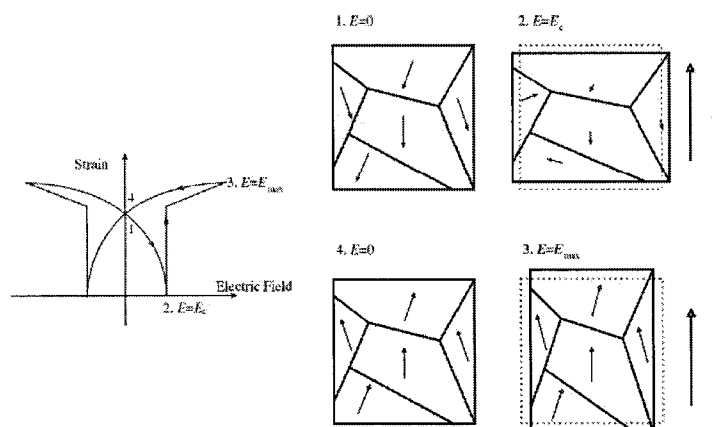


**Figure 1.7:** Strain vs. Electric Field for a piezoelectric material at the poled domain [38]

Piezoelectric materials have generated many expectations among engineers and scientists who are looking for ways of creating smart material structures. Researchers and engineers in recent years have worked with piezoelectric materials in order to make piezoelectric materials act as actuators, sensors or both.

As technology advances there is a need for more “biological-like” materials that are capable of sensing and actuating. Piezoelectric materials can provide such functions, however, if piezoelectric materials are to be more widely used in engineering applications, they will be mostly in the form of composites. Bulk piezoelectric materials have several serious drawbacks impeding their applications. It is the brittle nature of piezoelectric materials that limit their widespread implementation. Most piezoelectric materials are ceramics. Ceramic materials have an inherently low toughness that limits their use in any critical application. A number of brittle materials have been used for structural applications in the form of fibers in fiber reinforced composite materials. Such composites provide materials with high strength and high toughness. Recently, several attempts were made to develop composite materials with piezoelectric fibers [39-42]. Such active fiber composites (AFC) can be used as actuators and/or sensors in a number of different applications.

A combination of piezoelectric materials in a composite allows for the composite to be tougher, as well as flexible. A major advantage of a piezoelectric composite structure, over non-piezoelectric composites, is the ability to actuate and sense under the influence of an electrical or a deformation field respectively. As the material deforms the piezoelectric fibers

inside the material produce an electric voltage potential that can be used as sensors, thus serving as a component of an IMS.

The use of AFC for practical applications is still restricted by the lack of detailed knowledge about the relationship between the structure, manufacturing process, and material performance. Currently, for several AFC systems, the research is being conducted on the relationships between structures, properties of constituent components, and the behavior of the system as a whole [43]. One particularly challenging problem is the analysis of a long-term behavior and degradation of AFC materials. The study of the effect of fiber damage on the performance of AFC is an integral part of this research [39].

Composite materials (both conventional composites and AFC) provide an important opportunity for the material design approach, in which material properties are optimized or tailored to the requirements of the application through manufacturing. The tailoring of materials allows for an optimum material design for the application that it is being designed for. In order to use this approach, design tools are necessary to determine which structure is optimal or to predict how differences in structure result in different properties. AFC materials present a more challenging task for the development of such design models because their behavior is affected by a usually non-uniform distribution of the electrical field. This problem becomes especially challenging in the case of short fiber materials or materials with damaged fibers.

In non-piezoelectric composite structures there has also been a need to analyze the characteristics and properties of composite structures. Carbon and fiberglass materials have

very little structural applications on their own, but when combined with a material matrix they serve as structural members in the aerospace industry. The filler material used, the amount of filler material, the shape and how it is organized within the material matrix, determines the properties of the composite and its primary purpose such as weight reduction, strength and cost among others. Figure 1.8 shows the different types of fiber reinforced composite structures and sandwich composite structures.

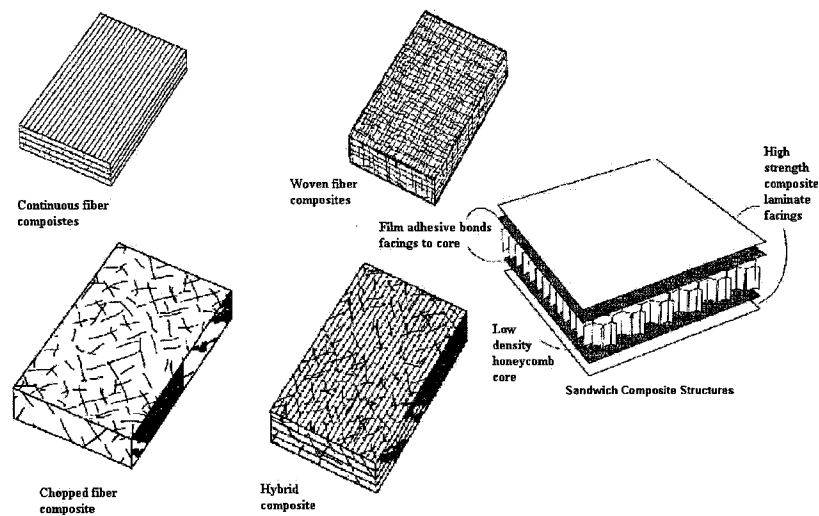


**Figure 1.8:** Composite Structures [44]

As shown in Figure 1.8, continuous fibers are widely used due to their strength capabilities, although this type of composite has its weakness in the possibility of delaminating and its inherently anisotropic characteristics. Figure 1.8 also shows composites made out of woven fibers. These types of composites avoid the delaminating drawback of continuous fiber, but at the expense of strength. Figure 1.8 shows chopped fiber composites. In chopped fiber composites the fibers are randomly oriented within the material matrix. Chopped fiber composites have the advantage of being less expensive to produce. These structures do not

have the strength of continuous fiber composites. Another example of composite structures is the hybrid composite, which consists of a combination of chopped and continuous fibers. Hybrid composites can be manufactured with different layers, for example, fiber reinforced and metal layers, or layers with different types of fibers. Finally a very common type of composite in the aerospace industry is the sandwiched composite, which is a combination of a low density honeycomb core, adhesive bond and a high strength composite laminate [44].

The finite element method (FEM) can provide an efficient computational tool for the modeling and design of composite structures, as well as actuated fiber composites. This thesis focuses on the development of finite element (FE) solver to analyze the electro-mechanical behavior of systems with elastic and piezoelectric components such as AFC.

### **1.1 Material properties of Piezoelectric & Ferroelectric materials**

Ferroelectric crystals are those that exhibit spontaneous polarization and in which polarization can have a change in direction when influenced by an external electrical field. The properties of all materials are determined by the crystallographic arrangement of atoms. The polarization of the material is affected by internal and external factors. The existence or lack of structural symmetry of the crystal is an internal factor that affects the polarization of the material. External factors can also affect the polarization of the material, such as temperature. Some ferroelectric crystals exhibit different microstructure arrangement at different temperatures for which the crystal does not exhibit ferroelectric properties; this temperature is known as the Curie temperature. It is important to note that the Curie temperature is the temperature at

which a paraelectric-ferroelectric phase transition occurs. Many ferroelectric materials undergo several phase transformations at different temperatures, which are known as phase transition temperatures. Figure 1.9 shows the crystal structure of barium titanate. When the temperature of the structure is raised to 120°C (Curie temperature) the unit cell structure of the barium titanate becomes cubic. Below the Curie temperature the structure becomes slightly deformed producing a dipole at the unit cell level. Materials that exhibit a polarization change, due to a change in temperature, are known as pyroelectric materials [25].

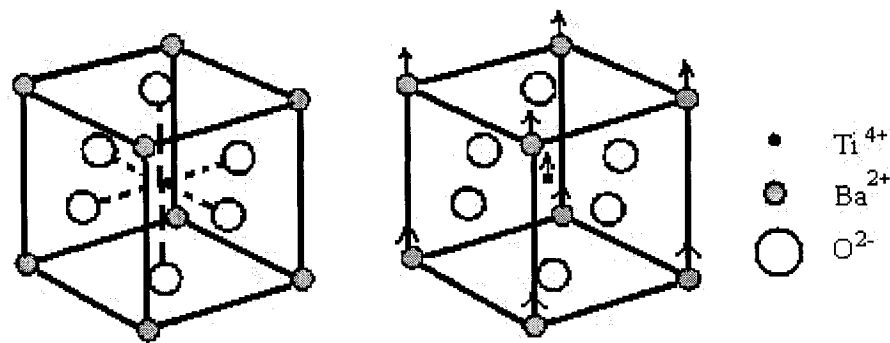


**Figure 1.9:** Crystal Structure of barium titanate [25]

As it has already been stated, the direction of the polarization vector for many domains in the crystal structure is influenced by the strength of the electric field and temperature. Hysteresis in a piezoelectric material can be defined when the polarization (or strain) of a piezoelectric material does not instantly follow, reacts slowly, or does not return completely to their original polarization (or strain) state, to an applied electric field as shown in Figure 1.10. In other words, if we plot strain or polarization vs. electric field from zero to a specific value of electric field and then from the specific value back to zero volts, the strain or polarization curves will follow different ascending and descending curves. Hysteresis loops are a consequence of the

inability of domain regions to re-align in the direction of the electric field or formation of domain patterns providing minimum state of energy.

In 1930, Sawyer-Tower published a paper on how ferroelectric hysteresis loops could be observed by means of an electric circuit [25]. Sawyer-Tower demonstrated in his paper that by monitoring the voltage with an oscilloscope the hysteresis loop could be determined. Figure 1.9 shows a typical hysteresis loop for a piezoelectric material.

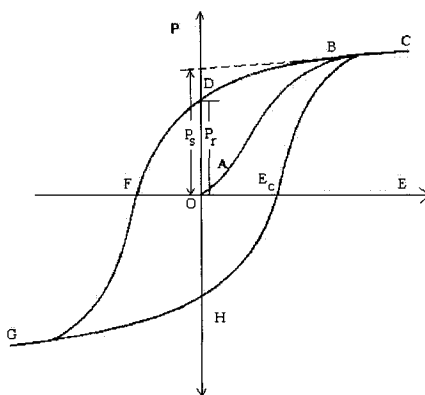


**Figure 1.10:** Polarization vs. Electric Field Hysteresis Loop [25]

As shown in Figure 1.10, when an applied electric field is small the polarization in the piezoelectric material is almost linear (points 0–A). This linearity is also possible for any small increment of the electric field were the curve could be approximated as a line. As the electric field forces increase the polarization reaches a saturation point at C. A zero electric field force shows some polarization, due to aligned domains, that remain aligned even after the electric field has been removed (point D). The remaining polarization is indicated in Figure 1.10 by the distance  $P_r$ . If the electric field changes direction then the polarization past point D rapidly

approaches zero at a value of the electric field known as the coercive field strength. If the electric field increases in the negative direction then saturation of the polarization also occurs at point G. If the electric field is increased in the positive direction then a negative value of polarization will remain at an electric field value of zero. This remainder polarization is due to the alignment of the domains even after the electric field has been removed. A final increase of the electric field in the positive direction causes the dipoles to follow the direction of the electric field until saturation occurs again at point C. Thus, the complete hysteresis curve is represented by CDFGHC.

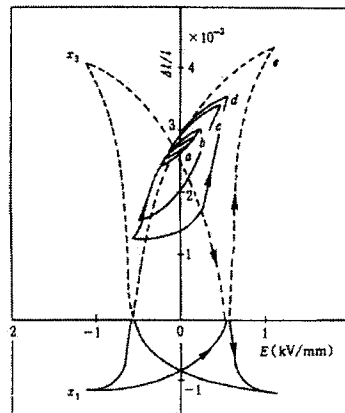


**Figure 1.11:** Strain vs. Electric Field in piezoelectric materials [38]

Figure 1.11 shows the electric field vs. strain for a piezoelectric crystal. When the maximum electric field is small the curve produced is almost linear as in the case of type (a) curve shown in Figure 1.11. As the maximum amplitude of electric field increases the hysteresis curves becomes more pronounced as shown in curves (b,c,d). Once the amplitude of the electric field increases beyond the coercive field the hysteresis curves transforms into a symmetric butterfly

shape, due to a polarization re-orientation as shown in Figure 1.11 [38]. The non-linearity of piezoelectric crystal make their application more difficult, on the other hand it is in the non-linear region were the material achieves its largest deformation.

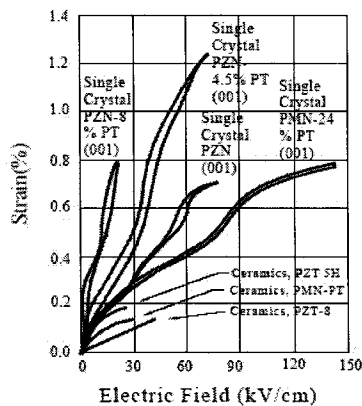


**Figure 1.12:** Strain vs. E-field behaviors for various electromechanical ceramics [45]

Figure 1.12 shows the strain behavior of several types of piezoelectric materials as a function of the electric field. As seen in Figure 1.12, it is noticeable that hard piezoelectrics have very little hysteresis. The fact that hard piezoelectrics have little hysteresis comes at the expense of low strain for hard piezoelectric crystals. It is believed that this low value of strain is due to a breakdown in the dielectric strength and polarization saturation. In contrast, soft piezoelectric show higher levels of strain and also very non-linear response between the electric field and their strain. The high values of hysteresis are due to domain motion. This high hysteresis results in poor accuracy of actuation control.

Shrout has shown larger strains on single crystal piezoelectric that are capable of producing strains in the order of 1.2% [45]. The higher strains of single crystals piezoelectric are

believed to occur due to a phase transformation as in the case of PZN-4.5%PT. This opens a wider range of uses for these materials, for example, actuators.

## 1.2 Actuated Composites

In recent years piezoelectric materials have been manufactured as piezoelectric fibers and used in the manufacturing of composite structures. Piezoelectric fibers embedded in an epoxy matrix, allow for composite structures that are capable of actuating and sensing. These types of composite structures are known as Actuated Fiber Composites (AFCs).

The simplest type of actuation scheme is to have a composite or a monolithic piezoelectric material sandwiched in between two electrodes as shown in Figure 1.13.

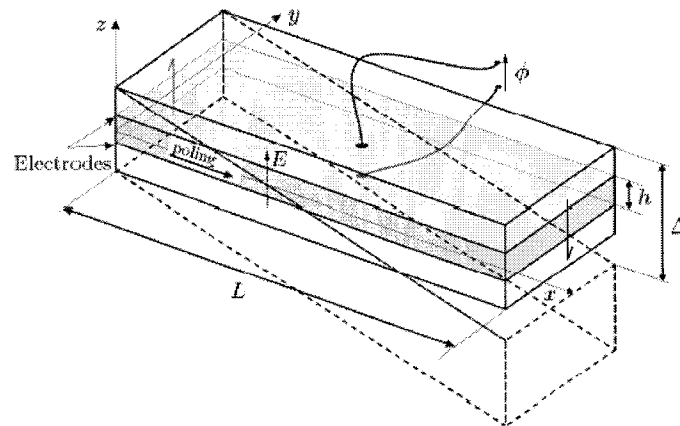


**Figure 1.13:** Simple piezoelectric composite [38]

As seen in Figure 1.13 when the electric field is orthogonal to the poling direction of the piezoelectric material it causes a shear deformation of the material. The poling direction and the electric field determine the actuation mode of the monolithic or composite piezoelectric beam. Details on the different forms of actuation mode will be explained in Section 1.3 of this chapter.

Recently, composite structures with more complicated actuation methods are being manufactured and investigated. These more complicated composites use more complex electrode patterns vs. two continuous electrodes. These electrode patterns are known as interdigitized electrodes (IDE) and allow for the poling of the fiber to occur in situ, as well as, serving as the actuation electrodes of the AFC. The next few pages will describe the manufacturing process used in order to create piezoelectric fibers used in AFC.

The fabrication of AFCs requires three primary components, as shown in Figure 1.14:

1. Piezoelectric fibers. These fibers can have different geometric cut sections and are usually extruded. These cross sections can also be hollow, allowing for lower actuation voltages [46]. In certain cases, such as in the case of materials developed by the NASA-Langley Research Center, known as Macro-Fiber Composite Actuator (LaRC MFC) the fibers are diced leaving a rectangular cross sectional fiber.
2. The matrix, usually an epoxy, acts as a means of holding the fibers together.
3. Polyimide film with imbedded electrodes.

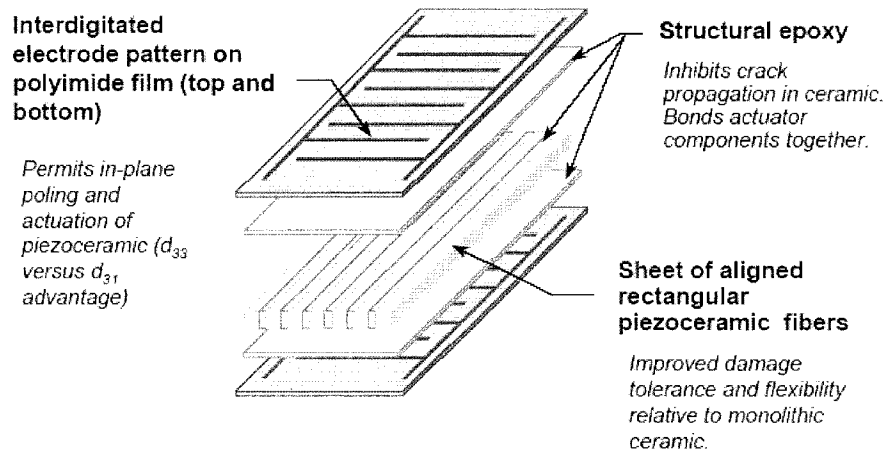


**Figure 1.14:** AFC Components [47].

In the case of the LaRc-MFC shown in Figure 1.14, the fibers are cut using a computer-controlled dicing saw. The fibers are diced directly on a polymer film, thus allowing for ease of handling. This allows for a low cost manufacturing process that is repeatable, accurate and automated. Figure 1.15 shows the LaRc-MFC fiber sheet fabrication process.

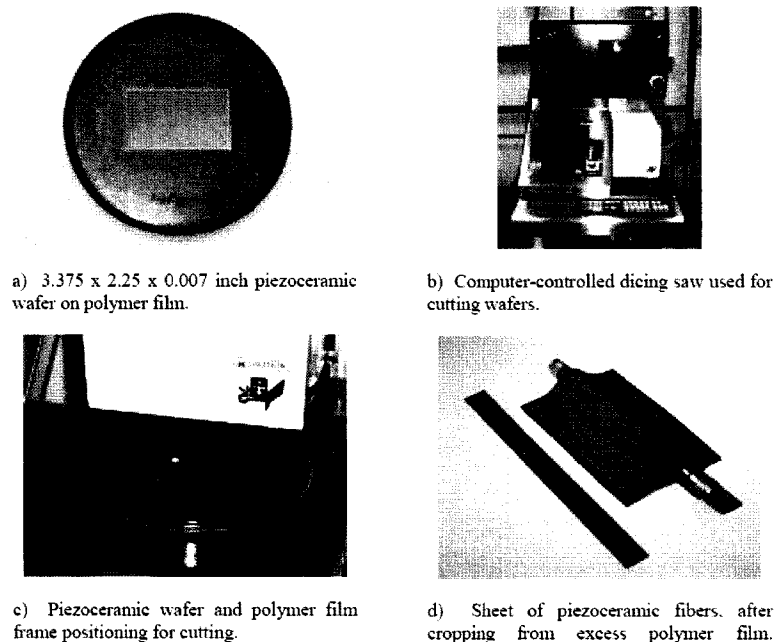


**Figure 1.15:** MFC<sup>TM</sup> piezoelectric fiber sheet fabrication [47].

The second component required, in an AFC, is a polyamide sheet with electrodes. The polyamide serves as an insulator, which is necessary to create the electrical field that actuates the piezoelectric fibers.

Figure 1.16 shows the actuated electrode pattern that is used in the LaRc-MFC. The electrode pattern is manufactured using photo-resist and etching processes.

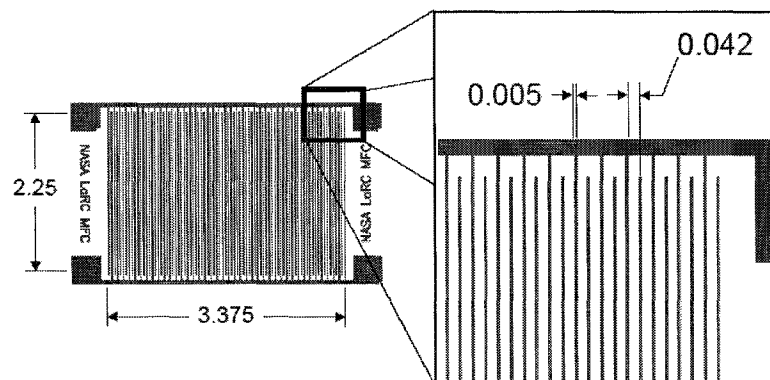


**Figure 1.16:** MFC™ Actuator electrode pattern (dimensions in inches) [47].

The final step consists of applying an epoxy adhesive and placing the piezoceramic fiber/polymer film sheet, shown in Figure 1.17, on a polyamide electrode edged sheets, shown in Figures 1.17-a, 1.17-b, 1.17-c and 1.17-d. Once the fibers have adhered correctly, the polymer film carrier is removed leaving the piezoceramic fibers attached to the electrode edged polyamide. A second layer of electrode edged polyamide film with epoxy sandwiches the fibers in place. The complete assembly is then cured in a pressure-heated chamber.

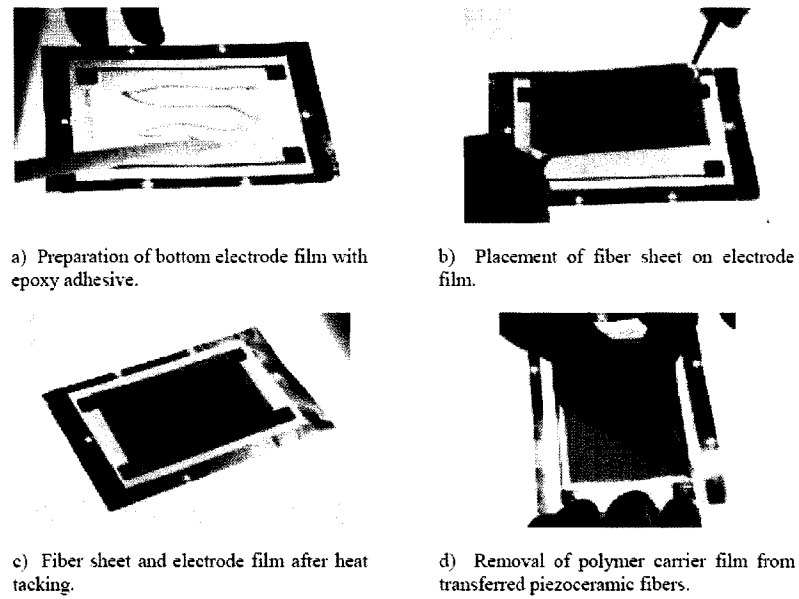


Figure 1.17: LaRC MFC™ Fabrication [47]

The final product is shown in Figure 1.18.

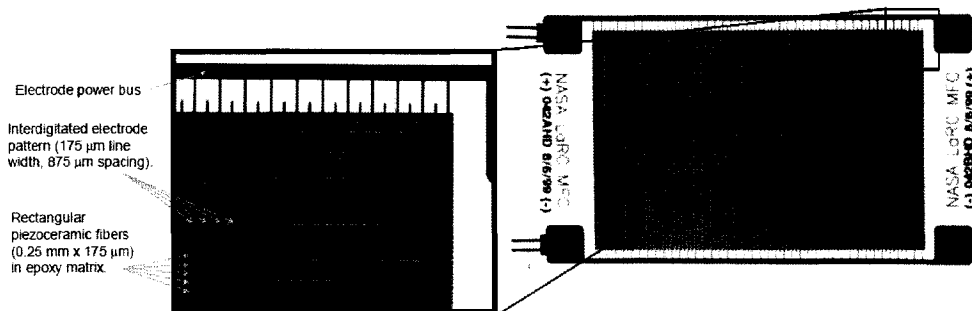


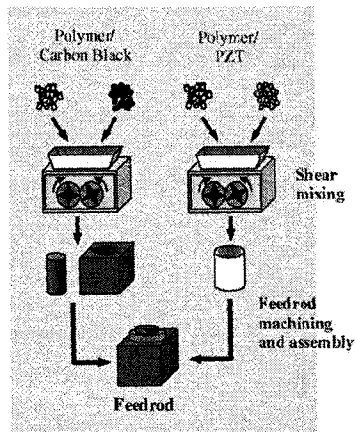
Figure 1.18: Completed Assembly of LaRC MFC [47].

Other approaches to actuation of AFC materials have been investigated. The cross sectional geometry of the fiber is not required to be rectangular or fully filled. In the next few paragraphs we will describe briefly manufacturing techniques for such piezoelectric fibers.

### 1.2.1 AFC with composite fibers

The possibilities of composite fibers are also being investigated. Composite fibers consist of hollow fibers with embedded internal electrodes on the inside and outside of the fiber. Under these conditions the electric field that causes the deformation of the fiber goes through the wall thickness of the fiber and not the complete fiber. This type of fiber is more difficult to manufacture than the LaRc-MFC but requires less voltage to actuate the AFC. The difficulties on a hollow fiber composite arise from the manufacturing of a hollow fiber and the implementation of an internal electrode inside the center of the fiber.

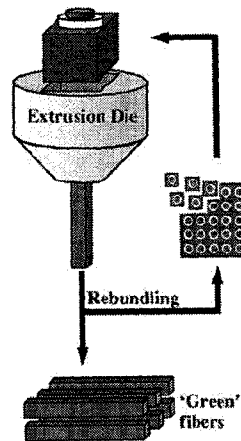
The first step in manufacturing hollow piezoelectric fibers is to create a mixture of thermoplastic polymer and piezoelectric compound with equal viscosity to avoid cross sectional deformation when mixing. Another mixture of carbon black powder and thermoplastic polymers are combined. Both of these mixtures are past through a shear mixer. The mixing occurs at high temperature (160°C) and at a speed of 30 RPM. The mixtures are then pressed, machined and cooled into feed rods with the desired dimensions such as to have the carbon/polymer feed rod inserted into the piezoelectric/polymer feed rod. This process is summarized in Figure 1.19. [46]



Step 1. Feed rod formation

Figure 1.19 Manufacturing of Feed rods [46]

The second step in the fabrication of hollow piezoelectric fibers is the extrusion of the feed rods. The extrusion is performed at approximately 1200Kg and permits a reduction in the diameter of the fiber by a factor of 25, while at the same time maintaining the same aspect ratio (fiber thickness to outside diameter) as the original extrusion as shown in Figure 1.20 [46].



b) Step 2. Extrusion

Figure 1.20 Fiber Extrusions [46]

The third step is the sintering and burning process. The burnout process burns the black carbon/thermoplastic core. The burnout process lasts approximately 18 hours at 600°C. The sintering process occurs at a heat rate of 180°C/hour until it reaches approximately 1285°C for a period of 2 hours. This sintering process allows for the piezoelectric ceramic fiber to become dense and strong. The burnout and the sintering occur by having the fibers vertically hanging to avoid them from warping during manufacturing [46]. This process is graphically explained in Figure 1.21.

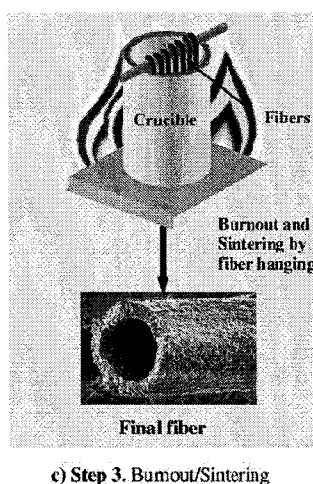


**Figure 1.21:** Burnout and Sintering [46]

The incorporation of the electrodes is problematic since the intent of hollow fibers is to have the electrode on the outer and inner surface of the hollow fiber. In order to overcome this problem, the inner electrode is wrapped to the outside layer. This allows for many fibers to be connected by means of a single power bar. Figure 1.22, outlines this concept.

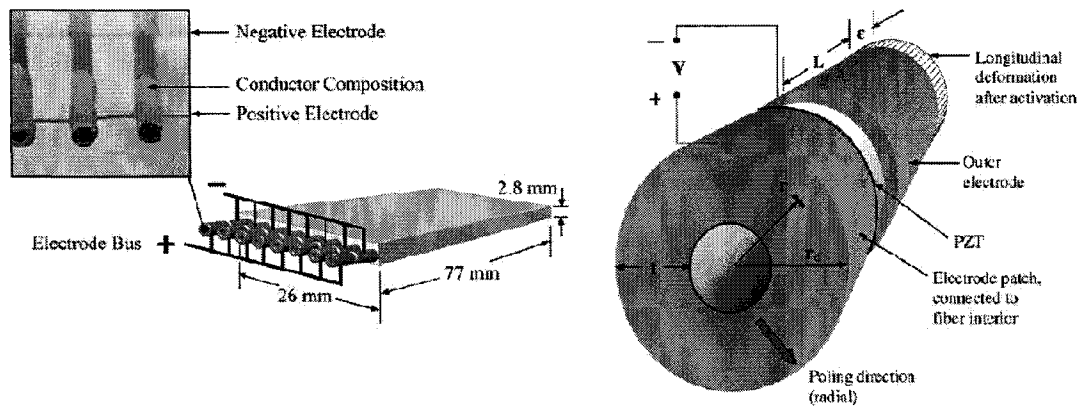


**Figure 1.22:** Electrodes on hollow fiber AFC [46]

### 1.3 Main types of Piezoelectric Actuators

Many applications for smart materials have been researched and developed. As with many new material and technology initiatives, the initial applications are usually military. Smart materials are no exception: Smart materials have been utilized and researched for active structural control applications [47], rotor blade damping controllers, aero-elastic vibration and surface control. Among many of the diverse applications being investigated, most of which are still in the research and development stages [48]. Other non-military applications in biomedical, telecommunication, actuators design are now also being researched. For example, in the semiconductor industry the use of piezoelectric ceramics as valves on mass flow controllers is frequently used. Also piezoelectric materials are commonly used in the design of hydrophones, pressure transducers and force transducers. In the next few paragraphs an emphasis on the different actuation mechanism using piezoelectric materials will be presented and briefly discussed.

The main purpose of any actuation mechanism is to achieve, high displacements, and high force over a wide variety of frequency, while requiring small amounts of power. For some applications piezoelectric material are able to achieve all these properties, such as in the case of micro positioning [49].

Piezoelectric actuators can be divided into monolithic piezoceramic actuators, among which we have:

- Stack Actuators,
- Laminar Actuators,
- Shear Actuators and
- Bimorph Actuators

Other types of actuators that are not monolithic are:

- Building Block Actuators
- Lever Arm Actuators
- Hydraulic Amplification
- Flexensional Actuators
- Frequency Leveraged Actuators and

- Actuated Fiber Composites (AFCs)

In the next few pages we will describe the primary characteristics of some of these actuators.

### 1.3.1 Stack Actuators

The Stack actuator, as shown in Figure 1.23, consist of stacking piezoelectric disks or plates interconnected by electrodes. The stack actuator design is common for position control applications. The stroke ( $\Delta$ ), when no external force is applied, is a function of the number of piezoelectric disks ( $n$ ), the voltage ( $\phi$ ), the length of the stacked actuator ( $L$ ) and the piezoelectric constant ( $d_{33}$ ). It is for this reason that this type of actuator is also known as the  $d_{33}$  actuator design [38]. Stack actuators have demonstrated that they have the highest stiffness and are able to sustain high-pressure loads [50]. The actuation performance of a piezoelectric actuator is a function of the material properties of the actuator (piezoelectric constants). Table 1.1 outlines the piezoelectric properties for PZT-5A.

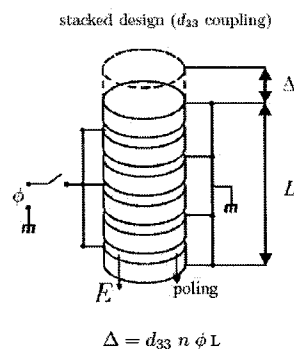


**Figure 1.23:** Stack Actuator [38]

Table 1.1: Piezoelectric Constants for PZT-5A

Constant	Value ( $10^{-12}$ C/N)
$d_{31}$	-171
$d_{33}$	374
$d_{24}, d_{15}$	584

### 1.3.2 Laminar Actuator

Laminar Actuators are very similar in nature to piezoelectric stack actuators in that the electric field and the polarization direction of the material are in the same direction. In a laminar actuators the poling of the material and electric field are in the same direction. These types of actuators are also used for micro-positioning control. The laminar actuator stroke ( $\Delta$ ) is also a function of the width of the piezoelectric plate ( $h$ ), the voltage ( $\phi$ ), and the material property ( $d_{31}$ ). The laminar actuator is shown in Figure 1.24.

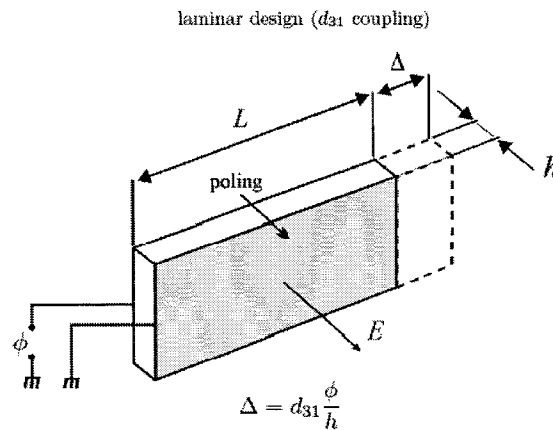


Figure 1.24: Laminar Actuation [38]

### 1.3.3 Shear Actuator

The shear actuation makes use of the piezoelectric constants  $d_{15}$ , and  $d_{24}$  as their primary deformation mode. The shear actuator, as stated by its name, shears the piezoelectric material. In this type of actuator the poling direction of the material and the electric field are orthogonal to each other. Figure 1.25 shows a shear actuator.

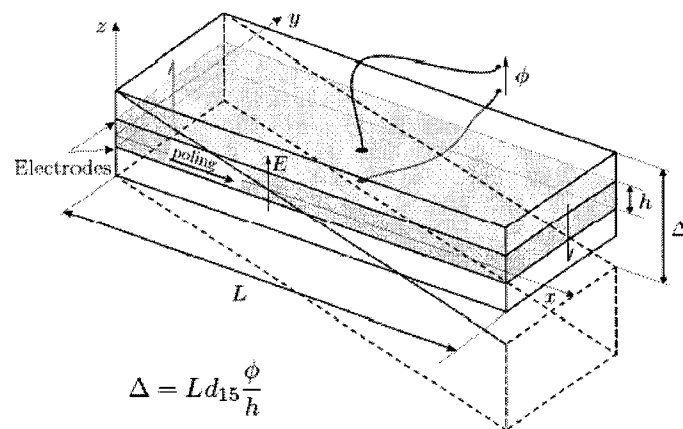
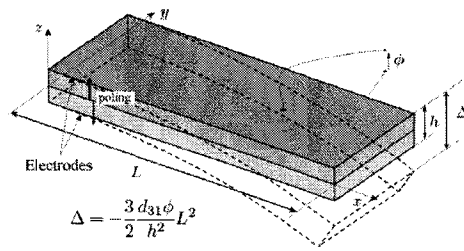


Figure 1.25: Shear Actuation [38]

### 1.3.4 Bimorph Actuator

Bimorphic actuators have been used in a variety of applications such as in robotics, spoilers and vibration of helicopter rotor blades. Most of these applications require large displacements. The bimorph actuator operates in the extension of the upper piezoelectric layer while contracting the lower piezoelectric layer. This extension and contraction is achieved by attaching two layers of piezoelectric that are poled in opposite directions, such that when under the presence of the same electric field it causes one layer to contract while the second layer expands, thus creating a bending deformation.



**Figure 1.26:** Bimorph Actuation [38]

The primary actuation mode of the bimorph actuator is that of  $d_{31}$ , as seen in the analytical equation presented in Figure 1.26.

The above actuators are of the simplest kind of actuating mechanisms and are of great importance because of simplicity. Simple analytical equations, as described in the figure, permit for quick estimates for deformation of these types of actuators. Recently, combinations of different types of actuators have been described in different journals. The following few paragraphs describe some more advanced actuating mechanisms. These types of actuators we will describe as non-monolithic.

### 1.3.5 Building Block Actuators

The concept of building block actuators is based on assembling a series of smaller actuators so to produce an actuator with better performance capabilities than the original building block. The C-block actuators, shown in figure 1.27, permit an increase in performance of approximately eight percent more work than an equivalent straight bender actuator [49]. Other types of building block actuators have also been studied, such as recursive actuators and telescopic actuators. Both of which are considered a building block actuator.

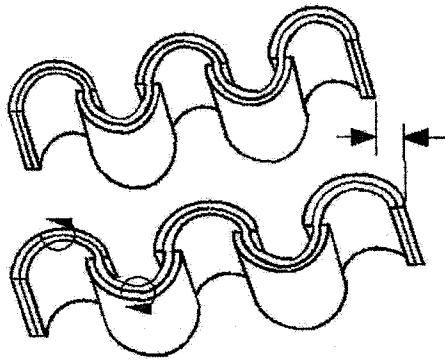


**Figure 1.27:** Building Block Actuation [49]

### 1.3.6 Lever Arm Actuators

Another possible way of increasing the performance of an actuator is to combine the piezoelectric actuator with mechanical devices, such as lever arms. This type of combination increases the output displacement but in the process the force produced by the actuator is reduced. Under this type of design the “moment rules” play an important role in order to determine the desired distance, the required force and the location of the pivoting point with respect to load location.

Figure 1.28 shows a lever arm actuator. The lever arm actuator makes use of the stacked piezoelectric actuator. The stacked actuator when excited causes the rotation of the mechanism [49].

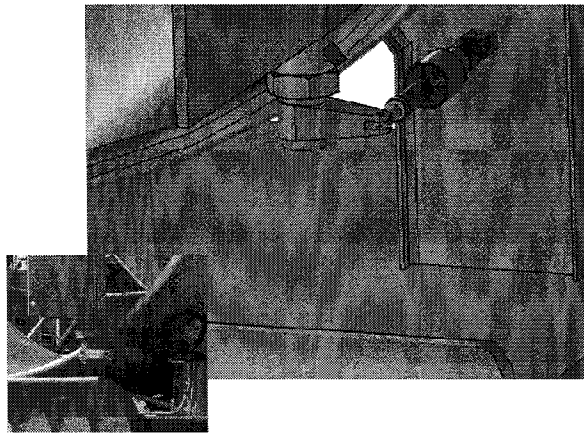


**Figure 1.28:** Stacked Linear Arm [51]

### 1.3.7 Hydraulic Amplification Actuator

The use of fluids as an intermediate medium to transfer force is an effective means of amplifying the transmission ratio up to 100 times. Figure 1.29 shows a typical schematic of a hydraulic amplification actuator. [49]

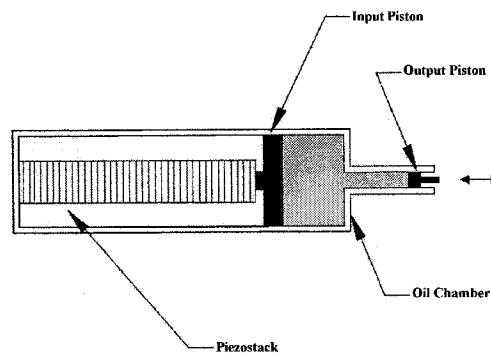


**Figure 1.29:** Hydraulic Amplification Actuator [49]

### 1.3.8 Flextensional Actuators

The flextensional actuator, shown in Figure 1.30, is also known as the Cymbal actuator. It consists of a piezoelectric stack that is attached at both ends to a cavity. As the piezoelectric actuator contracts or expands it causes the cavity to displace in a transverse direction. This type of actuator has a primary advantage, which is the capacity to increase the deflection and the force output.

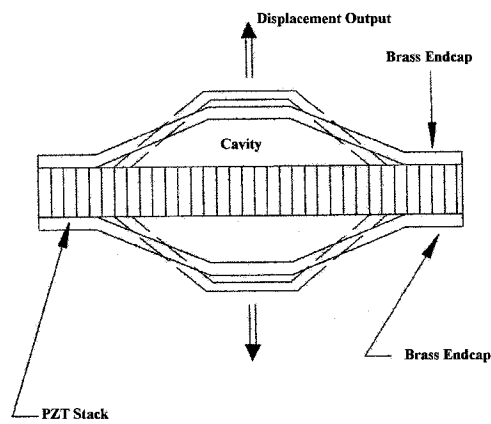


**Figure 1.30:** Flextentional Actuator [49]

### 1.3.9 Frequency Leveraged Actuators

The last type of actuator that will be described is the frequency-leveraged actuator. The primary advantage of this type of actuator is that it has infinite stroke capabilities at the expense of speed. This type of actuator consists of three piezoelectric actuators, the trailing, the leading and the extending. The trailing and the leading release and grab the rod depicted on Figure 1.31, while the extending and contracting arm extends and contracts in order to move

the rod. This allows for this actuator to have infinite stroke as long as it can grab and release the rod.

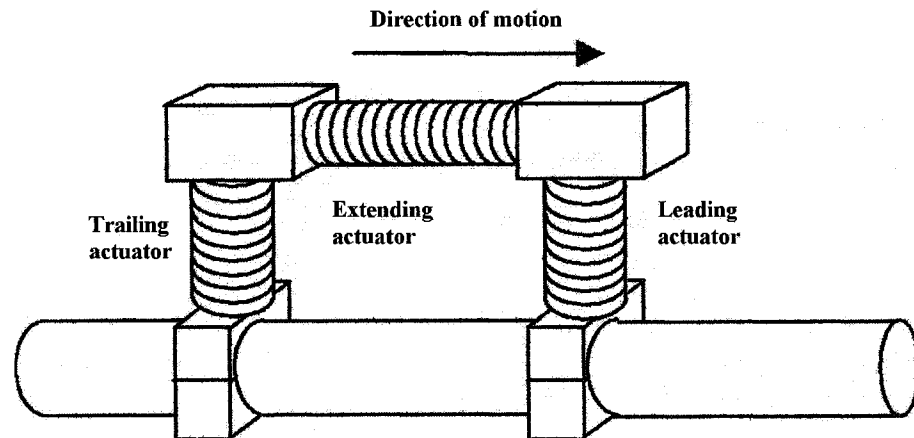


**Figure 1.31:** Frequency Inchworm Actuator [49]

#### 1.4 Summary

Chapter one of this thesis has presented a brief introduction on the importance of piezoelectric materials and how they could potentially play a major role in society as these are imbedded into composite materials. A definition of IMS is presented and described. The chapter presents a literature review focusing on ferroelectric material properties, followed by the use of piezoelectric fibers in AFCs. The manufacturing of AFCs with diverse fibers is considered and described. Finally most typical actuators found in literature are presented. The final goal of this thesis is to be able to simulate the behavior of piezoelectric materials using finite element methods. The main objective of this thesis is the development of a

computational tool that will allow us to simulate the behavior of elastic and piezoelectric structures. The need for a design tool arises from the necessity to simulate new material behavior and eventually the application of these new materials in large structural systems. The thesis is divided into six chapters.

Chapter two is followed with a detail derivation of the mechanical, electrical and coupled equations required to model piezoelectric structures mathematically.

Chapter three will focus on the implementation of the constituent mathematical equations into Finite Element Methods form (FEM).

Chapter four will concentrate on validating the elastic, piezoelectric elements and solver. The results obtained are compared to available analytical solutions.

Chapter five focuses on the use of the solver to analyze the behavior of Actuated Fiber Composites (AFC). The results are compared to experimental work performed by EMPA, Swiss Federal Laboratories for Material Testing and Research in Switzerland. Other problems using AFC are presented and analyzed, whenever possible the results are compared to analytical and experimental results.

Chapter 6 is the conclusion chapter of the thesis and briefly summarizes the results presented in all the chapters.

## 1.5 References for Chapter 1

- [1] Pierangelo Masarati, Gian Luca Ghiringhelli, On local solutions for piezoelectric laminates, Published by Elsevier Science Ltd. Computational Fluid and Solid Mechanics, 2001.
- [2] Anthony Faria Vaz, Composite Modeling of Flexible Structures with Bonded Piezoelectric Film Actuators and Sensors, Department of Mechanical and Aerospace Engineering at McMaster University, 2001.
- [3] Anthony Faria Vaz, Modeling of Piezoelectric Behavior for Actuators and Sensor Applications, Canadian Space Agency Report, ACE Document No. R-CSA-91-2.0, February 25th, 2001.
- [4] H.S. Tzou and H.Q. Fu, A study of segmentation of distributed piezoelectric sensors and actuators, Part I: Theoretical analysis. Journal of Sound and Vibration 1994.
- [5] Anthony Faria Vaz, Active Vibration Damping in Large Flexible Space Structures, June 1991.
- [6] Anthony Faria Vaz, Trip report on the first joint U.S. Japan, Conference on Adaptive Structures, Maui, Hawaii, Nov. 13-15, 1990.
- [7] A. Youseti-Koma, J.Z. Sasiadek, G. Vukovich, LQC Control of flexible structures using piezoelements, American Institute of Aeronautics and Astronautics, 1994.
- [8] Intelligent Structural Systems, Editors: H.S. Tzou, G. L. Anderson, Boston, Kluwer Academics 1992.

- [9] R.L. Clark, M.R. Flemming, C.R. Fuller, Piezoelectric Actuators for distributed vibration excitations of thin plates: A comparison between theory and experiment, *Journal of Vibration and Acoustics*, Vol. 115, July 1993.
- [10] *Polymer Sensors and Actuators*, Editors: Yoshihito Osada, Danilo De Rossi, New York, Springer-Verlag 2000.
- [11] *Smart structures and materials 1997 : smart structures and integrated systems : 3-6 March 1997, San Diego, California / Marc E. Regelbrugge, chair/editor ; sponsored by SPIE--the International Society for Optical Engineering ; cosponsored by SEM--Society for Experimental Mechanics, Inc., ASME--American Society of Mechanical Engineers ; cooperating organizations, Air Force Wright Laboratory [et al.] Bellingham, Wash., USA : SPIE, c1997.*
- [12] Junji Tani, Toshiyuki Takagi and Jinhao Qiu, *Intelligent material systems: Application of functional materials*, ASME Reprint no. AMR253, *Appl. Mech. Rev.* vol. 51, no 8, August 1998.
- [13] K. Otsuka, C.M. Wayman, *Shape Memory Materials*, Cambridge University Press, 1998.
- [14] Dimitris C Lagoudas and Iradj Tadjbakhsh, *Active flexible rods with embedded SMA fibers*, March 1992.
- [15] Aoyama, T. Iansaki, *Application of Electrorheological Fluid Dampers and Machine Tool Elements*, *Annals of the CIRP*, 46/1, 1997.
- [16] <http://www.glue.umd.edu/~gmkamath/er.html>
- [17] Mohsen Shahinpoor, *Micro-Electro-Mechanics of Ionic Polymeric Gels As Electrically controllable Artificial Muscles*, *Journal of Intelligent material Systems and Structures*, Vol 6- May 1995.

- [18] Electroactive Polymers, Editors, Q.M. Zhang, Takeo Furukawa, Yoseph Bar-Cohen, J. Scheinbelm, Symposium held Nov 29 to Dec 1<sup>st</sup>-1999, Boston Massachusetts, USA. CISTI Call number: TA401 M4256 v. 600.
- [19] Field Responsive Polymers, Electroresponsive, photoresponsive and responsive polymers in chemistry and biology, Editors: Ishrat M. Kahn, Joklyn S. Harrison, Washington DC, American Society, and Distributed by Oxford University Press 1999.
- [20] K.H.J. Buschow, F.R. de Boer, Physics of Magnetism and Magnetic Materials, New York: New York: Kluwer Academic/Plenum Publishers, c2003. CISTI Call number: QC753.2 B977.
- [21] Sina Valadkhan, Kirsten Morris, Amir Khajepour, Modeling of Magnetostrictive Materials under different load conditions, Cansmart 2005, Smart Materials and Structures Proceedings, 13-14 of October 2005, Toronto, Ontario Canada, 2005.
- [22] Jennifer Dooley, Induction mapping of magnetostrictive materials, Journal of applied physics volume 83, Number 11, June 1998.
- [23] Giant Magnetostrictive Materials O. Söderberg, A. Sozinov and V.K. Lindroos In: J. Buschow (Ed.) The Encyclopedia of Materials: Science and Technology Manuscript arranged according to the proof version (Emsat:02012).
- [24] Clark, A. E. Ferromagnetic Materials, vol 1, ed Wolfhart, E.P. (Amsterdam: North-Holland) pp. 531 (Picture taken from:  
<http://aml.seas.ucla.edu/research/areas/magnetostrictive/mag-composites/Magnetostriction%20and%20Magnetostrictive%20Materials.htm>).
- [25] Yuhuan Xu, “Ferroelectric Materials and Their Applications”, University of California Los Angeles, CA, USA, 1991.

- [26] W.J. Merz, Phys. Rev. 95 (1954) 690.
- [27] E.A. Little Phys. Rev 98 (1955) 978.
- [28] J. A. Hooton and W.J. Merz. Phys. Rev 98 (1955) 409.
- [29] S. Ikegami and I. Ueda, J. Phys. Soc. Jpn. 22 (1967) 725.
- [30] R.C. Bradt and G.S. Ansell, J. Am. Ceram. Soc. 52 (1969) 192.
- [31] C. Bousquet, M. Labert, A.M. Quittet and A. Guinier, Acta Crystallog. 16 (1963) 989.
- [32] G. L. Pearson and W.L. Feldman, J. Phys. Chem. Solids 9 (1959) 28.
- [33] J. Hatano, F. Suda and . Futama, Jpn. J. Appli. Phys 12 (1973) 1644.
- [34] Y. Furuhata and K. Toriyama, Appli. Phys. Lett 23 (1973) 361.
- [35] K. Yoshino. H. Taniguchi and M. Ozaki, Ferroelectrics 91 (1989) 267.
- [36] David M. Walba, Ferroelectric Liquid Crystals a Unique State of Matter, Advances in the Synthesis and Reactivity of Solids, JAI Press Volume 1, pages 173-235 1991.
- [37] [http://www.americanpiezo.com/piezo\\_theory/index.html](http://www.americanpiezo.com/piezo_theory/index.html) last accessed on January 30, 2006.
- [38] Vincent Piefort, Finite Element Modeling of Piezoelectric Active Structures, PhD. Thesis, Université Libre de Bruxelles, 2000-2001.
- [39] M. Martinez, A. Artemev, F. Nitzsche, B. Geddes, Finite Element Modeling of Actuated Fibre Composites, Conference proceeding for HSPM 2006, Ostend-Belgium May 3-4, 2006.
- [40] M. Martinez, M. Melnykowycz, A. Artemev, F. Nitzsche, Finite Element Analysis of Actuated Fiber Composites, Cansmart 2005, International Workshop, Smart Materials and Structures, 13 - 14 October 2005, Toronto, Ontario, Canada.

- [41] Internal Report: Prof. Dr. Paolo Ermanni, Benedetto Castelli, Alberto Belloli, Modeling and Characterization of Active Fiber Composites Diploma Thesis at the Centre of Structure Technologies, Institute of Mechanical Systems, Department of Mechanical and Process Engineering, ETH Zurich IMES Ref.-Nr: 08-183.
- [42] Cu-Hai Nguen and Xavier Kornmann, A Comparison of Dynamic Piezoactuation of Fiber-based Actuators and Conventional PZT Patches Journal of Intelligent Material Systems and Structures, Vol. 17—January 2006 45.
- [43] Eve Lenglet, Anne-Christine Hladky-Hennion and Jean-Claude Debus , Numerical homogenization techniques applied to piezoelectric composites, Acoustical Society of America, 2003.
- [44] Ronald F. Gibson, Principles of Composite Material Mechanics, McGraw-Hill Series, 1994.
- [45] Thomas R. ShROUT, Relaxor based ferroelectric single crystals for electro-mechanical actuators, Springer-Verlag 1997.
- [46] Dian Brei, Bryan J. Cannon, Piezoceramic hollow fiber active composites, Composite Science and Technology, June 11-2003.
- [47] W. Keats Wilkie, Robert G. Bryant, James W. High, Robert L. Fox, Richard, F. Hellbaum, Antony Jalink jr., Bruce D. Little and Paul H. Mirick, Low-Cost Piezocomposite Actuator for Structural Control Applications, NASA Langley Research Center, Hampton VA 23681-2199. Presented at SPIE's 7<sup>th</sup>, Newport Beach March 5-9 2000.
- [48] Aaron A. Bent, Active Fiber Composite Material Systems for Structural Control Applications, DARPA Smart Structures Technology Interchange Meeting, Baltimore, MD, June 26-27, 2000.

- [49] Christopher Niezrecki, Diann Brei, Sivakumar Balakrishnan and Andrew Moskalik,  
Piezoelectric Actuation: State of the Art, The Shock and Vibration Digest, Vol 33, No. 4  
July 2001, pp. 269-280.
- [50] <http://www.physikinstrumente.com/tutorial/> , Theory and Application of Piezo  
Actuators and PZT NanoPositioning Systems.
- [51] Jeremy Frank, Gary Koopmann, Jacob Loverich, Bob Drwal, Morphing Aircraft  
Structures, KFC Technologies and Penn State, Power Point Presentation.

## ELECTRO MECHANICAL EQUATIONS

### **2.0 Introduction**

A derivation of the electro-mechanical constitutive relationships is presented based on thermodynamic principles [1]. A derivation of the electro-mechanical stiffness matrix is presented from the weak formulation of the mechanical equilibrium equation, electrical equilibrium equation and the electro-mechanical constitutive equation [2-4].

### **2.1 Thermodynamics and constitutive relationships of piezoelectric materials**

The constitutive equations of piezoelectric systems can be derived from the thermodynamic principles.  $G$  is the Gibbs free energy of the system as described in equation 2.1. The Gibbs free energy is a function of  $U$ , the internal energy of the system,  $\epsilon$  the strain tensor of the system,  $D$  the electric displacement vector,  $B$  the magnetic induction vector and  $\eta$  the entropy of the system. Temperature ( $\Theta$ ), stress ( $\sigma$ ), electric field ( $E$ ), and magnetic field ( $H$ ) are also parameters that determine the behavior of a piezoelectric crystal. The Gibbs free energy of this system can be defined by taking into account the different energy contributions as shown in equation 2.1:

$$G = U - \varepsilon_{ij} \sigma_{ij} - D_m E_m - B_m H_m - \eta \Theta \quad (2.1)$$

In order to simplify the problem we will assume that the Gibbs free energy of the system is only a function of the stress, electric field and temperature and that they are independent variables as shown by equation 2.2.

$$G = G(\sigma_i, E_m, \Theta) \quad (2.2)$$

It is important to note the switch from tensor to engineering notation from this point on in the thesis. The engineering notation that we use defines the strain and stress parameters, in vector form, in the following order 11, 22, 33, 12, 23, and 31. For example the stress vector,  $\sigma_i$ , would contain the stress components in the following order  $\sigma_{xx}, \sigma_{yy}, \sigma_{zz}, \sigma_{xy}, \sigma_{yz}, \sigma_{zx}$

By taking the partial derivative of Gibbs free energy with respect to stress, and similarly with respect to the electric field and to temperature we obtain:

$$\begin{aligned} \varepsilon_i &= - \left( \frac{\partial G}{\partial \sigma_i} \right)^{E, \Theta} \\ D_m &= - \left( \frac{\partial G}{\partial E_m} \right)^{\sigma, \Theta} \\ \eta &= - \left( \frac{\partial G}{\partial \Theta} \right)^{\sigma, E} \end{aligned} \quad (2.3)$$

where,

- $\varepsilon_i$  is the strain of the system,  $D_m$  is the electrical displacement of the system in x, y and z, and  $\eta$  is the entropy of the system.

- The superscripts E,  $\sigma$  and  $\Theta$  indicate that the electric field, stress and temperature are kept constant.

The differentials of strain, displacement and entropy (equation 2.3) can be presented as:

$$\begin{aligned}
d\varepsilon_i &= \sum_j \left( \frac{\partial \varepsilon_i}{\partial \sigma_j} \right)^{E, \Theta} d\sigma_j + \sum_n \left( \frac{\partial \varepsilon_i}{\partial E_n} \right)^{\sigma, \Theta} dE_n + \left( \frac{\partial \varepsilon_i}{\partial \Theta} \right)^{\sigma, E} d\Theta \\
dD_m &= \sum_j \left( \frac{\partial D_m}{\partial \sigma_j} \right)^{E, \Theta} d\sigma_j + \sum_n \left( \frac{\partial D_m}{\partial E_n} \right)^{\sigma, \Theta} dE_n + \left( \frac{\partial D_m}{\partial \Theta} \right)^{\sigma, E} d\Theta \\
d\eta &= \sum_j \left( \frac{\partial \eta}{\partial \sigma_j} \right)^{E, \Theta} d\sigma_j + \sum_n \left( \frac{\partial \eta}{\partial E_n} \right)^{\sigma, \Theta} dE_n + \left( \frac{\partial \eta}{\partial \Theta} \right)^{\sigma, E} d\Theta
\end{aligned} \tag{2.4}$$

Expanding equation 2.4 we obtain the piezoelectric equations as shown in equation 2.5. It is important to note that the elimination of the differential operator from equation 2.4 to equation 2.5 is due to the fact that  $\varepsilon_i$  is equal to  $d\varepsilon_i$  since the choice of reference state is arbitrary.

$$\begin{aligned}
\varepsilon_i &= \varepsilon_{i,1}^{E, \Theta} \sigma_1 + \varepsilon_{i,2}^{E, \Theta} \sigma_2 + \cdots + \varepsilon_{i,6}^{E, \Theta} \sigma_6 + d_{i,1}^{\Theta} E_1 + d_{i,2}^{\Theta} E_2 + d_{i,3}^{\Theta} E_3 d\Theta \quad (i = 1, 2 \dots 6) \\
D_m &= d_{m,1}^{\Theta} \sigma_1 + d_{m,2}^{\Theta} \sigma_2 + \cdots + d_{m,6}^{\Theta} \sigma_6 + \kappa_{m,1}^{\Theta} E_1 + \kappa_{m,2}^{\Theta} E_2 + \cdots + \kappa_{m,3}^{\Theta} E_3 + p_m^{\sigma} d\Theta \\
dQ &= \Theta d\eta = \Theta (\alpha_1^E \sigma_1 + \alpha_2^E \sigma_2 + \cdots + \alpha_6^E \sigma_6) + \Theta (p_1^{\sigma} E_1 + p_2^{\sigma} E_2 + \cdots + p_6^{\sigma} E_6) + \rho c_p^E d\Theta
\end{aligned} \tag{2.5}$$

The superscripts of E,  $\sigma$  and  $\Theta$  indicate that the electric field, stress and temperature are kept constant. The specific heat value,  $c_p$ , is used in this equation with a constant electric field and pressure.

From equations 2.4 and 2.5 the following coefficients can be defined:

- Elastic compliance coefficient  $\bar{C}_{ij}$  :

$$\bar{C}_{ij} = \frac{\partial \varepsilon_i}{\partial \sigma_j}$$

- Permittivities  $\bar{\kappa}_{mn}$  :

$$\bar{\kappa}_{mn} = \frac{\partial D_m}{\partial E_n}$$

- Piezoelectric constant  $\bar{d}_{mj}$  :

$$\bar{d}_{mj} = \frac{\partial D_m}{\partial \sigma_j} = \frac{\partial \varepsilon_j}{\partial E_m}$$

- Pyroelectric coefficients  $\bar{p}_m$  :

$$\bar{p}_m = \frac{\partial D_m}{\partial \Theta} = \frac{\partial \eta}{\partial E_m}$$

- Thermal Expansion coefficient  $\alpha_{i\_thermal}$  :

$$\alpha_{i\_thermal} = \frac{\partial \varepsilon_i}{\partial \Theta} = \frac{\partial \eta}{\partial \sigma_i}$$

- Specific heat  $c$ :

$$c_p = \Theta \frac{\partial \eta}{\rho \partial \Theta}, \text{ where } \rho \text{ is the density.}$$

The last equation in equation 2.5 represents the energy transfer by means of a heat exchange. If this energy transfer results to be zero, in other words  $dQ=0$  then we obtain the adiabatic piezoelectric equations. For example if the piezoelectric material was used in a piezoelectric vibrator with a frequency of vibration of more than  $10^4$  Hz, then the system has no time to exchange heat with the surrounding environment, thus considering that the system is adiabatic. Under these circumstances, equation 2.5 remains the same and the superscript  $E$ ,  $\Theta$  and  $\sigma$  are replaced by  $\eta$  to indicate an adiabatic condition.

Equation 2.4 and 2.5 present the constitutive equations in the strain-charge form. The electro-mechanical constitutive equations can be presented in a total of four forms. It is important to note that the thermal effects are being neglected. In this thesis the stress charge form of equations will be used.

- Strain charge form

$$\begin{aligned} \bar{\varepsilon} &= \bar{C} \bar{\sigma} + \bar{d}^T E \\ \bar{D} &= \bar{d} \bar{\sigma} + \bar{\kappa} E \end{aligned} \quad (2.6)$$

- Stress charge form

$$\begin{aligned} \bar{\sigma} &= C_{stiff} \bar{\varepsilon} - eE \\ \bar{D} &= e^T \bar{\varepsilon} + \kappa E \end{aligned} \quad (2.7)$$

where,

- $\kappa$  is the permittivity constant matrix in the stress charge form.
  - $e$  is the piezoelectric constant matrix in the stress charge form.
  - $C_{siff}$  is the elastic stiffness matrix in the stress charge form.
  - T is the transpose operator.
- Strain voltage form

$$\begin{aligned} \varepsilon &= C_v \sigma + g^T D \\ E &= -g \sigma + \kappa^{-1} D \end{aligned} \quad (2.8)$$

Where,

- $C_v$  is a compliance coefficient matrix for the strain voltage form of the constitutive equations.
  - $g$  is the piezoelectric coupling coefficient for the strain voltage form of the constitutive equations.
- Stress voltage form

$$\begin{aligned} \sigma &= C_D \varepsilon - q^T D \\ E &= -q \varepsilon + \kappa_s^{-1} D \end{aligned} \quad (2.9)$$

Where:

- $C_D$  is the stiffness matrix in the stress voltage form of the constitutive equation.
- $\kappa_s$  electric permittivity matrix for the stress voltage form of the constitutive equation.
- $q$  is the piezoelectric coupling coefficients for the stress voltage form of the constitutive equations.

The following paragraphs show how to transform the electro-mechanical equations from strain charge form to stress charge form. We start with the equation for strain in the strain charge form (equation 2.10):

$$\boldsymbol{\varepsilon} = \bar{\mathbf{C}} \boldsymbol{\sigma} + \bar{\mathbf{d}}^T \mathbf{E} \quad (2.10)$$

where,

- $\boldsymbol{\varepsilon}$  is strain
- $\boldsymbol{\sigma}$  is the stress field
- $\bar{\mathbf{C}}$  is the compliance material matrix
- $\mathbf{E}$  is the electric field
- $\bar{\mathbf{d}}$  is the piezoelectric material constant matrix.

Solving for stress we obtain:

$$\boldsymbol{\sigma} = \bar{\mathbf{C}}^{-1} \boldsymbol{\varepsilon} - \bar{\mathbf{C}}^{-1} \bar{\mathbf{d}}^T \mathbf{E} \quad (2.11)$$

Re-naming some of the components in equation 2.11 we obtain that:

$$\begin{aligned} \mathbf{e} &= \bar{\mathbf{C}}^{-1} \bar{\mathbf{d}}^T \\ \mathbf{C}_{stiff} &= \bar{\mathbf{C}}^{-1} \end{aligned} \quad (2.12)$$

Thus,

$$\boldsymbol{\sigma} = \mathbf{C}_{stiff} \boldsymbol{\varepsilon} - \mathbf{e} \mathbf{E} \quad (2.13)$$

The equation for electrical displacement in strain charge form is:

$$\mathbf{D} = \bar{\mathbf{d}} \boldsymbol{\sigma} + \bar{\kappa} \mathbf{E} \quad (2.14)$$

Where,

- $\bar{\kappa}$  is the electric permittivity in the strain charge form.

Substituting  $\sigma$  into the above equation we obtain:

$$D = \bar{d}(C_{stiff} \boldsymbol{\varepsilon} - C_{stiff} \bar{d}^T E) + \bar{\kappa} E \quad (2.15)$$

Simplifying:

$$D = d C_{stiff} \boldsymbol{\varepsilon} - (d C_{stiff} \bar{d}^T E - \bar{\kappa}) E \quad (2.16)$$

Thus,

$$e^T = \bar{d} C_{stiff} \quad (2.17)$$

and

$$\kappa = \bar{\kappa} - \bar{d} C_{stiff} \bar{d}^T \quad (2.18)$$

Where,

- $\kappa$  is the electric permittivity in the stress charge form.

Thus, the final electromechanical equations in stress charge form are:

$$\begin{aligned} \boldsymbol{\sigma} &= C_{stiff} \boldsymbol{\varepsilon} - e E \\ D &= e^T \boldsymbol{\varepsilon} + \kappa E \end{aligned} \quad (2.19)$$

Equation 2.19 in matrix form is shown in equation 2.20:

$$\begin{bmatrix} \boldsymbol{\sigma} \\ D \end{bmatrix} = \begin{bmatrix} C_{stiff} & -e \\ e^T & \kappa \end{bmatrix} \begin{bmatrix} \boldsymbol{\varepsilon} \\ E \end{bmatrix} \quad (2.20)$$

The constitutive equation in stress charge form presented in equations 2.19 and 2.20 are used in our piezoelectric solver. The solver would solve for displacement and electric potential, which can then be used to compute the strain and the electric field [5,6]. Once the displacement and electric potential are obtained, the strain and the electric field can be computed which in turn allows the stress to be calculated.

The constitutive matrix for materials with orthotropic elasticity has the following form:

$$C_{stiff} = \begin{pmatrix} M_{11} & M_{12} & M_{13} & 0 & 0 & 0 \\ M_{21} & M_{22} & M_{23} & 0 & 0 & 0 \\ M_{31} & M_{32} & M_{33} & 0 & 0 & 0 \\ 0 & 0 & 0 & M_{44} & 0 & 0 \\ 0 & 0 & 0 & 0 & M_{55} & 0 \\ 0 & 0 & 0 & 0 & 0 & M_{66} \end{pmatrix} \quad (2.21)$$

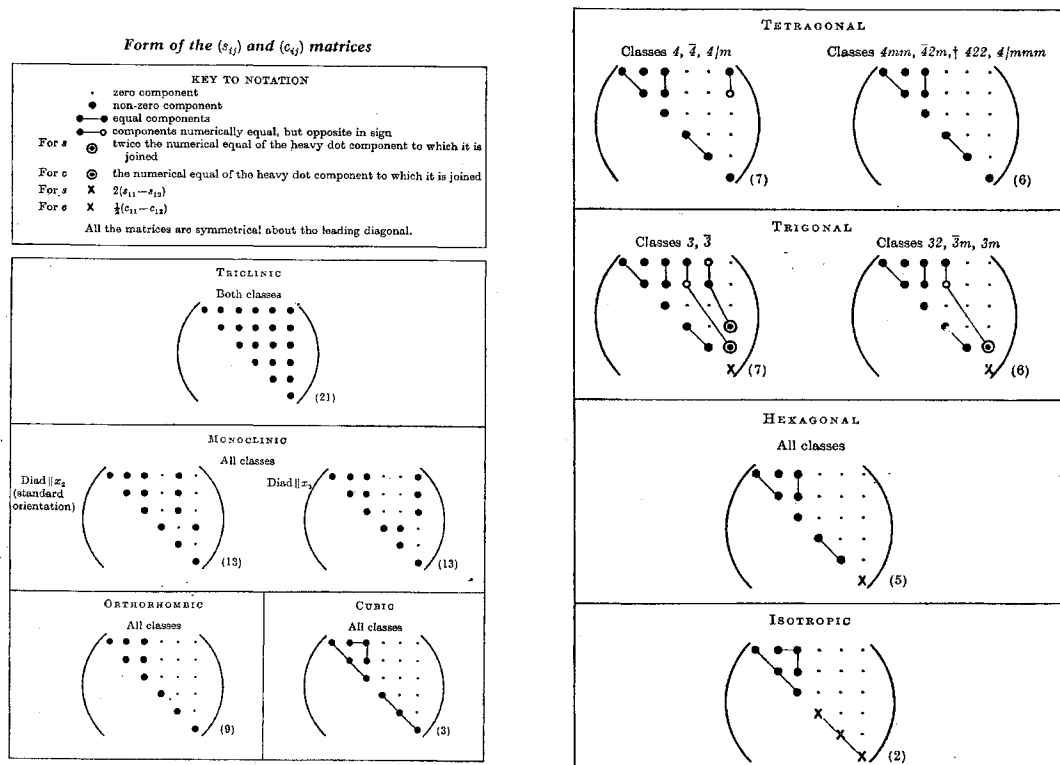
For isotropic materials:

$$M_{11} \equiv M_{22} \equiv M_{33} \equiv \frac{Y.M. \cdot (1-\nu)}{(1+\nu) \cdot (1+2\nu)}$$

$$M_{12} \equiv M_{13} \equiv M_{21} \equiv M_{23} \equiv M_{31} \equiv M_{32} \equiv \frac{Y.M. \cdot \nu}{(1+\nu) \cdot (1+2\nu)}$$

$$M_{44} \equiv M_{55} \equiv M_{66} \equiv \frac{Y.M.}{2(1+\nu)}$$

Where, Y.M. is the Young's Modulus of Elasticity. Figure 2.0 shows the elastic compliance and stiffness matrix based on the crystal symmetry. Figure 2.0 also shows the triclinic crystal structure as the most general compliance/stiffness matrix that one could simulate. However, in this thesis the focus has been placed on piezoelectric material, such as PZT-5A, that is based on a tetragonal class 4mm.



The piezoelectric constant matrix is defined by matrix  $e$ . The piezoelectric constant matrix is the mapping transformation matrix that maps electric field,  $E$ , to stress,  $\sigma$ . The transpose of the piezoelectric constant matrix determines the corresponding mapping transformation of

strain,  $\epsilon$ , to dielectric displacement,  $D$ . Equation 2.22, show the piezoelectric constant matrix for an orthorhombic crystal structure.

$$e = \begin{pmatrix} 0 & 0 & e_{31} \\ 0 & 0 & e_{32} \\ 0 & 0 & e_{33} \\ 0 & e_{24} & 0 \\ e_{15} & 0 & 0 \\ 0 & 0 & 0 \end{pmatrix} \quad (2.22)$$

The locations of the piezoelectric constants in  $e$  are dependent on the symmetry of the crystal structure as described in [1]. PZT single crystals with piezoelectric properties can have either tetragonal ( $4mm$ ) symmetry or rhombohedral ( $3m$ ). The ceramics studied in this thesis have tetragonal symmetry of properties in poled state. Figures 2.1 shows the different forms that the piezoelectric constant matrix takes depending on the symmetry and the crystal structure. The crystal structure with the most general form of piezoelectric constant matrix is the triclinic crystal arrangement [1].

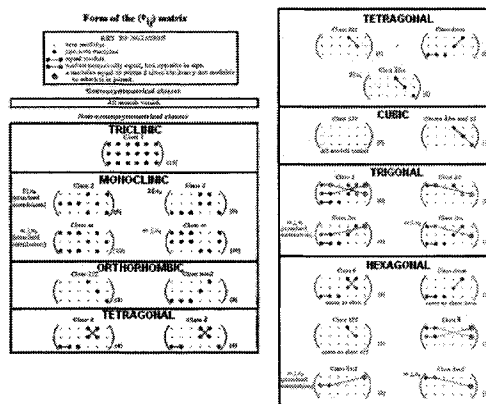


Figure 2.1: Piezoelectric Material Matrix [1]

The permittivity matrix for a tetragonal system is defined in equation 2.23. The permittivity matrix maps the electric field to the electric displacement  $\mathbf{D}$  [5,6]:

$$\boldsymbol{\kappa} = \begin{pmatrix} \kappa_{11} & 0 & 0 \\ 0 & \kappa_{22} & 0 \\ 0 & 0 & \kappa_{33} \end{pmatrix} \quad (2.23)$$

Where,  $\kappa_{11}$ ,  $\kappa_{22}$  and  $\kappa_{33}$  are the permittivity constants. The general forms for the permittivity constant matrix based on the crystal structure can be found in [1].

The complete piezoelectric material matrix ( $\mathbf{D}$ ) assuming no thermal effect is defined as [5,6]:

$$\mathbf{D} = \begin{pmatrix} M_{11} & M_{12} & M_{13} & 0 & 0 & 0 & 0 & 0 & e_{31} \\ M_{21} & M_{22} & M_{23} & 0 & 0 & 0 & 0 & 0 & e_{32} \\ M_{31} & M_{32} & M_{33} & 0 & 0 & 0 & 0 & 0 & e_{33} \\ 0 & 0 & 0 & M_{44} & 0 & 0 & 0 & e_{24} & 0 \\ 0 & 0 & 0 & 0 & M_{55} & 0 & e_{15} & 0 & 0 \\ 0 & 0 & 0 & 0 & 0 & M_{66} & 0 & 0 & 0 \\ 0 & 0 & 0 & 0 & e_{15} & 0 & \kappa_{11} & 0 & 0 \\ 0 & 0 & 0 & e_{24} & 0 & 0 & 0 & \kappa_{22} & 0 \\ e_{31} & e_{32} & e_{33} & 0 & 0 & 0 & 0 & 0 & \kappa_{33} \end{pmatrix} \quad (2.24)$$

where,

- $M_{11} = M_{22}$ ,  $M_{12} = M_{23} = M_{31} = M_{32}$  and  $M_{44} = M_{55}$
- $e_{31} = e_{32}$  and  $e_{15} = e_{24}$

- $\kappa_{11} = \kappa_{22}$ .

Figure 2.2 shows the different forms that the material stiffness matrix takes for tetragonal systems including the thermal effects [1].

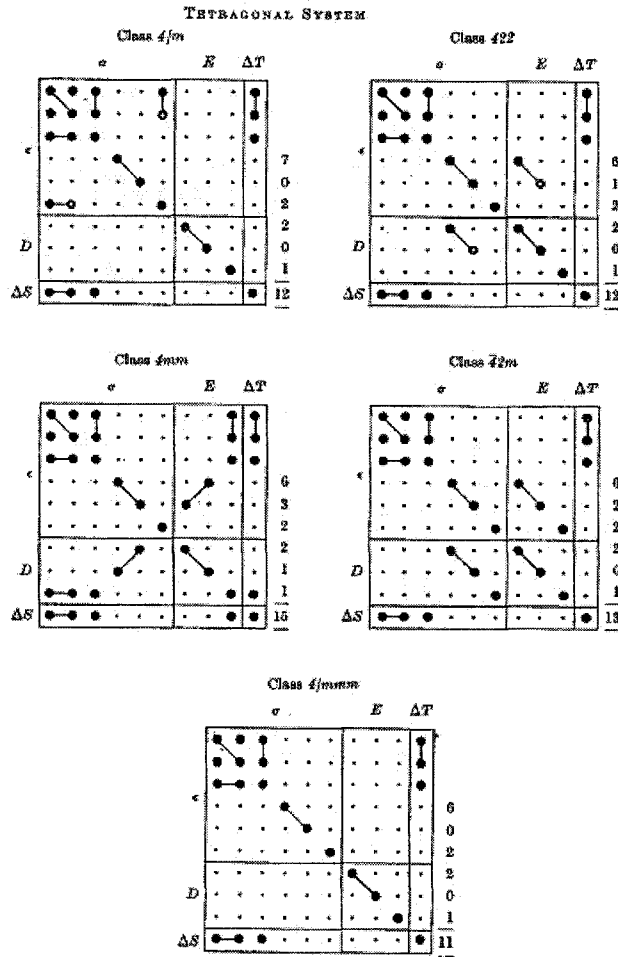


Figure 2.2: Material Stiffness Matrix for tetragonal systems [1]

## 2.2 Weak Formulation of the Electro-Mechanical Equations

This section presents the derivation of the weak formulation for the mechanical and electrical equilibrium equations. These equations are then combined with the linear electro-mechanical constitutive equations for piezoelectric structures in order to derive the complete set of equations required for modeling piezoelectric structures.

### 2.2.1 Mechanical Equilibrium equation

The conservation of momentum equation is presented in equation 2.25 as:

$$\nabla_1 \cdot \boldsymbol{\sigma} + p = \rho \frac{\partial^2 u}{\partial t^2} \quad (2.25)$$

where,

- $\rho$  is the density
- $u^T = [u_1 \quad u_2 \quad u_3]$  is the transposed (T) displacement vector
- $du^2/dt^2$  is the acceleration of the system
- $p = [p_1 \quad p_2 \quad p_3]$  is the body force
- $\boldsymbol{\sigma}^T = (\sigma_{11} \quad \sigma_{22} \quad \sigma_{33} \quad \sigma_{12} \quad \sigma_{23} \quad \sigma_{31})$  is the stress state and
- $\nabla_1 \cdot$  is the symmetric divergence operator.

$$\nabla_1 \cdot = \begin{bmatrix} \partial/\partial x_1 & 0 & 0 & \partial/\partial x_2 & 0 & \partial/\partial x_3 \\ 0 & \partial/\partial x_2 & 0 & \partial/\partial x_1 & \partial/\partial x_3 & 0 \\ 0 & 0 & \partial/\partial x_3 & 0 & \partial/\partial x_2 & \partial/\partial x_1 \end{bmatrix} \quad (2.26)$$

In our case the system is considered to be in static equilibrium, i.e., inertial forces are neglected. Thus, the mechanical equilibrium equation can be simplified to:

$$\nabla_1 \cdot \sigma + p = 0 \quad (2.27)$$

### 2.2.2 Electric equilibrium equation

The electric equilibrium equation is defined by equation 2.26:

$$\nabla D = 0 \quad (2.28)$$

where,

- $\nabla = [\partial/\partial x_1 \quad \partial/\partial x_2 \quad \partial/\partial x_3]^T$  is the gradient operator and
- $D$  is the electrical displacement.

### 2.2.3 Electromechanical Constitutive Equation

The linear coupled electro-mechanical constitutive equation is presented in equation 2.29. The mechanical equilibrium equation (2.27) and the electrical equilibrium equation (2.28) are coupled in the electromechanical constitutive equation 2.29:

$$\begin{aligned} \sigma &= C \varepsilon - e E \\ D &= e^T \varepsilon + \kappa E \end{aligned} \quad (2.29)$$

Where,

- $C_{\text{suff}}$  is stiffness material matrix (6 by 6)
- $e$  is the piezoelectric constants matrix (6 by 3)

- $\boldsymbol{\varepsilon}^T = [\varepsilon_{11} \ \varepsilon_{22} \ \varepsilon_{33} \ 2\varepsilon_{12} \ 2\varepsilon_{23} \ 2\varepsilon_{31}]$ , the strain matrix
- $\boldsymbol{\kappa}$  is the permittivity matrix (3 by 3) and
- $\mathbf{E}$  is the electric field vector,  $\mathbf{E}^T = [E_1 \ E_2 \ E_3]$ .

## 2.2.4 Weak formulation of the elastic mechanical equilibrium equation

Applying the weak formulation to the mechanical equilibrium equation we obtain:

$$\chi_1 = \int_V \delta \mathbf{u}^T (\nabla_1 \cdot \boldsymbol{\sigma} + p) dV = 0 \quad (2.30)$$

where,

- $\delta \mathbf{u}^T$  is the virtual displacement
- $V$  represents the volume of the continuum.

First we need to recall the divergence theorem which states [7,8]:

$$\int_V (\nabla \cdot \mathbf{h}) dV = \int_{\Gamma} (\mathbf{n} \cdot \mathbf{h}) d\Gamma \quad (2.31)$$

We define,

$$\mathbf{h} = f \nabla g \quad (2.32)$$

where,  $f$  and  $g$  are scalars and  $\Gamma$  represents an integral through the surface of the continuum.

By means of the divergence theorem we can obtain Green's 1<sup>st</sup> identity, which states:

$$\int_V (f \nabla^2 g) dV = \int_{\Gamma} f (\mathbf{n} \cdot \nabla g) d\Gamma - \int_V (\nabla f \cdot \nabla g) dV \quad (2.33)$$

Allowing  $\nabla g$  to be  $\boldsymbol{\sigma}$  and “ $f$ ” to be  $\delta \mathbf{u}^T$  and applying Green's first identity to the mechanical continuum equation section we obtain:

$$\int_V \delta \mathbf{u}^T (\nabla_1 \cdot \boldsymbol{\sigma}) dV = \int_{\Gamma} \delta \mathbf{u}^T (\mathbf{n} \cdot \boldsymbol{\sigma}) d\Gamma - \int_V ((\nabla_1^T \delta \mathbf{u})^T \cdot \boldsymbol{\sigma}) dV \quad (2.34)$$

Thus, the weak formulation for the mechanical equation is:

$$\chi_1 = \int_{\Gamma} \delta \mathbf{u}^T (\mathbf{n} \cdot \boldsymbol{\sigma}) d\Gamma + \int_V \delta \mathbf{u}^T (p) dV - \int_V ((\nabla_1^T \delta \mathbf{u})^T \cdot \boldsymbol{\sigma}) dV = 0 \quad (2.35)$$

In the next section we proceed to determine the weak formulation for the electrical equilibrium equation.

### 2.2.5 Weak formulation of the electrical equilibrium equation

We have applied Green's identity to the continuum equation, and now we proceed to apply the same steps to the equation below (Electrical Equilibrium equation):

$$\chi_2 = \int_V \delta \varphi^T (\nabla D) dV = 0 \quad (2.36)$$

where,

- $\delta \varphi$  is the virtual potential
- $D$  is the electric displacement.

Applying the Green's identity to the electric equilibrium equation we obtain:

$$\chi_2 = \int_V \delta \varphi (\nabla D) dV = 0 \quad (2.37)$$

By means of the divergence theorem we obtain Green's first identity, which states:

$$\int_V (f \nabla^2 g) dV = \int_{\Gamma} f (\mathbf{n} \cdot \nabla g) d\Gamma - \int_V (\nabla f \cdot \nabla g) dV \quad (2.38)$$

Allowing  $\nabla g$  to be  $D$  and “ $f$ ” to be  $\delta\phi$  and applying Green’s first identity to the mechanical continuum equation section we obtain:

$$\int_V \delta\phi(\nabla D)dV = \int_{\Gamma} \delta\phi(n \cdot D)d\Gamma - \int_V (\nabla \delta\phi)^T \cdot DdV \quad (2.39)$$

From the constitutive equations the electric field and the dielectric displacement are related by the permittivity equation.

$$D = \kappa E \quad (2.40)$$

This definition of dielectric displacement is then inserted into equation 2.41, later in the derivation. For now we will stop at the weak formulation of the electric equilibrium equation as defined by equation 2.41.

$$\int_V \delta\phi(\nabla D)dV = \int_{\Gamma} \delta\phi(n \cdot D)d\Gamma - \int_V (\nabla \delta\phi)^T \cdot DdV \quad (2.41)$$

Thus,

$$\chi_2 = \int_{\Gamma} \delta\phi(n \cdot D)d\Gamma - \int_V (\nabla \delta\phi)^T \cdot DdV \quad (2.42)$$

### 2.3 Total Weak formulation

The combined weak formulation to our problem is defined by equation 2.43 [7,8]:

$$\chi_{Total} = \chi_1 + \chi_2 = 0 \quad (2.43)$$

Thus, substituting equations (2.35) and (2.42) we obtain:

$$\chi_{Total} = \int_{\Gamma} \delta u^T (n \cdot \sigma)d\Gamma + \int_V \delta u^T (p)dV - \int_V ((\nabla_1^T \delta u)^T \cdot \sigma)dV + \int_{\Gamma} \delta\phi(n \cdot D)d\Gamma - \int_V (\nabla \delta\phi)^T \cdot DdV = 0 \quad (2.44)$$

By substituting the Electro-mechanical constitutive equations in stress-charge form

$$\begin{aligned}\sigma &= C\varepsilon - eE \\ D &= e^T \varepsilon + \kappa E\end{aligned}\tag{2.45}$$

we obtain:

$$\begin{aligned}\mathcal{X}_{Total} &= \int_{\Gamma} \delta u^T (n \cdot (C\varepsilon - eE)) d\Gamma + \int_V \delta u^T (p) dV - \int_V ((\nabla_1^T \delta u)^T \cdot (C\varepsilon - eE)) dV + \\ &\int_{\Gamma} \delta \varphi (n \cdot (e^T \varepsilon + \kappa E)) d\Gamma - \int_V (\nabla \delta \varphi)^T \cdot (e^T \varepsilon + \kappa E) dV = 0\end{aligned}\tag{2.46}$$

The next step is to expand all integrals:

$$\begin{aligned}\mathcal{X}_{Total} &= \int_{\Gamma} \delta u^T (n \cdot (C\varepsilon - eE)) d\Gamma + \int_V \delta u^T (p) dV - \int_V ((\nabla_1^T \delta u)^T C\varepsilon) dV + \int_V (\nabla_1^T \delta u)^T eE dV \\ &+ \int_{\Gamma} \delta \varphi (n \cdot e^T \varepsilon) d\Gamma + \int_{\Gamma} \delta \varphi (n \cdot \kappa E) d\Gamma - \int_V (\nabla \delta \varphi)^T \cdot (e^T \varepsilon) dV - \int_V (\nabla \delta \varphi)^T \cdot \kappa E dV = 0\end{aligned}\tag{2.47}$$

On the surface of the system:

$$\tau = n \cdot \sigma\tag{2.48}$$

where

- $\tau$  is the traction force
- $n$  is the normal vector that maps stress to traction.

Substituting  $\tau$  we get:

$$\begin{aligned}\mathcal{X}_{Total} &= \int_{\Gamma} \delta u^T (\tau) d\Gamma + \int_V \delta u^T (p) dV - \int_V ((\nabla_1^T \delta u)^T C\varepsilon) dV + \int_V (\nabla_1^T \delta u)^T eE dV \\ &\int_{\Gamma} \delta \varphi (n \cdot e^T \varepsilon) d\Gamma + \int_{\Gamma} \delta \varphi (n \cdot \kappa E) d\Gamma - \int_V (\nabla \delta \varphi)^T \cdot (e^T \varepsilon) dV - \int_V (\nabla \delta \varphi)^T \cdot \kappa E dV = 0\end{aligned}\tag{2.49}$$

The strain displacement relationship is:

$$\varepsilon = \nabla_1 \cdot u = D_u \cdot u\tag{2.50}$$

where

- $u$  is displacement.

The electric field is expressed as follows:

$$E = -\nabla\varphi = -D_\varphi^T\varphi \quad (2.51)$$

Thus substituting equation 2.50 and 2.51 into the weak formulation we obtain:

$$\begin{aligned} \mathcal{X}_{Total} = & \int_{\Gamma} \delta u^T(\tau) d\Gamma + \int_V \delta u^T(p) dV - \int_V ((\nabla_1^T \delta u)^T CD_u u) dV + \int_V (\nabla_1^T \delta u)^T e(-D_\varphi^T \varphi) dV \\ & \int_{\Gamma} \delta \varphi(n \cdot e^T D_u u) d\Gamma + \int_{\Gamma} \delta \varphi(n \cdot \kappa(-D_\varphi^T \varphi)) d\Gamma - \int_V \nabla \delta \varphi \cdot (e^T D_u u) dV \\ & - \int_V \nabla \delta \varphi \cdot \kappa(-D_\varphi^T \varphi) dV = 0 \end{aligned} \quad (2.52)$$

Simplifying:

$$\begin{aligned} \mathcal{X}_{Total} = & \int_{\Gamma} \delta u^T(\tau) d\Gamma + \int_V \delta u^T(p) dV - \int_V (\nabla_1^T \delta u)^T CD_u u dV - \int_V (\nabla_1^T \delta u)^T e D_\varphi^T \varphi dV \\ & \int_{\Gamma} \delta \varphi(n \cdot e^T D_u u) d\Gamma - \int_{\Gamma} \delta \varphi(n \cdot \kappa D_\varphi^T \varphi) d\Gamma - \int_V (\nabla \delta \varphi)^T \cdot e^T D_u u dV + \int_V (\nabla \delta \varphi)^T \cdot \kappa D_\varphi^T \varphi dV = 0 \end{aligned} \quad (2.53)$$

Grouping all volume and surface integrals we obtain:

$$\begin{aligned} \mathcal{X}_{Total} = & \int_{\Gamma} \delta u^T(\tau) d\Gamma + \int_{\Gamma} \delta \varphi(n \cdot e^T D_u u) d\Gamma - \int_{\Gamma} \delta \varphi(n \cdot \kappa D_\varphi^T \varphi) d\Gamma \\ & - \int_V (\nabla \delta \varphi)^T \cdot e^T D_u u dV + \int_V (\nabla \delta \varphi)^T \cdot \kappa D_\varphi^T \varphi dV + \int_V \delta u^T(p) dV - \int_V (\nabla_1^T \delta u)^T CD_u u dV - \int_V (\nabla_1^T \delta u)^T e D_\varphi^T \varphi dV = 0 \end{aligned} \quad (2.54)$$

We now proceed to group all the integrals that are displacement related and electric potential related:

$$\begin{aligned} \mathcal{X}_{Total} = & \int_{\Gamma} \delta u^T(\tau) d\Gamma + \int_{\Gamma} \delta \varphi(n \cdot e^T D_u u) d\Gamma - \int_{\Gamma} \delta \varphi(n \cdot \kappa D_\varphi^T \varphi) d\Gamma \\ & - \int_V (\nabla \delta \varphi)^T \cdot e^T D_u u dV - \int_V (\nabla_1^T \delta u)^T CD_u u dV + \int_V (\nabla \delta \varphi)^T \cdot \kappa D_\varphi^T \varphi dV - \int_V (\nabla_1^T \delta u)^T e D_\varphi^T \varphi dV + \int_V \delta u^T(p) dV = 0 \end{aligned} \quad (2.55)$$

At this point we proceed to re-arrange the above equation into a  $\chi_{Kx} = \chi_b$  form:

$$\begin{aligned} & \int_{\Gamma} \delta u^T(\tau) d\Gamma + \int_{\Gamma} \delta u^T(n \cdot e D_\varphi^T \varphi) d\Gamma + \int_{\Gamma} \delta \varphi(n \cdot e^T D_u u) d\Gamma - \int_{\Gamma} \delta \varphi(n \cdot \kappa D_\varphi^T \varphi) d\Gamma + \int_V \delta u^T(p) dV = \\ & + \int_V (\nabla \delta \varphi)^T \cdot e^T D_u u dV + \int_V (\nabla_1^T \delta u)^T CD_u u dV - \int_V (\nabla \delta \varphi)^T \cdot \kappa D_\varphi^T \varphi dV + \int_V (\nabla_1^T \delta u)^T e D_\varphi^T \varphi dV \end{aligned} \quad (2.56)$$

This would mean that the  $\chi_{Kx}$  form of our electromechanical problem is:

$$\chi_{Kx} = \int_V (\nabla \delta \varphi)^T \cdot e^T D_u u dV + \int_V (\nabla_1^T \delta u)^T C D_u u dV - \int_V (\nabla \delta \varphi)^T \cdot \kappa D_\varphi^T \varphi dV + \int_V (\nabla_1^T \delta u)^T e D_\varphi^T \varphi dV \quad (2.57)$$

Re-arranging:

$$\chi_{Kx} = \int_V (\nabla_1^T \delta u)^T C D_u u dV + \int_V (\nabla \delta \varphi)^T \cdot e^T D_u u dV + \int_V (\nabla_1^T \delta u)^T e D_\varphi^T \varphi dV - \int_V (\nabla \delta \varphi)^T \cdot \kappa D_\varphi^T \varphi dV \quad (2.58)$$

The gradient of the virtual displacement and the virtual potential translate into  $D_u$  and  $D_\varphi$  as shown in the equation below:

$$\begin{aligned} \nabla_1^T \delta u &= D_u \delta u \\ \nabla \delta \varphi &= D_\varphi \delta \varphi \end{aligned} \quad (2.59)$$

Then we obtain  $\chi_{Kx}$  as:

$$\chi_{Kx} = \int_V D_u^T \delta u \cdot C D_u u dV + \int_V D_\varphi \delta \varphi \cdot e^T D_u u dV + \int_V D_u^T \delta u \cdot e D_\varphi^T \varphi dV - \int_V D_\varphi \delta \varphi \cdot \kappa D_\varphi^T \varphi dV \quad (2.60)$$

It is interesting to note that the second term and the third term have a combination of  $D_u$  and  $D_\varphi$ . This would seem to indicate that a single matrix, that combines both electrical and elastic derivatives is required.

The right hand side term in 2.56 is the definition of  $\chi_b$  which is:

$$\chi_b = \int_\Gamma \delta u^T (\tau) d\Gamma + \int_\Gamma \delta \varphi (n \cdot e^T D_u u) d\Gamma - \int_\Gamma \delta \varphi (n \cdot \kappa D_\varphi^T \varphi) d\Gamma + \int_V \delta u^T (p) dV \quad (2.61)$$

The derivation of the electro-mechanical equation has been presented in this chapter. Chapter 3 focuses on the FEM as a means of solving the electro-mechanical equations required in solving structure with piezoelectric materials.

## 2.4 References for Chapter 2

- [1] Nye, “Physical Properties of Crystals”, Oxford University Press, Amen House, London E.C.4. 1964.
- [2] Finite Element Simulation of Smart Lightweight Structures for Active Vibration and Interior Acoustic Control, J. Lefevre, U. Gabbert, Technishe Mehanik, Band 23, Heft 1, (2003)59-60. Feb 2003.
- [3] Jean Lefevre, Ulrich Gabbert, Heinz Koppe, Simulation of piezoelectric controlled smart structures by the finite element method including vibroacoustic effects, Tenth International Congress on Sound and Vibration 7-10 of July 2003, Stockholm , Sweden.
- [4] Nellya N. Rogacheva, The Theory of Piezoelectric Shells and Plates, CRC Press, 1994.
- [5] <https://www.efunda.com/materials/piezo/> Last revised on January 31, 2006.
- [6] Vincent Piefort, Finite Element Modeling of Piezoelectric Active Structures, PhD. Thesis, Université Libre de Bruxelles, 2000-2001.
- [7] O.C. Zienkiewicz, K. Morgan, Finite Elements and Approximation, John Wiley and Sons, 1983.
- [8] J. Goldak, “Piezoelectric Formulation” Course Notes for Prof. Goldak Finite Element II course, Carleton University, Dept. of Mechanical and Aerospace Engineering, 2003.

FINITE ELEMENT MODEL FOR ELECTRO MECHANICAL SYSTEMS

**3.0 Introduction**

Analysis based on Finite Element Method (FEM) can be divided into the following steps:

- Development of a computer aided design (CAD) model that represents the continuum that is being analyzed.
- Meshing process, which involves the discretization of the continuum into finite elements.
- Evaluation of stiffness matrix of each element in the continuum. The evaluation of the stiffness matrix for each element is based on the nodal shape functions and the material matrix assigned to each element in the continuum.
- Assembly of the global stiffness matrix from the element stiffness matrix.
- Application of boundary conditions.

- Solving for the unknowns: In an elastic/piezoelectric structure these unknown are the nodal displacements “x”, “y” and “z” (where the boundary conditions are not applied) and nodal electric potentials,  $\phi$ .
- Post processing, which involves the computation of strain and stress fields based on the nodal displacements and electric field based on the nodal electric potentials.

The following pages will describe in detail how the mathematical equations derived in Chapter 2, are represented in FEM form.

### **3.1 Element Stiffness Matrix**

In FEM the continuum/structure is discretized into smaller parts known as elements. It is the assembly of these smaller elements that models the complete structure. Each element of the continuum may have different sizes and shapes. The degree of freedom for every node in the element is part of a series of algebraic equations. The solution to these algebraic equations can be obtained by direct or indirect mathematical methods. The solution of the algebraic equations in FEM provides an approximation to the exact solution in all parts of the continuum that has been modeled. The more elements used in the analysis of the problem the more accurate the result obtained; unfortunately the longer time required by the solver to compute the solution. Figure 3.0-a, shows a 20-node brick element, while Figure 3.0-b shows an 8-node brick element. Our piezoelectric structural solver uses 8 and 20-node brick elements to discretize the three dimensional structure.

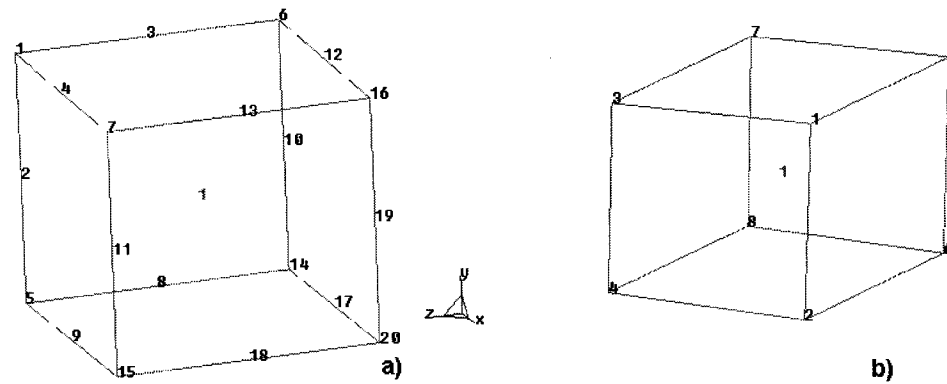


**Figure 3.0:** (a) 20 node brick element, (b) 8 node brick element

At every node in the element (every number shown in Figure 3.0 with the exception of the center number that indicates the element number) the nodal shape functions assigned to each node represent a variable number of degrees of freedoms (dof). For example, every nodal point is permitted to move in x, y and z, thus three dof. In the case of piezoelectric elements, a fourth degree of freedom, representing electrical potential, is added. The physical quantities, nodal displacement and electric potential, are described in the elements by polynomial equations known as nodal shape functions, weight functions or basis functions. These basis functions are shown in Figure 3.1 (for simplicity the shape functions for a 20-node brick element are shown only at one corner and one mid-point node). As seen in Figure 3.1, corner shape functions for a 20-node brick element have an extra term. Also, it is important to note that the mid-point shape functions for a 20-node brick are divided by four while the corner shape functions by eight. The physical quantities represented by shape functions (for example displacement or electric potential) are required to vary smoothly within the element. The assembly process (enumeration scheme) should be implemented to ensure continuity with the mesh. Thus, the element is required to have a piecewise-smooth representation of the physical quantity.

**Shape function for 8 node brick elements**

$$\text{NF}(i, x, y, z) := \begin{cases} \frac{1}{8 \cdot (a \cdot b \cdot c)} \cdot (x-a) \cdot (y+b) \cdot (z-c) & \text{if } i = 1 \\ \frac{-1}{8 \cdot (a \cdot b \cdot c)} \cdot (x-a) \cdot (y-b) \cdot (z-c) & \text{if } i = 2 \\ \frac{1}{8 \cdot (a \cdot b \cdot c)} \cdot (x-a) \cdot (y-b) \cdot (z+c) & \text{if } i = 3 \\ \frac{-1}{8 \cdot (a \cdot b \cdot c)} \cdot (x-a) \cdot (y+b) \cdot (z+c) & \text{if } i = 4 \\ \frac{-1}{8 \cdot (a \cdot b \cdot c)} \cdot (x+a) \cdot (y+b) \cdot (z-c) & \text{if } i = 5 \\ \frac{1}{8 \cdot (a \cdot b \cdot c)} \cdot (x+a) \cdot (y-b) \cdot (z-c) & \text{if } i = 6 \\ \frac{-1}{8 \cdot (a \cdot b \cdot c)} \cdot (x+a) \cdot (y-b) \cdot (z+c) & \text{if } i = 7 \\ \frac{1}{8 \cdot (a \cdot b \cdot c)} \cdot (x+a) \cdot (y+b) \cdot (z+c) & \text{if } i = 8 \\ 0 & \text{otherwise} \end{cases}$$

**Sample shape functions for a 20 node brick element**

$$\begin{cases} \frac{1}{8 \cdot a \cdot b \cdot c} \cdot [(x+a) \cdot (y+b) \cdot (z+c) \cdot (-2+x+y+z)] & \text{if } i = 1 \\ \frac{-1}{4 \cdot a \cdot b \cdot c} \cdot [(x^2 - a^2) \cdot (y+b) \cdot (z+c)] & \text{if } i = 9 \end{cases}$$

**Figure 3.1:** 8 Node brick shape functions and the sample shape functions for 20-node brick element.

Shape functions are a function of the nodal position and are equal to one, at the node in question and zero every other node.

An eight node brick has eight nodes per element (one at each corner). The number of degrees of freedom per node for this element varies from 3 per node, for elastic elements, to 4 per node for piezoelectric elements. [1]. The displacements/electric potentials in the element are represented as a sum of the nodal values times the basis functions over each element, as shown in equation 3.0 [2,3].

$$\begin{aligned} u &= N_i \cdot u_i \\ \varphi &= N_i \cdot \varphi_i \end{aligned} \tag{3.0}$$

Where,

- $u$  and  $\varphi$  are the displacement (u,v,w) and electric field respectively

- $\bar{u}_i$  and  $\bar{\varphi}_i$  is the nodal displacement ( $\bar{u}_i, \bar{v}_i, \bar{w}_i$ ) and nodal electric potential field respectively
- $N_i$  are the basis functions
- $i$  enumerates the basis function ( $i = 1$  to 8 for 8-node brick and 1 to 20 for 20-node brick).

A virtual electric potential and virtual displacement are also represented in FEM as the sum of nodal values times the basis functions over each element, as shown in equation 3.1

$$\begin{aligned}\delta \mathbf{u} &= N_i \cdot \bar{\delta \mathbf{u}}_i \\ \delta \varphi &= N_i \cdot \bar{\delta \varphi}_i\end{aligned}\quad (3.1)$$

In chapter two, we derived from the weak formulation equation 3.2, which is the starting point of our FEM solver:

$$\begin{aligned}\chi_{Kx} &= \int_V D_u^T \delta \mathbf{u} \cdot C D_u \mathbf{u} dV + \int_V D_\varphi \delta \varphi \cdot e^T D_u \mathbf{u} dV + \int_V D_u^T \delta \mathbf{u} \cdot e D_\varphi^T \varphi dV - \int_V D_\varphi \delta \varphi \cdot \kappa D_\varphi^T \varphi dV \quad (3.2) \\ \chi_b &= \int_\Gamma \delta \mathbf{u}^T (\tau) d\Gamma + \int_\Gamma \delta \varphi (n \cdot e^T D_u \mathbf{u}) d\Gamma - \int_\Gamma \delta \varphi (n \cdot \kappa D_\varphi^T \varphi) d\Gamma + \int_V \delta \mathbf{u}^T (p) dV\end{aligned}$$

- Thus, inserting equation 3.0 and 3.1 into 3.2 we obtain:

$$\begin{aligned}\chi_{Kx}^\wedge &= \int_V D_u^T N_j \cdot \bar{\delta \mathbf{u}}_j \cdot C D_u N_i \cdot \bar{\mathbf{u}}_i dV + \int_V D_\varphi N_j \cdot \bar{\delta \varphi}_j \cdot e^T D_u N_i \cdot \bar{\mathbf{u}}_i dV + \int_V D_u^T N_j \cdot \bar{\delta \mathbf{u}}_j \cdot e D_\varphi^T N_i \cdot \bar{\varphi}_i dV \\ &- \int_V D_\varphi N_j \cdot \bar{\delta \varphi}_j \cdot \kappa D_\varphi^T N_i \cdot \bar{\varphi}_i dV \quad (3.3) \\ \chi_b^\wedge &= \int_\Gamma N_j \cdot \bar{\delta \mathbf{u}}_j^T (\tau) d\Gamma + \int_\Gamma N_j \cdot \bar{\delta \varphi}_j (n \cdot e^T D_u N_i \cdot \bar{\mathbf{u}}_i) d\Gamma - \int_\Gamma N_j \cdot \bar{\delta \varphi}_j (n \cdot \kappa D_\varphi^T N_i \cdot \bar{\varphi}_i) d\Gamma + \int_V N_j \cdot \bar{\delta \mathbf{u}}_j^T (p) dV\end{aligned}$$

The insertion of the same nodal shape functions for displacements, virtual displacement and electric potentials into equation 3.2 assumes the use of the Galerkin approximation that results in a symmetric stiffness matrix K [2]. Rearranging we obtain:

$$\begin{aligned}
\chi_{\hat{k}_x} &= \bar{\delta}u_j \left[ \int_V D_u^T N_j \cdot C D_u N_i \cdot dV \right] \bar{u}_i + \bar{\delta}\varphi_j \left[ \int_V D_\varphi N_j \cdot e^T D_u N_i \cdot dV \right] \bar{u}_i + \bar{\delta}u_j \left[ \int_V D_u^T N_j \cdot e D_\varphi^T N_i \cdot dV \right] \bar{\varphi}_i \\
&\quad - \bar{\delta}\varphi_j \left[ \int_V D_\varphi N_j \cdot \kappa \cdot D_\varphi^T N_i \cdot dV \right] \bar{\varphi}_i \\
\chi_b &= \bar{\delta}u_j^T \left[ \int_\Gamma N_j \cdot (\tau) d\Gamma \right] + \bar{\delta}\varphi_j \left[ \int_\Gamma N_j \cdot (n \cdot e^T D_u N_i \cdot) d\Gamma \right] \bar{u}_i - \bar{\delta}\varphi_j \left[ \int_\Gamma N_j \cdot (n \cdot \kappa D_\varphi^T N_i \cdot) d\Gamma \right] \bar{\varphi}_i + \bar{\delta}u_j^T \left[ \int_V N_j \cdot (p) dV \right]
\end{aligned} \tag{3.4}$$

Equation 3.4 can be written in the compact form as equation 3.6 using:

$$[x] = \begin{bmatrix} - \\ u \\ \varphi \end{bmatrix} \tag{3.5}$$

$$\chi_{total} = \delta u (Kx - b) = 0 \tag{3.6}$$

where,

- $K$  represents the stiffness matrix
- $x$  represents the electric potential and nodal displacements
- $b$  represents the nodal forces acting on the system.

In order to satisfy equation 3.6,  $Kx-b$  term must be set equal to zero since the virtual displacement ( $\delta u$ ) and the virtual potentials ( $\delta\varphi$ ) cannot be set to zero.

In order to represent the forces applied to the continuum it is necessary to evaluate the  $\chi_b$  integrals presented in equation 3.4. In our solver, all body forces (for example gravity) are not considered in the solution, and only the traction (first term on the  $\chi_b$  -integral) is accounted for. Our solver evaluates the traction forces. This evaluation can be done by numerical integration, as it will be described later in this chapter. In the case of assigning traction forces to a flat

surface, the equivalent nodal forces may be assigned to each node in the element. This assignment is done in the  $b$  part of the  $Kx=b$  equation.

The assignment of traction forces, acting on the element, depends on the element that is being used to discretize the continuum. If the continuum is divided into 8-node bricks, then the contribution of forces over the surface of the element can be simply divided equally among all of the nodes that form that surface (assuming the surface is flat). If a 20-node brick element is used then the resulting force, due to the applied traction for that node, is multiplied by  $(-1/3)$  for corner nodes and by  $(4/3)$  for mid-point nodes. This is due to the fact that the 8 node brick shape functions represent the physical quantity being analyzed linearly from one node to the next, while in the case of a 20 node brick the representation is quadratic as seen in the figure below.

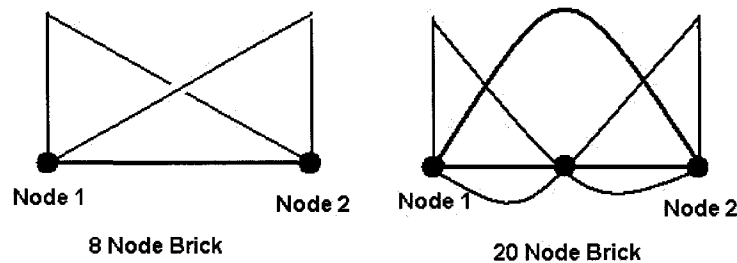


**Figure 3.2:** 8 and 20 node brick nodal shape distribution

The constants of  $-1/3$  and  $4/3$  for the application of traction on 20 node bricks comes from evaluating the first term of the  $\chi_b$ -integral (equation 3.4) for a unit traction on a flat surface. If the surface is not flat or other terms of the  $b$ -integral are required to be evaluated, the  $b$ -integral needs to be evaluated by numerical integration. This will be described later in this chapter.

Elements within the continuum are interconnected and thus interact with each other. For example, each element is required to remain attached to its neighboring elements. Thus, neighboring elements will not be allowed to overlap nor separate.

- Equations 3.4 and 3.5 represent the stiffness matrix of the element multiplied by the dof at every point in the continuum (where  $x$  represents the displacement and electrical field vector array). Equation 3.4 transforms into a FEM representation when the continuum is represented as an element or a combination of elements.

Array  $x$  contains a sequence of all dof within the elements. Some of these degrees of freedoms are known or assigned and some are not. The assigned degrees of freedoms represent the boundary conditions applied to the structure. For example, if a displacement in  $x$ ,  $y$ ,  $z$  or an electric potential is assigned at any part in the structure this would be assigned to a specific nodal element and thus be assigned to a member of array  $x$ . Therefore, only those terms in  $x$  that are unknown are solved for.

Isolating the stiffness matrix  $K$  from array  $x$  we find that the stiffness matrix can be represented as ( $K$  is represented by all term inside the brackets):

$$Kx = \left[ \int_V \bar{D}_u^T C \bar{D}_u \cdot dV \right] \bar{u} + \left[ \int_V \bar{D}_\varphi e^T \bar{D}_u dV \right] \bar{u} + \left[ \int_V \bar{D}_u^T e \bar{D}_\varphi dV \right] \bar{\varphi} - \left[ \int_V \bar{D}_\varphi \kappa \bar{D}_\varphi^T dV \right] \bar{\varphi} \quad (3.7)$$

Where,

- $\bar{D}_u$  is the matrix that maps nodal displacement to strain

- $\bar{D}_\phi$  is the matrix that maps nodal electric potentials to electric field
- $C$  is the material stiffness matrix
- $e$  is the piezoelectric material constants
- $\kappa$  is the permittivity constant matrix
- $T$  superscript represents the transpose of the matrices.

As seen in equation 3.7, the stiffness matrix of the element is computed by the summation of several volume integrals.

In the next few pages we will describe each one of these terms described in equation 3.7. The  $\bar{D}_u$  matrix defined below is the matrix that maps the nodal displacement vector array to the strain components at a point (x,y,z).

$$\left[ \bar{D}_u \right] = \begin{bmatrix} G_x & 0 & 0 \\ 0 & G_y & 0 \\ 0 & 0 & G_z \\ G_y & G_x & 0 \\ 0 & G_z & G_y \\ G_z & 0 & G_x \end{bmatrix} \quad (3.8)$$

Where,

- $G_x$  is the derivative with respect to x of the nodal shape function shown in figure 3.1
- $G_y$  is the derivative with respect to y of the nodal shape functions and
- $G_z$  is the derivative with respect to z of the nodal shape function.

The format that equation 3.8 takes has a significant meaning on how the nodal displacements are mapped to the strain tensor. The displacement vector array at every node is mapped to the Strain Voight notation at a point (x,y,z) as follows:

$$\begin{pmatrix} \epsilon_x \\ \epsilon_y \\ \epsilon_z \\ \epsilon_{xy} \\ \epsilon_{yz} \\ \epsilon_{xz} \end{pmatrix} = \left[ \bar{D}_u \right] \cdot \begin{pmatrix} u \\ v \\ w \end{pmatrix} \quad (3.9)$$

Where,

- $u, v$  and  $w$  are nodal displacements.

Shown above is a 6 by 1 strain vector. The  $D_u$  matrix for an 8 node brick would be a 6 by 24 matrix, while the nodal displacement vector would be 24 by 1 for an elastic element. In the case of a 20 node brick elastic,  $D_u$  would be 6 by 60 and the nodal displacement vector would be 60 by 1.

The  $\bar{D}_\phi$  matrix that maps the electric potential to the electric field is given by:

$$\left[ \bar{D}_\phi \right] = \begin{pmatrix} G_x \\ G_y \\ G_z \end{pmatrix} \quad (3.10)$$

The vector array of nodal voltages is mapped to the electric field gradient at a point (x,y,z) as follows:

$$\begin{pmatrix} E_x \\ E_y \\ E_z \end{pmatrix} = -\bar{D}_\phi \cdot \bar{\phi} \quad (3.11)$$

Where,

- $E_x, E_y$  and  $E_z$  are the electric field in  $x, y$  and  $z$
- $\bar{\phi}$  is the nodal electric potential

The electric field gradient is a 3 by 1 vector obtained by multiplying  $\bar{D}_\phi$  a 3 by 8 matrix, with an 8 by 1 vector of nodal potentials in the case of an 8 node brick.

The elastic material matrix represented by  $C$  in equation 3.7 is the matrix responsible for mapping the strain to stress for an isotropic material. This matrix is defined as:

$$C = \begin{pmatrix} M_{11} & M_{12} & M_{13} & 0 & 0 & 0 \\ M_{21} & M_{22} & M_{23} & 0 & 0 & 0 \\ M_{31} & M_{32} & M_{33} & 0 & 0 & 0 \\ 0 & 0 & 0 & M_{44} & 0 & 0 \\ 0 & 0 & 0 & 0 & M_{55} & 0 \\ 0 & 0 & 0 & 0 & 0 & M_{66} \end{pmatrix} \quad (3.12)$$

Where,

$$M_{11} \equiv M_{22} \equiv M_{33} \equiv \frac{Y.M. \cdot (1-\nu)}{(1+\nu) \cdot (1+2\nu)} \quad (3.13)$$

$$M_{12} \equiv M_{13} \equiv M_{21} \equiv M_{23} \equiv M_{31} \equiv M_{32} \equiv \frac{Y.M. \cdot \nu}{(1+\nu) \cdot (1+2\nu)} \quad (3.14)$$

$$M_{44} \equiv M_{55} \equiv M_{66} \equiv \frac{Y.M.}{2(1+\nu)} \quad (3.15)$$

Where,

- $Y.M.$  is the Young's Modulus of Elasticity. The matrix presented above is for an isotropic material.

The elastic stiffness material matrix for PZT-5H is:

$$[C] = \begin{bmatrix} 1.203E11 & 7.518E10 & 7.509E10 & 0 & 0 & 0 \\ 7.518E10 & 1.203E11 & 7.509E10 & 0 & 0 & 0 \\ 7.509E10 & 7.509E10 & 1.109E11 & 0 & 0 & 0 \\ 0 & 0 & 0 & 2.105E10 & 0 & 0 \\ 0 & 0 & 0 & 0 & 2.105E10 & 0 \\ 0 & 0 & 0 & 0 & 0 & 2.257E10 \end{bmatrix} \cdot \frac{N}{m^2} \quad (3.16)$$

The mapping transformation matrix that maps electric field,  $E$ , to stress,  $\sigma$ , in the strain charge form is defined as matrix  $d$  in equation 3.17.

$$d = \begin{pmatrix} 0 & 0 & d_{31} \\ 0 & 0 & d_{32} \\ 0 & 0 & d_{33} \\ 0 & d_{24} & 0 \\ d_{15} & 0 & 0 \\ 0 & 0 & 0 \end{pmatrix} \quad (3.17)$$

The transpose of  $e$  is the matrix that maps strain ( $\epsilon$ ) to dielectric displacement ( $D$ ) in the strain charge form. In the case of PZT-5A this was determined as:

$$d^T = \begin{pmatrix} 0 & 0 & 0 & 0 & 584 & 0 \\ 0 & 0 & 0 & 584 & 0 & 0 \\ -171 & -171 & 374 & 0 & 0 & 0 \end{pmatrix} \cdot 10^{-12} \cdot \frac{C}{N} \quad (3.18)$$

Since we are using the Stress-Charge form of the electromechanical coupling equations the  $d$ -matrix is transformed to the “ $e$ ” matrix (as shown in section 2.1 of chapter 2) in the following units:

$$e = \begin{pmatrix} 0 & 0 & 0 & 0 & 12.295 & 0 \\ 0 & 0 & 0 & 12.295 & 0 & 0 \\ -5.351 & -5.351 & 15.783 & 0 & 0 & 0 \end{pmatrix} \cdot \frac{s \cdot A}{m^2} \quad (3.19)$$

The permittivity constant matrix is the mapping transformation matrix that maps the electric field to the dielectric displacement in the strain charge form of the constitutive equations. This matrix is defined as [4]:

$$\bar{\kappa} = \begin{pmatrix} \kappa_{11} & 0 & 0 \\ 0 & \kappa_{22} & 0 \\ 0 & 0 & \kappa_{33} \end{pmatrix} \quad (3.20)$$

Where,  $\kappa_{11}$ ,  $\kappa_{22}$  and  $\kappa_{33}$  are the permittivity constants.

In the case of PZT-5A the permittivity matrix is as follows:

$$\bar{\kappa} = \begin{pmatrix} 1730 & 0 & 0 \\ 0 & 1730 & 0 \\ 0 & 0 & 1700 \end{pmatrix} \cdot 8.854 \cdot 10^{-12} \cdot \frac{F}{m} \quad (3.21)$$

For FEM purpose we are using the Stress-Charge form of the electromechanical coupling equation. Thus the permittivity matrix would have the following units:

$$\kappa = \begin{pmatrix} 8.137E-9 & 0 & 0 \\ 0 & 8.137E-9 & 0 \\ 0 & 0 & 7.319E-9 \end{pmatrix} \cdot \frac{s^4 A^2}{kg m^3} \quad (3.22)$$

### 3.1.1 The Jacobian Matrix

In the meshing process of the structure not all elements that describe the structure conform to perfect cubic elements, since not all structures can be fully characterized by straight lines. In

FEM the meshing program will deform the elements to better approximate the shape of the structure. When elements are geometrically deformed into different shapes in order for the elements to fit the contour of the continuum that will be analyzed (the deformation of the element in this case is not due to the application of a load but rather due to the need for the element to fit the geometry of the structure), the stiffness matrix of the element that is deformed is affected. In FEM applications, it is typical to transform the deformed element to a standard element that has an origin at the center 0,0,0 with node coordinates that range from -1,-1,-1 to +1,+1,+1 as shown in Figure 3.3.

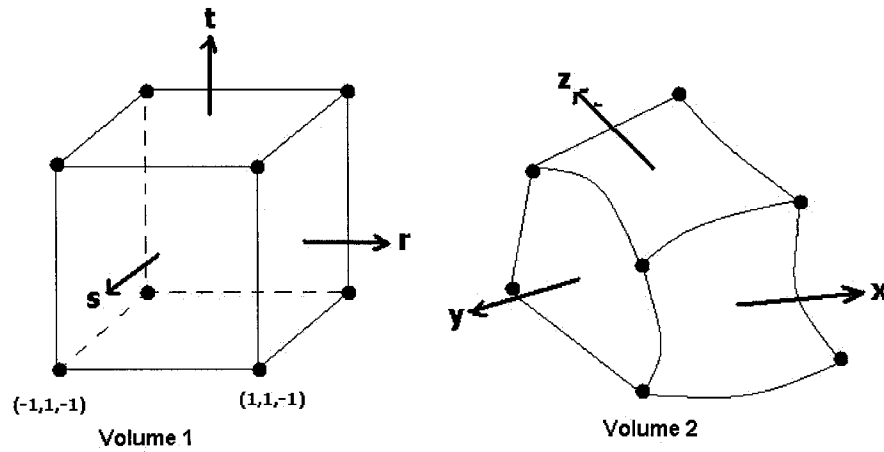


**Figure 3.3:** Jacobian Matrix Transformation

The deformed element in the Cartesian system  $(x,y,z)$ , volume 2 in Figure 3.3, is related to the standard element in the natural coordinate system  $r,s,t$ , (volume 1 in Figure 3.3). In the Cartesian coordinate system, the volume of the element, is a function of the volume of the element in the  $r,s,t$  coordinate system. In the reference element the volume integration is easily obtained and thus the stiffness matrix of the element can be computed. In order to perform

the integration for volume 2, the transformation to natural coordinates can be used and then the integrals can be obtained as:

$$\int_{v_2} f dv_2 = \int_{v_1} f \det J dv_1 \quad (3.23a)$$

where,  $\det J$  is the determinant of the Jacobian which is defined by:

$$J = \sum \begin{pmatrix} N_{i,r} x_i & N_{i,r} y_i & N_{i,r} z_i \\ N_{i,s} x_i & N_{i,s} y_i & N_{i,s} z_i \\ N_{i,t} x_i & N_{i,t} y_i & N_{i,t} z_i \end{pmatrix} \quad (3.23b)$$

where,

- $N_{i,r}$  are the derivatives of the nodal shape functions with respect to the r,s,t coordinate system
- $x, y, z$  is the point in the Cartesian coordinate system where the Jacobian is being evaluated at.

It is important to note that the Jacobian is not actually evaluated at the nodal points, but at the Gauss points of the element. An 8-node brick element usually has eight gauss points, while a twenty-node brick element usually has twenty-seven gauss points. Gauss points are points optimally placed within the volume that is being integrated. A more detail explanation of Gauss points will be described later this chapter.

The determinant of the Jacobian is then computed based on equation 3.23. Which multiplies the complete stiffness matrix at a Gauss point. In the next section we will describe how the determinant of the Jacobian affects the stiffness matrix.

### 3.1.2 Abbreviated Stiffness Matrix

Equation 3.24 is an abbreviated version of equation 3.7. In most FEM literature the stiffness matrix is described as a more concise equation, which combines all of the integrals and matrices shown in equation 3.7.

The stiffness matrix of a piezoelectric or elastic element is then computed as follows:

$$K_{piezo} = \iiint B^T \cdot \mathbf{D} \cdot B \cdot \det J \, dx dy dz \quad (3.24)$$

Where,

- $\mathbf{D}$  is the unified material matrix (equation 2.24)
- $B$  is the combined mapping transformation matrix for nodal displacement to strain and nodal electric potential to electric field
- $\det J$  is the determinant of the Jacobian.

The form of the  $B$ -matrix and the  $\mathbf{D}$ -matrix would vary if the element describes the piezoelectric effect or just the elastic effects. The next few pages will describe the combined material and  $B$ -matrix for piezoelectric and elastic effect.

### 3.1.3 Unified B-Matrix Definition

For problems where nodal displacement and electric potential are present, the generalized  $B$ -matrix is the matrix that transforms the displacement and electric potential distribution in the continuum to strain and electric field, as shown in equation 3.25.

$$\begin{pmatrix} \varepsilon \\ E \end{pmatrix} = \begin{pmatrix} \bar{D}_u & 0 \\ 0 & \bar{D}_\varphi \end{pmatrix} \cdot \begin{pmatrix} \bar{u} \\ \bar{\varphi} \end{pmatrix} \quad (3.25)$$

Where,  $u$  and  $\varphi$  are the nodal displacements in  $x, y$  and  $z$ , and the nodal electric potentials respectively. The unified B-matrix can be mathematically represented as:

$$[B] = \begin{pmatrix} G_x & 0 & 0 & 0 \\ 0 & G_y & 0 & 0 \\ 0 & 0 & G_z & 0 \\ G_y & G_x & 0 & 0 \\ 0 & G_z & G_y & 0 \\ G_z & 0 & G_x & 0 \\ 0 & 0 & 0 & G_x \\ 0 & 0 & 0 & G_y \\ 0 & 0 & 0 & G_z \end{pmatrix} \cdot \begin{pmatrix} - \\ u \\ - \\ \varphi \end{pmatrix} \quad (3.26)$$

Where,  $G_x, G_y$  and  $G_z$  are the spatial gradients of the basis functions with respect to  $x, y$  and  $z$  respectively evaluated at point  $x, y, z$ . The first 6 rows and 3 columns represent the  $D_u$  matrix of an elastic element while the last column and rows 7 to 9 represent the modification of the B-matrix in order to take into account the piezoelectric effect ( $D_\varphi$ ). It is this last column and last 3 rows that map electric potential to electric field.

### 3.2 Integration Scheme

In order to evaluate the stiffness matrix of an element it is necessary to evaluate it, by integrating over the volume of the element. Numerical integration is essential in determining the  $K$  matrix in finite element code. Numerical integration is necessary when an analytical equation is not readily available. There are many forms of numerical integration techniques,

such as the Simpson's rule, the trapezoidal rule and the Gauss rule. We will discuss very briefly the Gauss rule for a one-dimensional case.

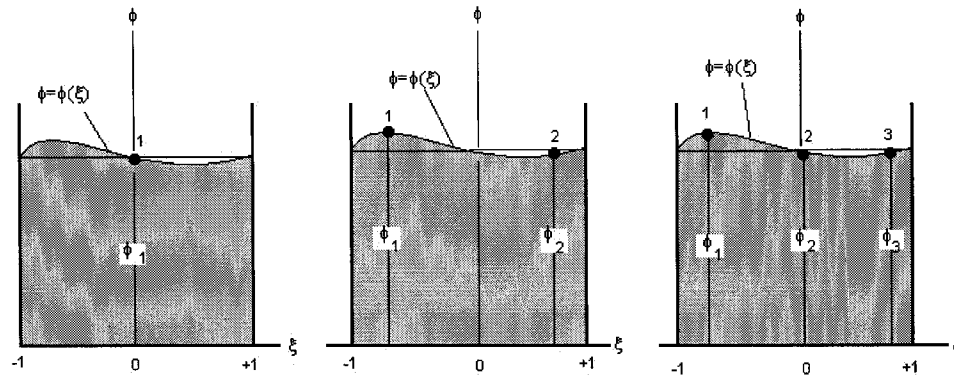


**Figure 3.4:** Gauss Numerical Integration [1]

Figure 3.4, is a 1-D diagram of how the area under the curve is obtained. This evaluation is performed using integration over the gauss points. Gauss points are points optimally placed within the area that is being integrated. Table 3.0 shows the Gauss points used for integrating over an 8-node brick element. For a 20-node brick element there are twenty-seven gauss points.

Table 3.0: Gauss Points for an 8 Node Brick Element [5]

Gauss Point No.	Gauss Point in X	Gauss Point in Y	Gauss Point in Z
1	-0.57735027	-0.57735027	-0.57735027
2	0.57735027	-0.57735027	-0.57735027
3	0.57735027	0.57735027	-0.57735027
4	-0.57735027	0.57735027	-0.57735027
5	-0.57735027	-0.57735027	0.57735027
6	0.57735027	-0.57735027	0.57735027
7	0.57735027	0.57735027	0.57735027
8	-0.57735027	0.57735027	0.57735027

The area under the curve shown in Figure 3.4 is represented by equation 3.28:

$$I = \int_{-1}^1 \phi d\xi \quad (3.28)$$

As seen in equation 3.28,  $\phi$  is a function of  $\xi$ . The area under the curve  $\phi$  can be approximated by a rectangle (base  $\cdot$  height where the height is equal to  $\phi_1$ ). The base would go from -1 to +1, thus making a base-of-length 2. The area can be computed by multiplying the base times the height, which in this case the height is equal to one. This is an exact solution for a straight line of any finite slope.

Mathematically the Gauss rule integration scheme for a 1-D case can be represented as follows:

$$I = \int_{-1}^1 \phi d\xi \approx W_1\phi_1 + W_2\phi_2 + \dots + W_n\phi_n \quad (3.29)$$

Where,  $\phi_n$  are points on the curve separated by a distance  $\xi_i$  and multiplied by a weight factor that depends on the order of the polynomial representing the function. This concept can be expanded to two and three dimensions. Our FEM solver uses Gauss integration in order to compute the stiffness matrix of the element. A generalized statement of the Gauss rules says: “a polynomial of degree  $2n-1$  is integrated exactly by  $n$ -point Gauss quadrature. Use of more than  $n$  points will still produce the exact result.” [1].

For 3-D elements if we have a quadrature formula for function of a single variable,

$$\int_{-1}^1 x^\alpha dx = \sum_{i=1}^m A_i \cdot v_i^\alpha, \quad (3.29a)$$

$$\alpha = 0, 1, \dots, d \quad (3.29b)$$

then it is not difficult to see that the integration formula:

$$\int_{-1}^1 \int_{-1}^1 \int_{-1}^1 x^\alpha y^\beta z^\gamma dz dy dx = \sum_{i=1}^m \sum_{j=1}^m \sum_{k=1}^m A_i \cdot A_j \cdot A_k \cdot v_i^\alpha \cdot v_j^\beta \cdot v_k^\gamma \quad (3.29c)$$

is also exact for  $0 \leq \alpha, \beta, \gamma \leq d$ ."

Note that products  $A_i \cdot A_j \cdot A_k$  determine weights for Gauss points with coordinates  $(x=v_i, y=v_j, z=v_k)$  and the total number of Gauss points in 3D is  $m^3$ .

In the case of the Gaussian integration scheme, the integral is evaluated at the gauss points. In the case of an 8-node brick element the weight factors are equal to one. In the case of a 20-node brick element the Gauss points and their corresponding weight factors are shown in Table 3.1. It is also important to note that a 20-node brick element integrates over 27 Gauss points while the 8-node brick element integrates over 8 Gauss points.

Table 3.1: Gauss Points and Weight Functions for 20-Node brick elements obtained using the equations in [5] and one dimensional gauss points and weight for n=3 from [6]

Gauss Point No.	Gauss Point in X	Gauss Point in Y	Gauss Point in Z	Weight Factor
1	-0.77459667	-0.77459667	-0.77459667	0.171467764
2	0.77459667	-0.77459667	-0.77459667	0.171467764
3	0.77459667	0.77459667	-0.77459667	0.171467764
4	-0.77459667	0.77459667	-0.77459667	0.171467764
5	-0.77459667	-0.77459667	0.77459667	0.171467764
6	0.77459667	-0.77459667	0.77459667	0.171467764
7	0.77459667	0.77459667	0.77459667	0.171467764
8	-0.77459667	0.77459667	0.77459667	0.171467764
9	0	-0.77459667	-0.77459667	0.274348422
10	0.77459667	0	-0.77459667	0.274348422
11	0	0.77459667	-0.77459667	0.274348422
12	-0.77459667	0	-0.77459667	0.274348422
13	-0.77459667	-0.77459667	0	0.274348422

Table 3.1-Continuation: Gauss Points and Weight Functions for 20-Node brick elements obtained using the equations in [5] and one dimensional gauss points and weight for  $n=3$  from [6]

Gauss Point No.	Gauss Point in X	Gauss Point in Y	Gauss Point in Z	Weight Factor
14	0.77459667	-0.77459667	0	0.274348422
15	0.77459667	0.77459667	0	0.274348422
16	-0.77459667	0.77459667	0	0.274348422
17	0	-0.77459667	0.77459667	0.274348422
18	0.77459667	0	0.77459667	0.274348422
19	0	0.77459667	0.77459667	0.274348422
20	-0.77459667	0	0.77459667	0.274348422
21	0	0	-0.77459667	0.438957476
22	0	-0.77459667	0	0.438957476
23	0.77459667	0	0	0.438957476
24	0	0.77459667	0	0.438957476
25	-0.77459667	0	0	0.438957476
26	0	0	0.77459667	0.438957476
27	0	0	0	0.702331962

Once the stiffness matrix for each element within the continuum is computed, it is necessary to obtain a global stiffness matrix. The following section describes how the assembly procedure is performed in order to obtain the global stiffness matrix of the continuum.

### 3.3 Assembly Procedure

The purpose of the assembly procedure is to produce a global stiffness matrix. The FEM global stiffness matrix  $K$  is shown in equation 3.30:

$$K \cdot x = b \quad (3.30)$$

Where,

- $K$  represents the FEM global stiffness matrix, which is obtained from the assembly of the individual stiffness matrix for each element
- $x$  represent the electric potential and displacement array, and
- $b$  represents the applied forces.

In the assembly process the node numbering plays an important role. Each node represents one or several degrees of freedom (dof), as shown in Figure 3.5

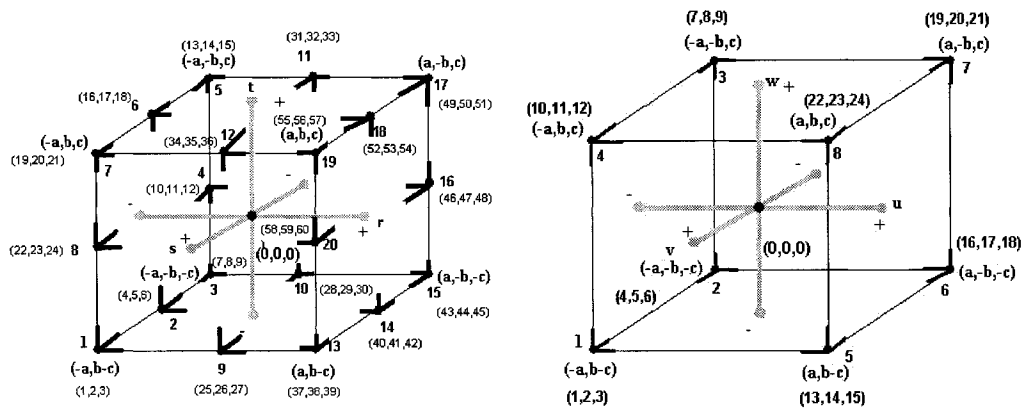


**Figure 3.5:** Degree of freedom for a 20-node brick element and 8-node brick element

The local numbering scheme for an 8-node brick is set from one to eight and it corresponds to the numbering of nodal basis functions. In the case of the 20-node brick then the numbering is set from one to twenty and it also corresponds to the basis function. The mesher assigns the global numbering scheme. A good mesher will try to have a numbering scheme as to lower the bandwidth of the assembly matrix. The numbering of the elements in the continuum is very important in order to optimize the structure of the stiffness matrix, so that it has a minimum bandwidth.

The letters a,b,c in brackets represents the coordinate points in the natural coordinate system of the element (in the case of the 20-node brick only the corner nodes are shown due to space constraint in the figure). The values of a, b and c are -1, 0 or +1 in the standard element in local coordinate systems. The numbers beside each node, in brackets, represents the degree of freedom, for example dof numbers 1, 2 and 3 represents the displacements in x, y and z directions at node 1. This indicates that the values of stiffness for node one are placed in row/columns 1, 2 and 3 in the global stiffness matrix. Every node in every element is assigned two numbers. The first number is defined in the local numbering scheme within the element, while the second number is defined in the global numbering scheme produced by the mesher/pre-processor.

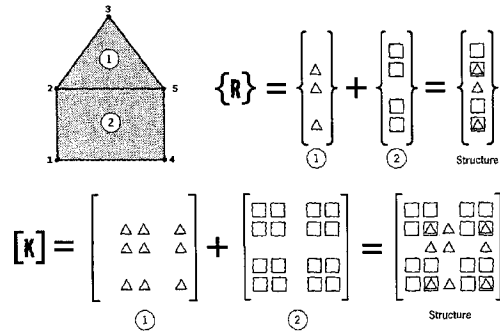


**Figure 3.6:** Assembly Procedure [1]

Figure 3.6 shows how the numbering of each node in the element indicates the contribution from local stiffness matrix in the elements of the global stiffness matrix (assuming 1 dof per node). In the case of the triangular element (1) has global node numbers 2, 3, and 5. In this case it is assumed that each node has only one degree of freedom, thus the stiffness for each degree of freedom is located in columns and rows, 2, 3, and 5. In the case of the square

element (element 2 in figure 3.6) the degree of freedoms are related to nodes 1, 2, 4 and 5. Thus, in the global stiffness matrix they would occupy row and column positions related to these degrees of freedoms, 1, 2, 4 and 5. The global stiffness matrix is the summation of the individual stiffness matrix for every element.

If the elements have more than one dof per node then the topology matrix determines the correspondence between the local numbers of dof and numbers assigned to dof in global numbering scheme. The contribution of the element stiffness matrices into the global stiffness matrix follows the same correspondence as the topology matrix.

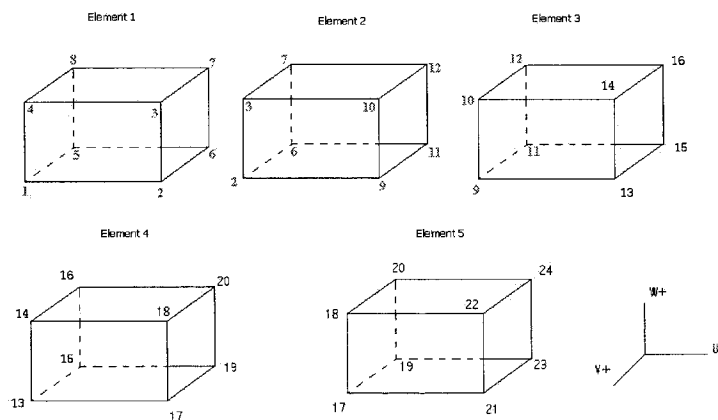


**Figure 3.7:** Topology of a 5-element beam

Figure 3.7 shows the example of the numbering scheme of 5-element beam with 3 degree of freedom per node.

The resulting global stiffness matrix would have the following shape as shown in Figure 3.8.

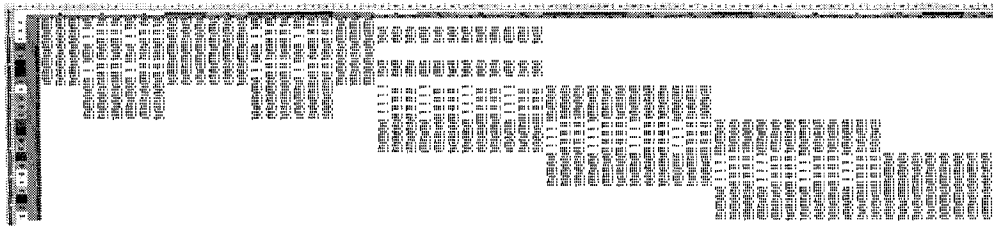


**Figure 3.8:** Global stiffness matrix of a 5 element beam

As seen in Figure 3.8 the global stiffness matrix, which is always a square matrix, has 72 rows and columns (3 degree of freedom per node • 24 dof in total). All the blank spacing in Figure 3.8 is filled with zeros, thus creating a symmetric banded matrix. The lower the band the less memory required to solve the problem. Once the global stiffness matrix is obtained it is necessary to apply the boundary condition.

### 3.4 Application of Boundary Conditions

The application of boundary conditions (B.C.) is an important step of FEM. The continuum being simulated is applied with different boundary conditions, such as B.C in terms of displacement and forces. Boundary Conditions, in terms of displacements and forces, are applied to one or more surface (or volume) of the continuum. In fully constrained B.C. one or more surfaces (or volumes) are fully fixed such that no displacement of the constrained surface is permitted. In piezoelectric structure, electric potential is assigned to different regions of the structure, which is also a B.C. In the next few paragraphs the application of B.C. on the global stiffness matrix and load vector are described.

In structural problems B.C., such as displacement and forces, are applied on the structure. The displacement and forces are applied at the nodal points. Equation 3.31 shows a simplified example of a typical FEM problem that we are trying to solve. Where  $K$  is the global stiffness matrix,  $u_1$ ,  $v_1$  and  $w_1$  represents the displacement vector ( $\times$  array) and  $f_1$ ,  $f_2$ , and  $f_3$  the forces acting on the continuum.

$$\begin{bmatrix} K_{11} & K_{12} & K_{13} \\ K_{21} & K_{22} & K_{23} \\ K_{31} & K_{32} & K_{33} \end{bmatrix} \cdot \begin{bmatrix} u_1 \\ v_1 \\ w_1 \end{bmatrix} = \begin{bmatrix} f_1 \\ f_2 \\ f_3 \end{bmatrix} \quad (3.31)$$

The applications of force B.C. are prescribed by assigning the values of forces on the force vector ( $f_1, f_2$ , and  $f_3$ ) at the required nodes. The application of traction or pressure on a surface of the continuum is performed by decomposing the normal and tangential components of the pressure/traction on the nodes of the element.

If the displacement direction  $v_1$  is set as a known displacement, then the contributions of forces corresponding to  $v_1$  are subtracted from all other nodal forces and the column and row for  $v_1$  is eliminated. Equation 3.32 shows the application of such displacement boundary condition.

$$\begin{bmatrix} K_{11} & 0 & K_{13} \\ 0 & 1 & 0 \\ K_{31} & 0 & K_{33} \end{bmatrix} \cdot \begin{bmatrix} u_1 \\ v_1 \\ w_1 \end{bmatrix} = \begin{bmatrix} f_1 - K_{12}v_1 \\ v_1 \\ f_3 - K_{32}v_1 \end{bmatrix} \quad (3.32)$$

For every displacement boundary condition, a row and column of the global stiffness matrix representing the corresponding dof is eliminated. This global stiffness matrix is further

reduced but remains a square matrix. This reduction operation results in a modified global stiffness matrix prior to solving. The final equation before solving is shown as equation 3.33:

$$\begin{bmatrix} K_{11} & K_{13} \\ K_{31} & K_{33} \end{bmatrix} \cdot \begin{bmatrix} u_1 \\ v_3 \end{bmatrix} = \begin{bmatrix} f_1 - K_{12}v_1 \\ f_3 - K_{32}v_1 \end{bmatrix} \quad (3.33)$$

Equation 3.33 is smaller in size but it is still a symmetric banded matrix.

In the case of piezoelectric structures, electric potential boundary conditions are applied. Equation 3.31 would have an extra degree of freedom, accounting for the electric potential as shown in equation 3.34:

$$\begin{bmatrix} K_{11} & K_{12} & K_{13} & K_{14} \\ K_{21} & K_{22} & K_{23} & K_{24} \\ K_{31} & K_{32} & K_{33} & K_{34} \\ K_{41} & K_{42} & K_{43} & K_{44} \end{bmatrix} \cdot \begin{bmatrix} u_1 \\ v_1 \\ w_1 \\ \phi_1 \end{bmatrix} = \begin{bmatrix} f_1 \\ f_2 \\ f_3 \\ Cf_4 \end{bmatrix} \quad (3.34)$$

Where,

- $u, v, w$  are nodal displacements
- $f_1, f_2, f_3$  are nodal forces
- $\phi$  is the electric potential and
- $Cf_4$  is the electric charge force.

The application of B.C. would be similarly performed as in equation 3.33

$$\begin{bmatrix} K_{11} & K_{12} & K_{13} & 0 \\ K_{21} & K_{22} & K_{23} & 0 \\ K_{31} & K_{32} & K_{33} & 0 \\ 0 & 0 & 0 & 1 \end{bmatrix} \cdot \begin{bmatrix} u_1 \\ v_1 \\ w_1 \\ \phi_1 \end{bmatrix} = \begin{bmatrix} f_1 - K_{14}\phi_1 \\ f_2 - K_{24}\phi_1 \\ f_3 - K_{34}\phi_1 \\ \phi_1 \end{bmatrix} \quad (3.35)$$

The units for  $K_{11}$  to  $K_{33}$  are Newton/meter. The  $x$  vector array ( $u_1, v_1$  and  $w_1$ ) also has units of meter, thus the units of  $f_1, f_2$  and  $f_3$  are all in Newton.

In the case of  $K_{14}$  the equation is still have the same form as equation 3.27 with a material matrix ( $\mathbf{D}$ ), consisting of piezoelectric constants in Amp·Sec. Thus, when multiplied by  $\mathbf{B}^T, \mathbf{B}, dx, dy$  and  $dz$ , followed by the units of electric potential (volts) in the  $x$  array we obtain force in Newton. This is shown in equation 3.35, and  $K_{24}$  and  $K_{34}$  would have the same units.

$K_{44}$  is a different case since its material matrix is formed by the permittivity constants. Thus, the units of the  $\mathbf{D}$  matrix would be in F/m when  $\mathbf{D}$  is multiplied by  $\mathbf{B}^T, \mathbf{B}, dx, dy, dz$  and electric potential (voltage) in the  $x$  array. Thus, we end up with units of Amp·Sec, which is the equivalent of a Coulomb.

It is important to note that the force boundary conditions are applied to the  $b$  array in equation 3.30, while the electric potential are assigned to the  $x$  array. The resulting equation, describing the problem, is a modified version of equation 3.30, where the global stiffness matrix  $K$ , the  $x$  array and the  $b$  force vectors are modified (as described above) and shown in equation 3.36:

$$K_{\text{mod}} \cdot x_{\text{mod}} = b_{\text{mod}} \quad (3.36)$$

The procedure shown above is used to implement boundary conditions in our FEM solver. Once the global stiffness matrix has been reduced by elimination of the columns and rows (rows filled with all zeros and a one in equation 3.32 and 3.35) the next step is solving for all unknown in the  $x$  array.

### 3.5 Solving

Solving of multiple equations is one of the primary tasks in FEM. In creating a FEM solver one can decide to use a direct or an indirect solver. Indirect solvers consist in iterative techniques such as Conjugate Gradient Methods, which will be briefly described in the sparse matrix solver section of this chapter [7, 8]. Many techniques exist in direct solvers, this thesis will briefly explain some of the most common direct methods for solving multiple linear equations. Equation 3.36 is the equation being solved:

$$K_{\text{mod}} \cdot x_{\text{mod}} = b_{\text{mod}}$$

The  $x$  array represents all of the unknowns, the  $b$  vector array all of the known and the  $K$  matrix the final stiffness matrix with boundary conditions applied.

The  $x$  array can be obtained by multiplying the inverse of the stiffness matrix with the  $b$  array as shown in equation 3.37:

$$x_{\text{mod}} = K_{\text{mod}}^{-1} \cdot b_{\text{mod}} \quad (3.37)$$

Our finite element analysis solver uses an off-the-shelf matrix inversion code [9]. The solution for nodal displacement and electric potential is obtained by multiplying the inverse matrix by the assigned nodal forces as shown in equation 3.37. This method of solving resulted in a very inefficient method for solving linear equations, due to the amount of computational resources (memory) required in order to carry out the inverse matrix operation. Our initial attempts stored the complete stiffness matrix and inverted it; this prohibits us from analyzing problems with more than a few hundred elements. It was then necessary to modify the inversion code and use a symmetric band stiffness matrix (all off diagonal non zeros past a specific band are not stored). This aided in allowing us to double the amount of elements that we could analyze. Under these conditions we can run up to 1,000 element 20-node bricks and 6,000 8-node brick elements. This consumes in the order of 2 Gigabytes of memory, which is the upper limit of a 32-bit application in a Microsoft Windows operating system. Future work in this code will require the modification of the solving method. Some of the possible methods used are briefly described next.

Several direct methods for solving system of linear equations exist, such as:

- Gaussian Elimination with back substitution
- Gauss-Jordan elimination
- Sparse Linear System Solvers with direct or indirect method of solving.

### 3.5.1 Gaussian Elimination with back substitution

In Gaussian elimination the stiffness matrix is not fully reduced to the identity matrix, in order to obtain the inverse of the matrix but only half way as to obtain the following matrix:

$$\begin{bmatrix} a_{11} & a_{12} & a_{13} & a_{14} \\ 0 & a_{22} & a_{23} & a_{24} \\ 0 & 0 & a_{33} & a_{34} \\ 0 & 0 & 0 & a_{44} \end{bmatrix} \cdot \begin{bmatrix} x_1 \\ x_2 \\ x_3 \\ x_4 \end{bmatrix} = \begin{bmatrix} b_1 \\ b_2 \\ b_3 \\ b_4 \end{bmatrix} \quad (3.38)$$

Where,

- $a_{xx}$  and  $b_{xx}$  coefficients are not the original matrix values, but modified in order to obtain the lower triangle filled with zeros. The reduction of the original matrix and the  $b$  vector array is performed by row operations.
- $x_i$  are the unknowns in question.

The form of equation 3.38 allows immediately for the solution of  $x_4$  since it is already isolated. This can be used to solve  $x_3$ . Solving for  $x_3$  allows solving  $x_2$  and so forth. This procedure is known as back substitution and can be mathematically described as [7]:

$$x_i = \frac{1}{a_{ii}} \left[ b_i - \sum_{j=i+1}^N a_{ij} x_j \right] \quad (3.39)$$

Where,

- N is the number of unknowns.

### 3.5.2 Gauss Jordan elimination

The Gauss Jordan elimination method is one of the most reliable methods for solving linear equations. It is not as fast as the Gaussian elimination method. It solves the inverse of the matrix. This provides an advantage that if the  $b$  vector array ever changes it will not be necessary to compute the inverse matrix since it has previously been computed.

Gauss Jordan elimination consists in the application of 3 operations to the following equation:

$$\begin{bmatrix} a_{11} & a_{12} & a_{13} & a_{14} \\ a_{12} & a_{22} & a_{23} & a_{24} \\ a_{13} & a_{23} & a_{33} & a_{34} \\ a_{14} & a_{24} & a_{34} & a_{44} \end{bmatrix} \cup \begin{bmatrix} x_1 \\ x_2 \\ x_3 \\ x_4 \end{bmatrix} \cup \begin{bmatrix} y_{11} & y_{12} & y_{13} & y_{14} \\ y_{12} & y_{22} & y_{23} & y_{24} \\ y_{13} & y_{23} & y_{33} & y_{34} \\ y_{14} & y_{24} & y_{34} & y_{44} \end{bmatrix} = \begin{bmatrix} b_1 \\ b_2 \\ b_3 \\ b_4 \end{bmatrix} \cup \begin{bmatrix} 1 & 0 & 0 & 0 \\ 0 & 1 & 0 & 0 \\ 0 & 0 & 1 & 0 \\ 0 & 0 & 0 & 1 \end{bmatrix} \quad (3.40)$$

Where,

- U is the augmentation operator.

In this case the following operations are performed, as explained in the book Numerical Recipes in C:

- “Interchanging any two *rows* of  $\mathbf{A}$  and the corresponding *rows* of the  $\mathbf{b}$ 's and of  $\mathbf{1}$ , does not change (or scramble in any way) the solution  $\mathbf{x}$ 's and  $\mathbf{Y}$ . Rather, it just corresponds to writing the same set of linear equations in a different order.

- Likewise, the solution set is unchanged and in no way scrambled if we replace any row in  $\mathbf{A}$  by a linear combination of itself and any other row, as long as we do the same linear combination of the rows of the  $\mathbf{b}$ 's and  $\mathbf{1}$  (which then is no longer the identity matrix, of course).
- Interchanging any two *columns* of  $\mathbf{A}$  gives the same solution set only if we simultaneously interchange corresponding *rows* of the  $\mathbf{x}$ 's and of  $\mathbf{Y}$ . In other words, this interchange scrambles the order of the rows in the solution. If we do this, we will need to unscramble the solution by restoring the rows to their original order.”, [7], page 37.

The result of these three operations is an  $\mathbf{A}$  matrix that transforms to the Identity matrix, a  $\mathbf{Y}$  matrix that becomes the inverse of the original  $\mathbf{A}$  matrix and the solution to the equations on the right hand side of equation 3.40.

As part of the Gauss Jordan elimination method the division of rows by diagonal elements are required. In some cases the diagonal element will be zero. In this case Gauss Jordan would produce division by zero during implementation. For this reason it is necessary to apply a pivoting technique. The pivoting technique consists of the re-arrangement of rows (or rows and columns) in order to have a diagonal element in the desired location, from which the element is to be taken from and which has a non-zero value. Since we don't wish to alter the identity matrix that has been produced till the encountering of the zero diagonal elements, we proceed to choose the element on the row or below the row we are about to normalize.

From memory consumption point of view the storage of the identity matrix is not required since it is a very simple matrix that is zero everywhere and ones at the diagonal. The inverse  $\mathbf{A}$  is built up in the  $\mathbf{A}$  matrix storage space. The results to the solution of equations can be built up in  $\mathbf{b}$  since once the columns of  $\mathbf{A}$  have been transformed; the row in  $\mathbf{b}$  is not used again.

### 3.5.3 Sparse Linear Systems

In solving a system of linear equations the global stiffness matrix is filled with mostly zeros, this creates very large global stiffness matrices that consume a large amount of the available system memory. Sparse linear solvers take advantage of only storing the non-zero values thus, saving time and space.

A sparse matrix may have different patterns of sparsity. Some sparse matrixes are more complicated to solve than others. Figure 3.9, shows some of these typical patterns of sparsity.

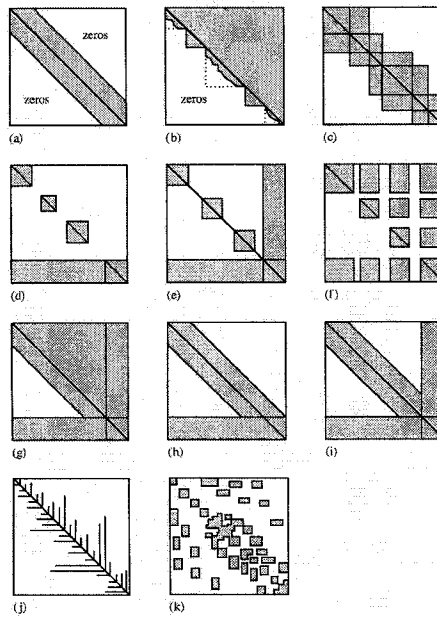


Figure 3.9: Sparsity patterns [7]

- a) Band diagonal,
- b) Block triangular,
- c) Bloc tridiagonal,
- d) Singly bordered block diagonal,
- e) Doubly bordered block diagonal,
- f) Singly bordered block triangular,
- g) Bordered band –triangular,
- h) Singly bordered band diagonal
- i) Doubly bordered band diagonal,
- j) and k) others.

Our solver stores the global stiffness matrix as a band diagonal. Several techniques can be used to solve a linear system of equations as described. This thesis will concentrate on briefly

describing the sparse matrix memory allocation technique, followed by a brief explanation of the Conjugate Gradient Method for Sparse Systems in the indirect method approach.

### 3.5.3.1 Sparse Matrix memory allocation

One of the primary advantages of the memory allocation of a sparse matrix system is that only the numbers of the matrix that are non-zero are stored. This can be seen in the following example of a matrix of the form of equation 3.41:

$$[K_{sym}] = \begin{bmatrix} 9 & 3/2 & 6 & 3/4 & 3 \\ 3/2 & 1/2 & 0 & 0 & 0 \\ 6 & 0 & 1/2 & 0 & 0 \\ 3/4 & 0 & 0 & 5/8 & 0 \\ 3 & 0 & 0 & 0 & 16 \end{bmatrix} \quad (3.41)$$

Matrix  $K_{sym}$  (considered a symmetrical sparse matrix) would be stored in a 1-D array in the form of:

$$\begin{aligned} [A] &= [9 \ 3/2 \ 6 \ 3/4 \ 3 \ 1/2 \ 1/2 \ 5/8 \ 16] \\ [Col] &= [1 \ 2 \ 3 \ 4 \ 5 \ 2 \ 3 \ 4 \ 5] \\ [Row] &= [1 \ 6 \ 7 \ 8 \ 9 \ 10] \end{aligned} \quad (3.42)$$

Since the matrix is symmetrical we only need to store the non-zero elements in the upper triangle of the matrix, including the diagonal of the matrix.

This type of storage produces a very compressed matrix that will only store the necessary values in order to perform the operations required to produce the solution to a set of linear system equations.

### 3.5.3.2 Conjugate Gradient Method for Sparse System

The conjugate gradient method is an iterative solution to the system of linear equations of equation 3.30:

$$K \cdot x = b$$

The method allows for the solution to  $N \times N$  linear systems, based on the minimization of equation 3.43:

$$f(x) = \frac{1}{2} x \cdot K \cdot x - b \cdot x \quad (3.43)$$

The minimization of equation 3.43 is done through the minimization of the gradient of  $f(x)$ .

When the gradient of  $f(x)$  is zero we obtain the equivalent of the equation  $Kx=b$ . Equation 3.44 shows the gradient of  $f(x)$ :

$$\nabla f = K \cdot x - b \quad (3.44)$$

The solving procedure is described in Numerical Recipes in C [7, page 84]:

“The minimization is carried out by generating a succession of search directions  $\mathbf{p}_k$  and improved minimizers  $\mathbf{x}_k$ . At each stage a quantity  $a_k$  is found that minimizes  $f(\mathbf{x}_k + a_k \mathbf{p}_k)$ , and  $\mathbf{x}_{k+1}$  is set equal to the new point  $\mathbf{x}_k + a_k \mathbf{p}_k$ .

The  $\mathbf{p}_k$  and  $\mathbf{x}_k$  are built up in such a way that  $\mathbf{x}_{k+1}$  is also the minimizer of  $f$  over the whole vector space of directions already taken,  $\{\mathbf{p}_1, \mathbf{p}_2, \dots, \mathbf{p}_k\}$ . After  $N$  iterations you arrive at the minimizer over the entire vector space, i.e., the solution to the equation”

This method of solving and storing large matrix will be part of the future work required to improve our solver. The need to solve larger systems is evident due to the limitations when the complete global stiffness band matrix is stored in memory and inverted (maximum of 2 Gigabyte memory for Win 32 bit applications in Microsoft Windows). In our solver this limitation is reached when a structure is modeled with approximately 1,000 elements 20-node brick and 6,000 elements 8-node bricks.

### **3.6 Post-Processing**

The post processing consists in the calculation and graphic representation of:

- Strain field,
- Stress field.

The following sections will describe how each parameter is obtained.

### 3.6.1 Strain field

The strain field is obtained from the displacement field. The strain is computed at the gauss points of each element. The strain is obtained by using equation 3.9:

$$\begin{pmatrix} \epsilon_x \\ \epsilon_y \\ \epsilon_z \\ \epsilon_{xy} \\ \epsilon_{yz} \\ \epsilon_{xz} \end{pmatrix} = [D_u] \cdot \begin{pmatrix} u \\ v \\ w \end{pmatrix}$$

Where  $u$ ,  $v$  and  $w$  represent the displacement fields as indicated by equation 3.0, while  $D_u$  represent the gradient of the nodal shape functions, as shown in equation 3.8. The displacement field and the electric potential are obtained directly from solving equation 3.37. The electric potential field and displacement field are evaluated at the nodes (vs. gauss points) and stored in a text file for GID (pre/post processor) to transform the displacement and electric potential field into a graphical representation.

The strain is computed at every gauss point within the element. In the case of an 8-node brick this represents 8 gauss points while in the case of 20-node bricks we compute  $D_u$  at 27 gauss points. The result of this computation is then printed out to a text file in the following form:

**Table 3.2:** Example of Strain Output at one nodal point

Nodal Point	$\epsilon_{xx}$ -Strain	$\epsilon_{yy}$ -Strain	$\epsilon_{zz}$ -Strain	$\epsilon_{xy}$ -Strain	$\epsilon_{yz}$ -Strain	$\epsilon_{xz}$ -Strain
1	-2.6e-9	5.2e-10	6.9e-18	-5.6e-5	-5.7e-10	-0.00213
	-1.11e-9	5.21e-10	-1.38e-17	-5.83e-5	-7.22e-10	-0.00223
	-1.11e-9	7.67e-10	-6.93e-18	-5.83e-5	-2.21e-10	-0.0022
	-2.66e-9	7.64e-10	4.33e-18	-5.68e-5	-3.57e-10	-0.0021
	6.16e-10	7.66e-10	1.73e-17	0.000109	-5.88e-10	-0.0021
	1.66e-9	7.76e-10	0	0.000116	-7.71e-10	-0.0022
	1.665e-9	5.29e-10	-2.08e-17	0.00011	-1.75e-10	-0.0022
	6.1602e-10	5.32e-10	2.75e-17	0.000109	-3.49e-10	-0.00214

The results are printed to a text file with the name of mesh.res. This file contains information on the displacement field, electric potential field, strain field (shown in Table 3.2) and the stress field. The calculation of the stress field is shown next.

### 3.6.2 Stress field

The stress field is computed as a two-step process as indicated by the electromechanical constitutive equations shown in Chapter 2 (equation 2.19):

$$\boldsymbol{\sigma} = \mathbf{C}_{siff} \boldsymbol{\epsilon} - eE$$

The material matrix  $\mathbf{C}_{siff}$  (a 6 by 6 matrix) is multiplied with the strain vector evaluated at every gauss points (a 6 by 1 vector as shown in table 3.1). The result of this is stored in memory until

the contribution of the stress, due to the electric field, is obtained. The calculation of the stress contribution, due to the electric field, is computed by multiplying the piezoelectric constant matrix “ $\epsilon$ ” (Equation 3.19) with the electric field vector (a 3 by 1 vector). The two stress terms are then subtracted as described by the electro-mechanical constitutive equation. The results obtained at each gauss points are saved to the mesh.res file in the same format as described in Table 3.1. These results are then read by the pre/post processor and transformed by GID into a graphical representation of the strain and stress field.

### **3.7 Summary**

This chapter shows the equations used in the calculation of the stiffness matrix for a piezoelectric element. The FEM analysis equations are reviewed and how the different steps for assembly, boundary conditions and solving are evaluated. Finally the post processing equations are also described. Chapter 4 will present the validation problems for the elastic and piezoelectric elements.

### **3.8 References for Chapter 3**

- [1] Robert D. Cook, David S. Malkus, Michael E. Plesha, Concepts and Applications of Finite Element Analysis, 3<sup>rd</sup> Edition, Published by John Wiley & Sons 1989.
- [2] O.C. Zienkiewicz, K. Morgan, Finite Elements and Approximation, John Wiley and Sons, 1983.

- [3] J. Goldak, "Piezoelectric Formulation" Course Notes for Prof. Goldak Finite Element II course, Carleton University, Dept. of Mechanical and Aerospace Engineering, 2003.
- [4] ] Nye, "Physical Properties of Crystals", Oxford University Press, Amen House, London E.C.4. 1964.
- [5] A.H. Stroud, D. Secrest, Gaussian Quadrature Formulas, Prentice Hall, 1966.
- [6] Handbook of Mathematical Functions with Formulas, Graphs, and Mathematical Tables  
Edited by: Abramowitz, M.; Stegun, I.A., National Bureau of Standards, 1964.
- [7] William H. Press, Saul A. Teukolsky, William T. Vetterling, Brian P. Flannery, Numerical Recipes in C, The Art of Scientific Computing 2<sup>nd</sup> Edition, Cambridge University Press, 1988.
- [8] [http://netlib2.cs.utk.edu/linalg/html\\_templates/node20.html](http://netlib2.cs.utk.edu/linalg/html_templates/node20.html) (Last accesses Feb. 21st-06)
- [9] <http://www.robertnz.net/> (Last accessed February 4, 2006).

## FINITE ELEMENT SOLVER VALIDATION

### **4.0 Introduction**

A series of validation tests for elastic and piezoelectric elements were conducted. A set of standard tests developed by McNeal and Harden [1] is used to determine the accuracy of elastic elements. The intentions of these tests are not for testing the efficiency of the solver, since they are small in the number of elements used, but instead to test the accuracy of the elements under different conditions. Not all of the McNeal and Harden tests were implemented since it is not the intention of the author to create a universal solver. It is the primary intention of the author to prove the use of finite element methods (FEM) as a means of solving problems that use piezoelectric elements and the limitations of the developed elements under different type of deformations.

In FEM it is necessary to assure that the results obtained are accurate. The MacNeal and Harden problem tests provide a means for testing the accuracy of the elements and all of the functions that comprise a finite element solver. The proposed tests by MacNeal and Harden for solid elements are [1]:

- Patch test
- Straight cantilever beam
- Curved beam

- Twisted beam
- Rectangular plate
- Scordelis-Lo Roof
- Spherical Shell
- Thick-Walled Cylinder.

All of the tests mentioned above are required to proof the performance of any finite element code that is intended as a universal solver that uses solid elements. The FEM solver that we have developed is not a universal solver and it is not intended to be one at this time. As part of this thesis we have implemented the patch test, straight cantilever beam and the rectangular plate test. We have selected these tests because they are relevant to the type of problems which were studied. In the case of piezoelectric elements a set of standard tests are not available. Thus, we have proposed a series of tests that for which analytical solutions are available.

#### 4.1 Patch Test

In order to assure convergence to the exact solution, R. Cook, D. Malkus and M. Plesha [2] describe three requirements:

1. The field that is computed (say displacement  $u$ ) within each element must be represented by a complete polynomial of degree  $m$ . It is said that a polynomial is complete when it is of high enough term to represent the exact solution.
2. Continuity must exist for the described field and its derivatives (order  $m-1$ ) along the boundaries of the element.

3. The continuum can be described as a mesh by means of the elements. Boundary conditions on the mesh are assigned a constant value of any of the derivatives of the displacement field. As the mesh is refined the elements must display the constant value assigned.

The patch is one of the required tests to pass when developing a solid element. A successful pass of the patch test guarantees that the mathematics developed in chapter three for the element have been derived correctly and properly translated into a computer code.

The patch test is also a necessary condition in order to assure that the element used in the FEM model converges to an exact solution of the problem, as the mesh of the continuum is refined.

The first step in implementing the patch test is to create a mesh of elements as described in Figure 4.1. The locations of all internal nodes in the patch test are found in Table 4.1.

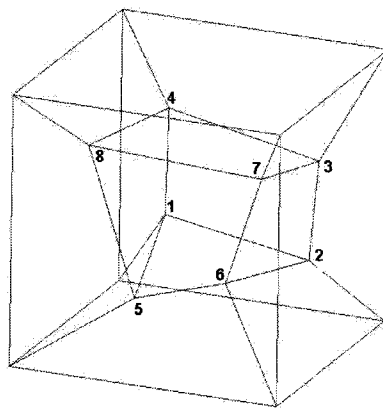


**Figure 4.1:** Patch Test.

**Table 4.1:** Location of the internal nodes in the Patch Test.

Point No.	X	Y	Z
1	0.249	0.342	0.192
2	0.826	0.288	0.288
3	0.850	0.649	0.263
4	0.273	0.750	0.230
5	0.320	0.186	0.643
6	0.677	0.305	0.683
7	0.788	0.693	0.644
8	0.165	0.745	0.702

MacNeal and Harden provide the material properties and the boundary conditions for the solid patch test. They set the Young's Modulus of elasticity,  $E$ , to 1.0E6 and the Poissons ratio to 0.25.

After the mesh has been created, the boundary conditions are set as displacement at each corner nodes as a function of  $x, y$  and  $z$  as shown in equation 4.1:

$$\begin{aligned}u &= 10^{-3}(2x + y + z)/2 \\y &= 10^{-3}(x + 2y + z)/2 \\z &= 10^{-3}(x + y + 2z)/2\end{aligned}\tag{4.1}$$

The theoretical solution to the patch test problem is given by:

$$\begin{aligned}\epsilon_x = \epsilon_y = \epsilon_z = \gamma_{xy} = \gamma_{yz} = \gamma_{zx} &= 10^{-3} \\ \sigma_x = \sigma_y = \sigma_z = 2000; \tau_{xy} = \tau_{yz} = \tau_{zx} &= 400\end{aligned}\tag{4.2}$$

The results of patch test on 20-node bricks are described next. Our 20-node brick element passes the patch test, as seen in the figures below. All of the normal stresses and shear stresses agree with the theoretical results presented in equation (4.2).

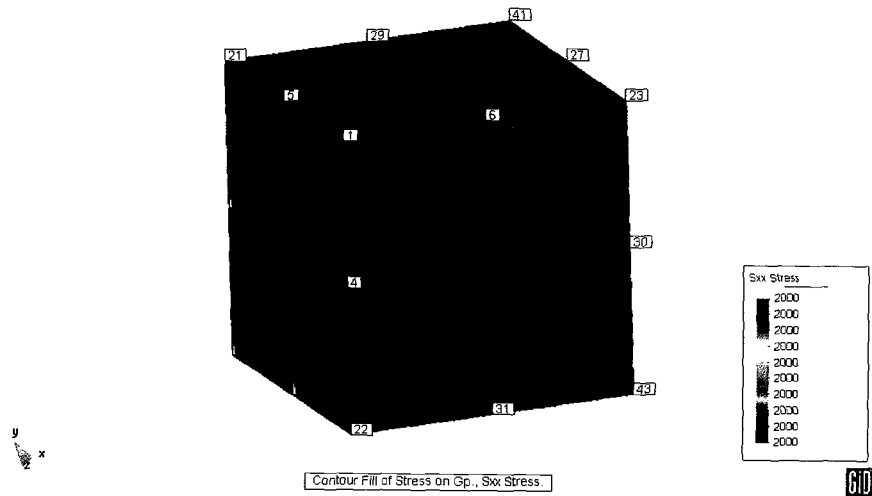


Figure 4.2:  $\sigma_{xx}$  results on 20-node brick patch test.

Figure 4.3 shows the results of the shear stress on the 20-node brick patch test.

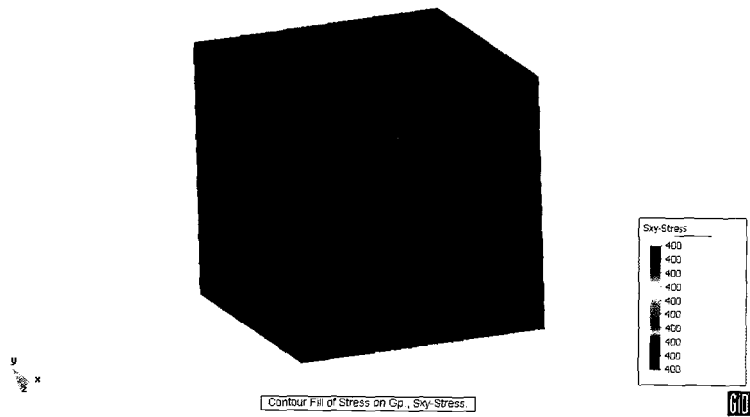


Figure 4.3:  $\tau_{xy}$  shear stress on 20-node brick patch test.

As seen in the results presented above, we can conclude that the 20-node brick element passes the patch test problem.

The patch test was also performed on the 8-node brick and the results produced are exactly the same as those produced for a 20-node brick.

## 4.2 Straight cantilever beam test

Figure 4.4 shows the types of elements used for the straight cantilever beam test. Type *a*, element has a rectangular shape, while *b* is trapezoidal and *c* is a parallelogram element. In all three cases a load tip is applied to create a deformation in extension, in-plane shear and out-of-plane shear. The load tip of in-plane and out-of-plane shear produces bending deformation of the beam. All beams have been meshed with a total of six elements along the length and one element through the height and thickness, as seen in Figure 4.4.

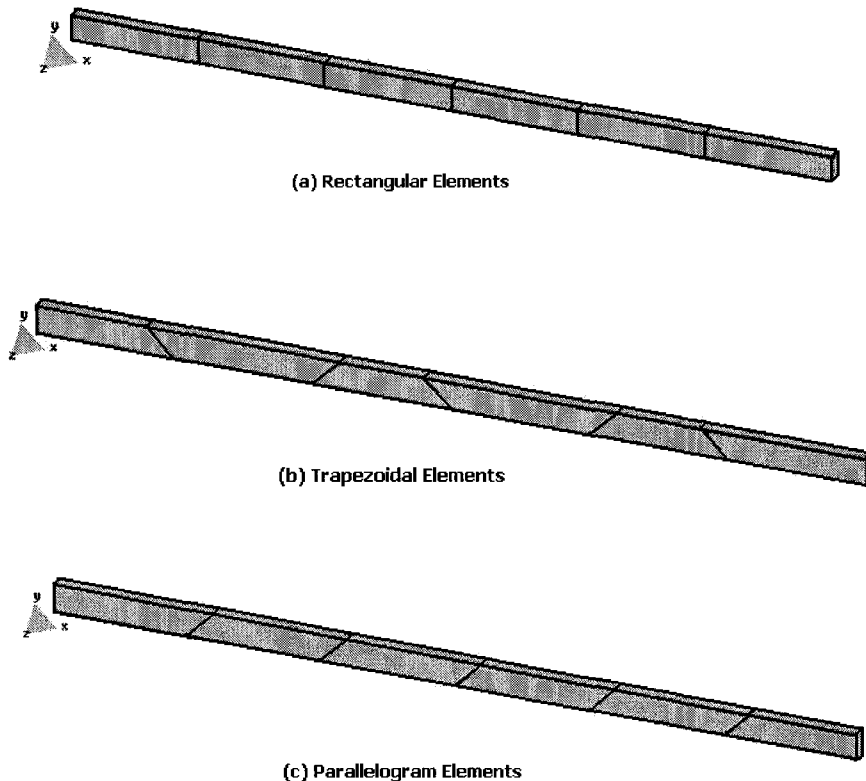


**Figure 4.4:** Straight Cantilever Beam, a) with rectangular elements, b) with trapezoidal elements and c) with parallelogram elements.

The straight cantilever beam has a length of 6 units, a depth of 0.1 units and a width of 0.2 units. The material properties for this elastic beam are set to have a Young Modulus of  $1.0E7$  and Poisson ratio of 0.3. Table 4.2 shows the theoretical displacement and the corresponding results for 8 and 20-node brick elastic elements.

**Table 4.2:** Straight Cantilever Beam for 20-Node Brick Elements.

Tip load direction <sup>¥</sup>	Displacement in direction of load		
	Straight Beam Theoretical	20-Node Brick Results	Percentage Difference
Extension (type a)	3.0E-5	2.98E-5	0.66%
Extension (type b)	3.0E-5	2.99E-5	0.33%
Extension (type c)	3.0E-5	2.99E-5	0.33%
In Plane Shear (a)	0.1081	0.1049	2.96%
In Plane Shear (b)	0.1081	0.0955	11.66%
In Plane Shear (c)	0.1081	0.1044	3.42%
Out of Plane Shear (a)	0.4321	0.4151	3.93%
Out of Plane Shear (b)	0.4321	0.4055	6.16%
Out of Plane Shear (c)	0.4321	0.4055	6.16%

¥ The type a, b and c for each tip load direction refers to the element type described in figure 4.4

As seen in Table 4.2, the results show that the percentage differences are all within 10%, with the exception of the in-plane shearing (b) which is only slightly higher. In the case of in-plane shearing a greater number of elements can be used in order to minimize the error.

Table 4.3 shows the results for the 8-node brick elements under the same test conditions.

**Table 4.3:** Straight Cantilever Beam for 8 Node Brick Elements.

Tip load direction	Displacement in direction of load		
	Straight Beam Theoretical	8-Node Brick Results	Percentage Difference (%)
Extension (type a)	3.0E-5	2.96E-05	1.47
Extension (type b)	3.0E-5	2.99E-05	0.33
Extension (type c)	3.0E-5	2.99E-05	0.50
In Plane Shear (a)	0.1081	1.00E-02	90.71
In Plane Shear (b)	0.1081	2.90E-03	97.32
In Plane Shear (c)	0.1081	3.16E-02	70.77
Out of Plane Shear (a)	0.4321	1.08E-02	97.50
Out of Plane Shear (b)	0.4321	4.86E-03	98.88
Out of Plane Shear (c)	0.4321	5.70E-03	98.68

As seen in Table 4.3, it can be easily seen that the 8-node brick is capable of producing accurate results for extension tests but not for shear or bending problems. An 8-node brick consists of linear shape functions, as seen in Chapter 2, which are not capable of reproducing bending deformations accurately. Thus, under bending or shear conditions a large number of 8-node bricks would be required in order to properly produce the results.

The figure below shows, how by adding a greater number of 8-node brick elements the deformation of the beam converges to the analytical simulation. With 1,200 elements the solution is only 12.85% from the theoretical results compared to 91% difference obtained with 6 elements along the length and 1 element through the height and thickness of the beam.

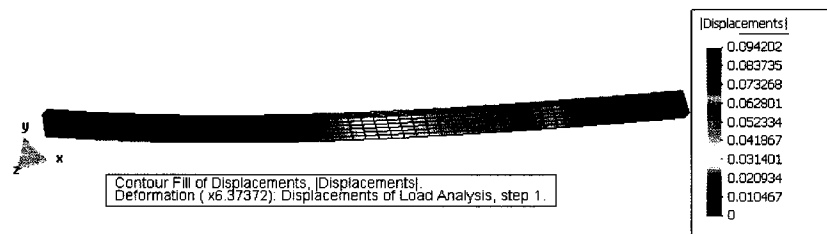


**Figure 4.5:** Shear Simulation with 1,200 8-node brick elements.

### 4.3 Flat sheet test

In the flat sheet test the effect of either uniform pressure or concentrated pressure applied to the thin rectangular plate is calculated. The rectangular plate has dimensions of 2 by 10 by 0.01 meters, as shown in Figure 4.6. The Young's modulus of elasticity is set to  $1.7472 \cdot 10^7$  with a Poisson's ratio of 0.3. McNeal and Harden modeled  $\frac{1}{4}$  of the plate, but it was decided to model the complete plate in order to simplify the boundary conditions. Two types of support are applied at the edge of this test, simply supported and clamped. Figure 4.6 shows the model of the flat rectangular plate with 1 element through the thickness.

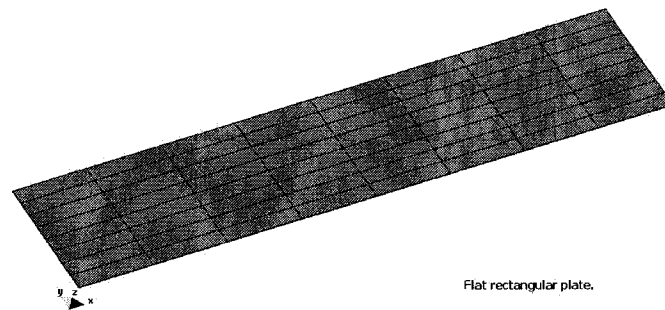


**Figure 4.6:** Flat rectangular plate.

Table 4.4 shows the theoretical displacement at the center of the plate under a uniform pressure or concentrated load. The plate in this problem is set to have either simple or clamped boundary supports.

**Table 4.4:** Displacement at the center of a rectangular plate under uniform pressure/concentrated load for simple and clamped boundary conditions.

Boundary Supports	Aspect Ratio b/a	Displacement at center of plate $\cdot 10^{-6}$	
		Uniform Pressure	Concentrated Force
Simple	1.0	4.062	11.60
Simple	5.0	12.97	16.96
Clamped	1.0	1.26	5.60
Clamped	5.0	2.56	7.23

Table 4.5 shows the results of this test on an a plate modeled with 8-node brick elements.

**Table 4.5:** 8-node brick flat plate under a uniform pressure.

Boundary Supports	Aspect Ratio b/a	Displacement at center of plate 8 Node Brick		
		Uniform Pressure Theoretical	Uniform Pressure	% Difference
Simple 16x16x1	5.0	$12.29 \cdot 10^{-6}$	$2.78 \cdot 10^{-7}$	97.74%
Clamped 8x8x1	5.0	$2.56 \cdot 10^{-6}$	$1.28 \cdot 10^{-8}$	99.50%
Clamped 16x16x1	5.0	$2.56 \cdot 10^{-6}$	$4.98 \cdot 10^{-8}$	98.05%
Clamped 20x20x5	5.0	$2.56 \cdot 10^{-6}$	$7.72 \cdot 10^{-8}$	96.98%

The results presented in Table 4.5 indicate that the 8-node brick, in bending (deformation of a flat plate), do not converge to the theoretical solution. Thus, in order to be able to solve this type of problem it is necessary to either add more 8-node brick elements or to use 20-node brick elements, which can provide better accuracy, as shown in Table 4.6. The small number indicated under each boundary condition indicate the number of elements along the width, length and thickness of the plate respectively. Similar results, as those presented in Table 4.5, have also been shown by McDill [3].

Figure 4.7 shows the deformed state of the complete plate clamped at the edge with a uniform pressure. A clamped condition at the edge is performed by fixing the displacement of every node on the edge of the thin plate to zero in  $x$ ,  $y$  and  $z$ . The simple boundary condition means that no displacement of the edge is allowed in  $z$  but is allowed in  $x$  and  $y$ .

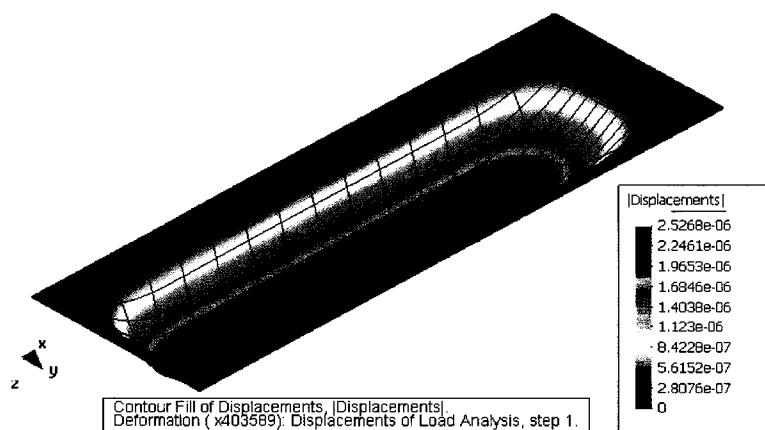


**Figure 4.7:** Clamped plate under a uniform pressure.

Table 4.6 shows the results of a flat sheet test with 20-node brick elements. The results indicate that for an aspect ratio of 5 (aspect ratio defined as the ratio of overall length of the element to the width of the element) the errors of computational results are all within 3%. This indicates that 20-node brick elements are capable of simulating problems where bending is involved. Eight node bricks are also capable, but a lot more elements would be required.

**Table 4.6:** 20-node brick flat plate under a uniform pressure.

Boundary Supports	Aspect Ratio $b/a$	Displacement at center of plate 20 Node Brick		
		Uniform Pressure Theoretical $10^{-6}$	Uniform Pressure $10^{-6}$	% Difference
Note: * 4 by 4, 20 node brick per quarter plate. ** 8 by 8, 20 node brick per quarter plate. *** 4 by 4, 20 node brick per quarter plate.				
Simple*	5.0	12.97	13.30	2.54%
Clamped**	5.0	2.56	2.53	1.17%
Clamped***	5.0	2.56	2.57	-0.39%

Table 4.7 shows the results of an 8-node brick flat plate under a concentrated load. The results also indicate that the use of 8-node brick elements, under a concentrated load condition, require a greater number of 8-node brick elements than presented in Table 4.7 in order to converge to the theoretical result presented by McNeal and Harden.

**Table 4.7: 8-node brick flat plate under a concentrated load.**

Boundary Supports	Aspect Ratio b/a	Displacement at center of plate 8 Node Brick		
		Concentrated Load Theoretical $10^{-6}$	Concentrated Load	% Difference
Clamped 4x4x1	5.0	7.23	$2.0 \cdot 10^{-8}$	99.72%
Clamped 20x20x6	5.0	7.23	$1.17 \cdot 10^{-7}$	98.38%

Similar tests were also conducted on the same flat plate modeled with 20-node brick elements. The results indicate that if only 4 by 4 elements on  $\frac{1}{4}$  of the plate is modeled the obtained displacement under simple and clamped boundary conditions can vary from 38 to 63%. As the number of 20-node brick elements increased the results converged to the theoretical solution and the approximate percentage difference was only 1 to 3%.

**Table 4.8: 20-node brick under a concentrated load.**

Boundary Supports	Aspect Ratio b/a	Displacement at center of plate 20 Node Brick		
		Concentrated Load Theoretical $10^{-6}$	Concentrated Load $10^{-6}$	% Difference
Simple*	5.0	16.96	10.52	37.97%
Clamped**	5.0	7.23	2.71	62.50%
Clamped***	5.0	7.23	7.05	2.50%
Simple <sup>+</sup>	5.0	16.96	16.83	0.77%

\*4 by 4, 20 node brick elements on  $\frac{1}{4}$  plate.

\*\* 4 by 4, 20 node brick elements on  $\frac{1}{4}$  plate.

\*\*\* 30 by 15 by 1, 20 node brick elements on  $\frac{1}{4}$  plate

+ 30 by 15 by 1, 20 node brick elements on  $\frac{1}{4}$  plate

The figure below shows a test where a total of 60 by 30 by 1 element through the thickness is used. The simulation was set under a concentrated load. The results indicate that the value converges to the theoretical solution (2.5% difference).

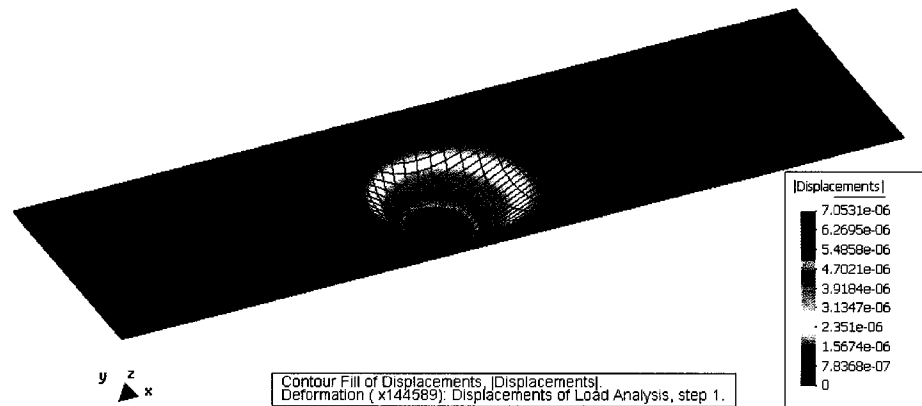


**Figure 4.8:** Concentrated load on a clamped plate (20-node brick).

#### 4.4 Summary of results for elastic problems

It can be concluded that the patch tests both for 8 and 20-node brick elements converges to the theoretical results. The straight cantilever beam tests demonstrated the effectiveness of the 20-node brick elements in extension and in and out-of-plane shear and bending. Eight node brick elements, under the same tests, are only effective in extension problems. Finally the flat plate sheet problem, under a concentrated or uniform load, confirmed the results obtained for a straight cantilever beam under bending conditions. The 8-node brick element is very useful from the point of view of the memory consumption per element, but a larger number of

elements are required to guarantee convergence to the correct solution. It has also been demonstrated that when modeling with 8-node brick elements it is recommended to run the same simulation several times increasing the number of 8-node brick elements to guarantee mesh convergence. Twenty node brick elements would require fewer elements to converge to the correct solution but require greater amounts of memory per element to run the same problem.

#### **4.5 Validation of piezoelectric elements**

In the analysis of piezoelectric elements, a standard set of problems, as presented by McNeal and Harden [1] is not available. Sets of simple problems for which analytical solutions can be determined are used to validate the performance of 8 and 20-node brick piezoelectric elements. The results of these validations are shown in this section of the chapter.

The problems that we have simulated for piezoelectric elements are:

- Piezoelectric extension beam
- Piezoelectric shear beam
- Piezoelectric biomorphic beam
- Piezoelectric sensing element problem.

#### 4.5.1 Piezoelectric extension beam

The piezoelectric extension beam test consists in the extension of a monolithic piezoelectric beam. This condition is obtained in a piezoelectric beam where the polarization vector (poling direction) and the electric field are in the same direction. The analytical equation is a function of the length, the width of the beam, the electric potential difference and the piezoelectric constant  $d_{31}$ . Figure 4.9 shows the laminar design actuation test.

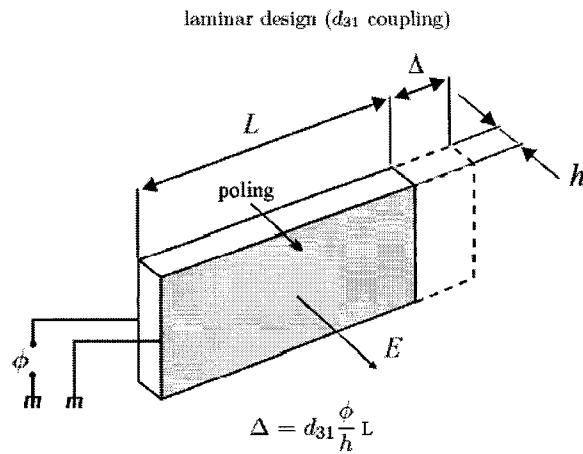


**Figure 4.9:** Laminar actuation [4].

The results of the piezoelectric test are summarized in the table below.

**Table 4.9:** Piezoelectric extension test for 8-node brick elements.

Tip load direction	Displacement		
	Straight Beam Theoretical	8-Node Brick Results	Percentage Difference
Extension (type a)	1.026E-5	1.027E-5	-9.74E-2%
Extension (type b)	1.026E-5	1.026E-5	0.0%
Extension (type c)	1.026E-5	1.026E-5	0.0%

The results of the 8-node brick element show that it is capable of simulating the piezoelectric actuation extension very accurately. It is also seen from Table 4.9 that the geometry of the element seems to have little if any influence on the overall extension result. Similarly results for 20-node brick elements are also shown in Table 4.10.

**Table 4.10:** Piezoelectric extension test 20-Node Brick Elements.

Tip load direction	Displacement due to 1000V electric potential		
	Straight Beam Theoretical	20-Node Brick Results	Percentage Difference
Extension (type a)	1.026E-5	1.027E-5	-9.74E-2%
Extension (type b)	1.026E-5	1.027E-5	-9.74E-2%
Extension (type c)	1.026E-5	1.026E-5	0.0%

#### 4.5.2 Piezoelectric shear beam

The piezoelectric shear beam test, consist in applying the electric field perpendicular to the polarization direction of the material. The resulting actuation causes the beam to shear proportional to the electric potential and the  $d_{15}$  piezoelectric constant. Figure 4.10, shows the deformation a piezoelectric beam under these conditions.

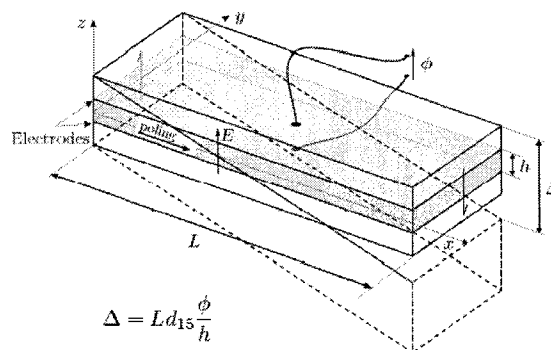


**Figure 4.10:** Shear Actuation Test [4].

Table 4.11 shows the results of the beam in shear. The results are very accurate when compared to the theoretical solution.

**Table 4.11:** Piezoelectric extension test 8-node brick elements

Tip load direction	Displacement due to 1000V		
	Straight Beam Theoretical	8-Node Brick Results	Percentage Difference (%)
Shear (type a)	1.752E-5	1.7523E-5	1.71E-2%
Shear (type b)	1.752E-5	1.7523E-5	1.71E-2%
Shear (type c)	1.752E-5	1.7523E-5	1.71E-2%

Similarly, the 20-node brick piezoelectric element results, under the same shear conditions, are presented in Table 4.12.

**Table 4.12:** Piezoelectric extension test 20-node brick elements

Tip load direction	Displacement due to 1000V		
	Straight Beam Theoretical	20-Node Brick Results	Percentage Difference
Shear (type a)	1.752E-5	1.752E-5	0.0%
Shear (type b)	1.752E-5	1.752E-5	0.0%
Shear (type c)	1.752E-5	1.752E-5	0.0%

As seen by the results produced, the FEM results with 20-node brick matches the experimental results perfectly.

#### 4.5.3 Piezoelectric Bimorphic beam

The bimorphic beam test consists of two layers of piezoelectric material polarized in opposite directions. The bending of the beam is due to the presence of a single electric field through

both piezoelectric layers. The result is the expansion of one of the layers, while the second one contracts producing a bending motion on the beam. The analytical equation describing this type of actuation is proportional to the electric potential difference, the length and the piezoelectric constant  $d_{31}$  as shown in Figure 4.11.

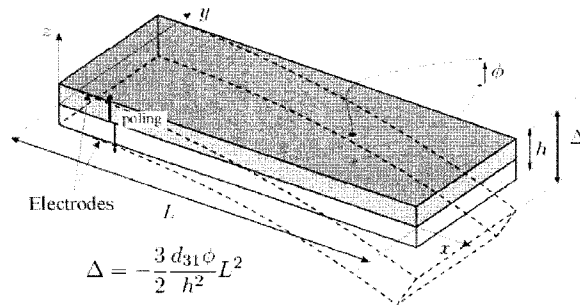


**Figure 4.11:** Bimorphic actuation beam [4].

The results for both 8 and 20-node brick elements, under a bimorphic beam test conditions, are presented in Table 4.13. The beam was placed under an electric potential difference of 1,000V.

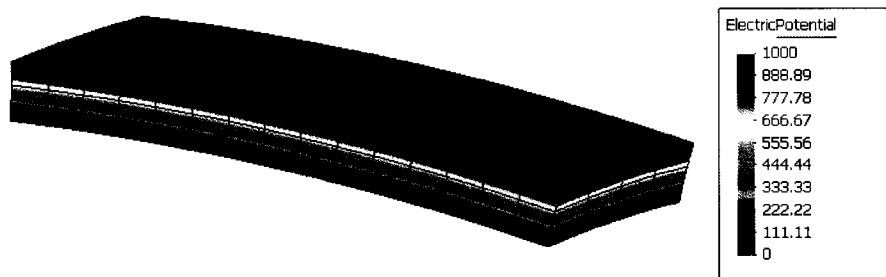


**Figure 4.12:** Bimorphic actuation beam.

As seen in Table 4.13 the results for a bimorphic beam modeled with 20-node brick elements are within 1% of the theoretical results. Similar results with 8-node brick elements are within 14% of the theoretical results. The reason is in the inability of 8-node brick elements to represent bending accurately. In order to avoid this discrepancy in the 8-node brick model a larger number of 8-node brick elements are required.

**Table 4.13:** Piezoelectric bimorphic actuation test

Tip load direction	Displacement due to a 1000V		
	Straight Beam Theoretical	FEM Results	Percentage Difference
Bimorphic Actuation (8-Node brick) <sub>10x15x10</sub>	2.57E-05	2.22E-05	-13.45%
Bimorphic Actuation (20-Node brick) <sub>15x4x10</sub>	2.57E-05	2.54E-05	-0.97%

Analytical equations on the behavior of bimorphic actuators are described in [5]. The next few paragraphs present the analytical equations for bimorphic actuation.

The moment of a cantilevered beam consisting of 2 piezoelectric layers fully attached, as described by Figure 4.12, is presented as:

$$\frac{d^2 w}{dx^2} = -\frac{M + M_{piezo}}{Y \cdot I_{eq}} \quad (4.3)$$

where,

- M is the moment acting on the beam

- $M_{piezo}$  is the moment resulting from the electric field
- $Y$  is the elastic modulus of the material
- $I_{eq}$  is the equivalent moment of inertia
- $w$  is the displacement in  $z$  as a function of the length of beam ( $x$ ).

Assuming that no other moment is applied on the bimorphic cantilevered beam, equation 4.3 can be reduced to:

$$\frac{d^2w}{dx^2} = -\frac{M_{piezo}}{Y \cdot I_{eq}} \quad (4.4)$$

Solving equation 4.4 for  $w$  and assuming that  $\frac{d^2w}{dx^2}$  is equal to zero when  $x$  is equal to zero we obtain:

$$w(x) = -\frac{M_{piezo}}{Y \cdot I_{eq}} x^2 \quad (4.5)$$

Inserting into  $x$  the length of the actuator ( $l$ ), equation 4.5 would provide us with the maximum deflection:

$$w(l) = -\frac{M_{piezo}}{Y \cdot I_{eq}} l^2 \quad (4.6)$$

The piezoelectric moment assuming that the electric field imposed is such that  $E_2 = -E_1$  is:

$$M_{piezo} = -AYd_{31}E_1h \quad (4.7)$$

where,

- A is the cross sectional area of the beam (base · total height of the beam)
- $E_1$  is the electric field applied to top or bottom of the beam from the neutral axis
- h is defined as the height from the neutral axis to the top or bottom of the beam.

The moment of inertia of the beam is assumed to be  $I_{eq} = \frac{2}{3}bh^3$ , thus the maximum deflection as a function of the electric field is defined as:

$$w(l) = \frac{3}{4}d_{31}E_1 \frac{l^2}{h} \quad (4.8)$$

Equation 4.8 is equivalent to that presented in Figure 4.12. In Figure 4.12 the maximum displacement is defined as function of the electric potential. In Figure 4.12 the height is considered the full height of the beam while in equation 4.8 it is only half the height of the beam. Thus, the relation between  $E_1$  and electric potential is  $2\varphi/h$

#### 4.5.4 Piezoelectric sensing problem

The piezoelectric sensing problem consists of applying a deformation field to an element and determining if the electric potential produced corresponds to the analytical solution. The

validation for sensing was only carried out at the element level. In order to validate the sensing problem a strain value in X, Y and Z were applied to a 2 by 2 by 2 element. The applied strain vector was set to:

$$S = \begin{pmatrix} 8.55 \cdot 10^{-8} \\ 8.55 \cdot 10^{-8} \\ -1.87 \cdot 10^{-7} \\ 0 \\ 0 \\ 0 \end{pmatrix} \quad (4.9)$$

The applied strain is shown in Figure 4.13

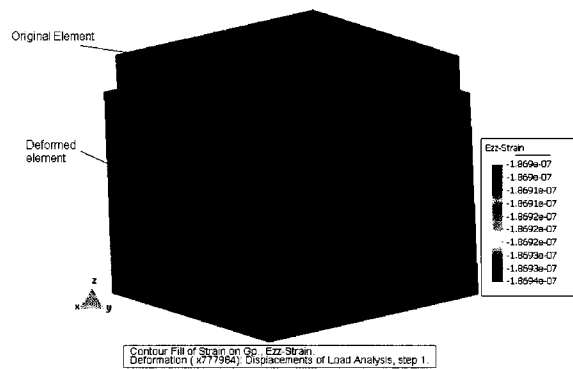


Figure 4.13: Applied strain on the element.

The electric displacement vector ( $D$ ) is set to zero. Thus, from the electro-mechanical constitutive equations (stress voltage form) one can compute the electric field as follows:

$$E = -q\varepsilon + \kappa_s^{-1} D \quad (4.10)$$

Thus, through equation 4.10 we obtain the electric field to be:

$$E = \begin{pmatrix} 0 \\ 0 \\ 528.313 \end{pmatrix} \frac{V}{m} \quad (4.11)$$

The result obtained by our FEM solver is presented in the figure below:

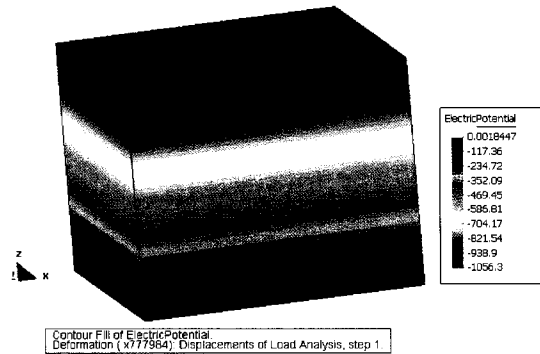


**Figure 4.14:** Electric potential in sensing problem.

The FEM solver outputs electric potential. The electric potential is divided by the length of the element (2) in order to obtain the electric field through the element as: 528.15 V/m vs. a theoretical value of 528.313 V/m thus a percentage difference of 0.03%.

The same simulation was performed on a 20-node brick element and the results matched the theoretical value described above.

#### 4.5.5 Summary of results for piezoelectric problems

As seen from the above results it can be concluded that the 8 and 20-node brick piezoelectric produce the correct results for standard theoretical piezoelectric problems for which the analytical solution is known.

#### 4.6 References for Chapter 4

- [1] Richard H. Macneal and Robert L. Harder, A proposed Standard Set of Problems to test finite element accuracy, The MacNeal Schwendler Corporatinos, 815, Colorado Boulevard, Los Angeles, CA 90041, USA.
- [2] Robert D. Cook, David S. Malkus, Michael E. Plesha, Concepts and Applications of Finite Element Analysis, 3<sup>rd</sup> Edition, Published by John Wiley & Sons 1989.
- [3] J.M.J. McDill, K.H. Runnemalm, A.S. Oddy, An 8- to 16-Node Solid Graded Shell Element for Far-Field Applications in Adaptive 3-D Thermal-Mechanical FEA, Mathematical Modelling and Scientific Computing Vol 13., No. 3, pp. 177-190, Principia Scientia 2001.
- [4] Vincent Piefort, Finite Element Modeling of Piezoelectric Active Structures, PhD. Thesis, Université Libre de Bruxelles, 2000-2001.
- [5] Roman Solecki, R. Jay Conant, Advanced Mechanics of Materials, New York, Oxford University Press, 2003.

FINITE ELEMENT ANALYSIS OF COMPOSITES WITH PIEZOELECTRIC  
FIBERS

**5.0 Introduction**

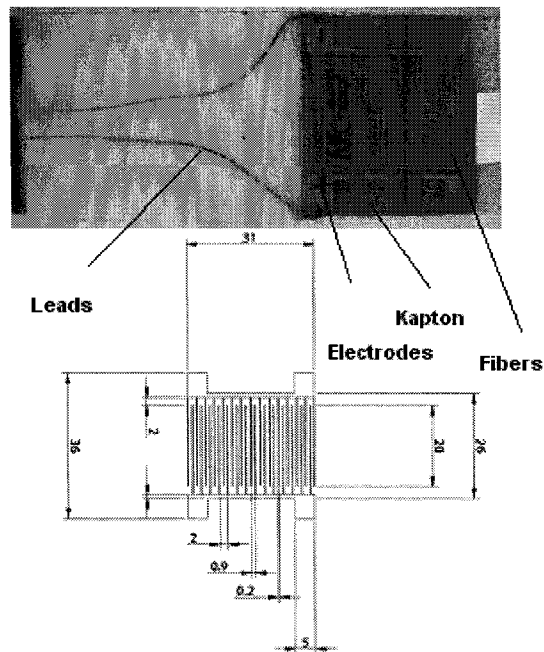
In this chapter the results obtained using finite element methods for the analysis of the behavior of structures with piezoelectric and elastic components will be presented. Many possible structures, that combine elastic and piezoelectric properties, can be analyzed using FEM. We have selected the study of piezoelectric fibers, sandwiched in-between an epoxy/Kapton layers forming an active composite. This type of composite is known as an Actuated Fiber Composites (AFC). AFC are being developed by several research organizations such as NASA-Langley Research Center, the Defense Advanced Research Projects Agency (DARPA) and the Swiss Federal Laboratories for Material Testing and Research (EMPA), for sensing and actuation applications.

The research presented in this thesis was produced in collaboration with EMPA and a research group of Prof. F. Nitzsche from Carleton University. The primary goal of the author of this thesis was to develop a finite element solver, which could be used for the analysis and design of AFC and their applications. The experimental results presented in this thesis were obtained

by EMPA. The main goal of the collaborative project is to create flexible sensors and actuators that can adapt to different surface contours for use in such applications as “Smart Blades” [1]. Such flexibility is impossible to achieve when using bulk piezoelectric ceramics. In the development of flexible piezoelectric sensors and actuators, design tools capable of predicting the behavior of piezoelectric structures are required. EMPA has created AFC specimens and experimentally tested them under different conditions. The AFC structures and actuation methods were presented and studied in [2-5].

The AFC systems manufactured by EMPA have a thickness of 0.26mm, a length of 31mm, and a width of 36mm. The AFC specimens have an active area of 31mm in length by 26mm in width. An active fiber section is the area of the AFC in-between two consecutive electrodes, thus it is the area of the AFC that contributes to the actuation. The AFC have a total of 76 PZT fibers in the active area of the AFC and are made with the following materials and components, as seen in Figure 5.1:

- Epoxy matrix
- PZT fibers
- Copper electrodes
- Kapton layers
- Glass Fiber Reinforced Plastic (GFRP).



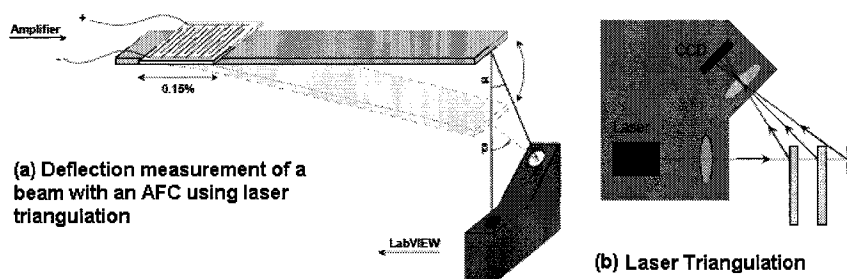
**Figure 5.1:** AFC Geometry, all dimensions in mm [6,7].

Figure 5.1 shows the electrode pattern used in EMPA's AFC. This type of electrode pattern allows for the poling of the fibers in-situ. AFC systems, as those manufactured by EMPA, have been modeled and studied using FEM in this work. This type of AFC system, will be called the unconstrained AFC system.

An AFC where the AFC layer is constrained symmetrically by layers of elastic material (Glass Fiber Reinforced Polymer GFRP) will be called in this thesis, the constrained AFC model. The constrained AFC was also manufactured by EMPA. The layer of GFRP that covered the AFC had a thickness of  $260\mu\text{m}$ , a width of  $2150\mu\text{m}$ , and a length of  $4600\mu\text{m}$ . This specimen was clamped at one end.

All experimental work was performed by EMPA and we did not make any contribution to the experimental results. Thus, only a very brief description of the experiment is presented. The AFC systems were manufactured and tested for actuation and sensing performance. The actuation experiments consisted of clamping the manufactured AFC at one end, while a voltage was applied at the IDE in order to induce an extension deformation of the AFC. The strain was measured indirectly due to the high actuation voltages induced in the AFC. Indirect measurement of the deformation were mostly performed in order to avoid potentially damaging the amplifiers that one would typically use to perform the measurements with strain gauges. The high actuation voltages on the IDE can also affect the strain gauges. EMPA also performed direct measurements using strain gauges.

A laser was used to measure the resulting extension of the AFC specimens. The measurement is obtained using a non-contact laser triangulation sensor (LTS). The measurement was done using a focused laser beam (wavelength 670 nm), which is reflected from the AFC and re-focused and sensed by a charge-coupled device (CCD). The CCD is a NCDT 2000 model from Micro-optronic. This device has a measurement range of  $\pm 10\text{mm}$  with a resolution of  $1\mu\text{m}$ . The figure below shows a simplified schematic of the laser triangulation technique [5]:



**Figure 5.2:** (a) deflection measurement of AFC on beam, (b) laser triangulation schematic [5]

A laser beam is used to measure the overall displacement produced by the AFC under free strain and constrained conditions. Figure 5.2 shows the AFC with a laser target. The overall displacement is measured from which the strain in  $\epsilon_{xx}$  is calculated.

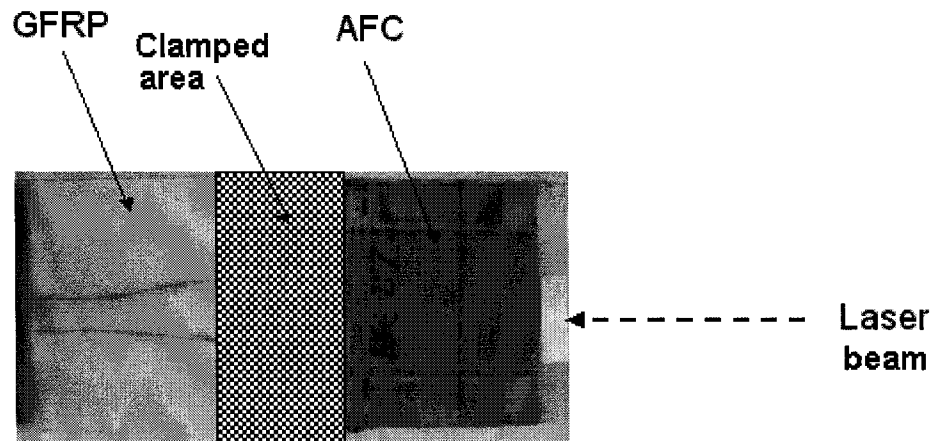


Figure 5.3: Clamped AFC setup [6].

Figure 5.3 shows the clamped AFC setup, where the laser beam measures the distance that the AFC extends out. Once the actuation distance of the AFC is measured and knowing the original (non-actuated) length of the AFC, the strain is computed. The clamped area of the AFC consists of fixing, by compression, the back end of the AFC to avoid any displacement of this section.

The sensing tests in which a mechanical strain was applied to the specimens and the electric response was measured were performed by EMPA [8] and also additional data were obtained from literature [9]. In [8] the specimens were subjected to a static strain and the changes in sensing efficiency were measured at different levels of applied static strain by super-imposing small amplitudes oscillating strain. In [9] the fatigue testing was performed (according to

ASTM Standards) with the purpose to determine the degradation of sensing actuation performance of AFC resulting from damaged produced by fatigue.

This thesis presents results of the FEM models of AFC systems as those manufactured by EMPA. The experimental results provided by EMPA are used for validation of our FEM code and analysis of other computational models.

This chapter is divided into three sections. The first section covers an introduction and brief description of the experimental work performed by EMPA. The second section is a description of the FEM models and results of computer simulations. In particular, the results of sensing and actuation performance simulation for continuous fiber AFC are shown and compared to analytical solutions and experimental data. The results of analysis for single layer AFC and bi-layer AFC-GFRP system are shown. The second section also presents results of the study of the effects that non-continuous fibers have on AFC performance both in sensing, extension actuation and shear actuation. Finally, the third section of the chapter covers the homogenization technique that would be used to develop an element that behaves like an AFC. The homogenization technique is briefly described as possible future work in order to improve the capabilities of our solver.

## **5.1 FEM models of AFC systems**

A large number of finite elements are required to model the AFC, as shown in Figure 5.1. Due to the memory limitation of our solver it was decided to model a section of the AFC and

compare the strain values produced by the FEM solver to the experimental strain values obtained by EMPA. The AFC was modeled using the same design parameters as the AFC manufactured by EMPA. Almost all the calculations were performed using 8-node brick elements with tri-linear shape functions [10-12]. For those simulations where the deformation involved bending of the structure; 20-node brick elements were used. The FEM models will be individually described next.

### **5.1.1 Unconstrained AFC with continuous fibers**

In our FEM simulations we used a model of a section of an AFC with a length of 4600  $\mu\text{m}$ , a width of 1200  $\mu\text{m}$ , and a thickness of 260  $\mu\text{m}$ . The PZT-5A fibers with 250 $\mu\text{m}$  diameters were spaced at 300 $\mu\text{m}$ , center to center. It consisted of four piezoelectric fibers, an epoxy matrix, and copper interdigitized electrodes (IDE) that were covered by a top and bottom layer of epoxy. Figure 5.4-a shows a view of the FEM model of an AFC specimen with the epoxy matrix. Figure 5.4-b demonstrates the same AFC with the epoxy matrix made transparent to show the fibers and the copper electrodes. The IDE manufactured by EMPA are made out of silver. As it will be shown later in this chapter, the difference in performance in modeling the AFC with copper versus silver is minimal since the experimental and FEM results match very closely. The AFC was cantilevered at one end.

The fibers had a varying polarization along their length. The fibers between electrodes E1 and E2, shown in Figure 5.4-b, have polarization along the positive x direction while the fibers between electrodes E2 and E3 have polarization along the negative x direction. This permits

the AFC to extend or contract since the direction of the electric field also changes from one electrode pair to another. The applied electric potentials cause the regions between the electrodes to extend because the direction of fiber polarization between each pair of electrodes coincides with the direction of the electric field between them.

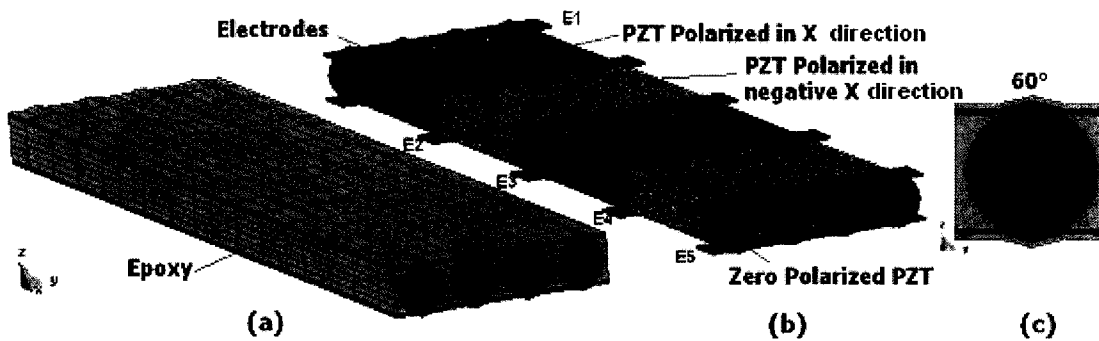


**Figure 5.4:** (a) AFC with epoxy matrix, (b) Inner components of AFC, (c) Cross-sectional view of AFC at the electrodes with a  $60^\circ$  contact angle between the electrode and the PZT fiber.

The four copper electrodes are spaced at  $900 \mu\text{m}$  apart and are  $200 \mu\text{m}$  wide and  $10 \mu\text{m}$  thick. The electrodes in Figure 5.4-b are labeled as E1, E2, E3 and E4. The electric potential for E2 and E4 are set to zero, while E1 and E3 are set to the electric potential of 900, 1350, and 1800 Volts for each simulation run. The copper electrodes make a direct contact with the fibers through an angle of  $60^\circ$ , as shown in Figure 5.4-c. The fiber under the electrodes was modeled to have zero polarization.

### 5.1.2 AFC symmetrically constrained by GFRP layers (Constrained AFC) with continuous fibers

A model, where the AFC layer is constrained symmetrically by layers of elastic material; Glass Fiber Reinforced Polymer (GFRP) was also analyzed. The upper layer of the AFC in the FEM model was changed from Epoxy to a Kapton layer as shown in Figure 5.5. In our FEM simulation of this AFC, the model was also clamped at one end and the electric potentials were set, as described in Figure 5.5.

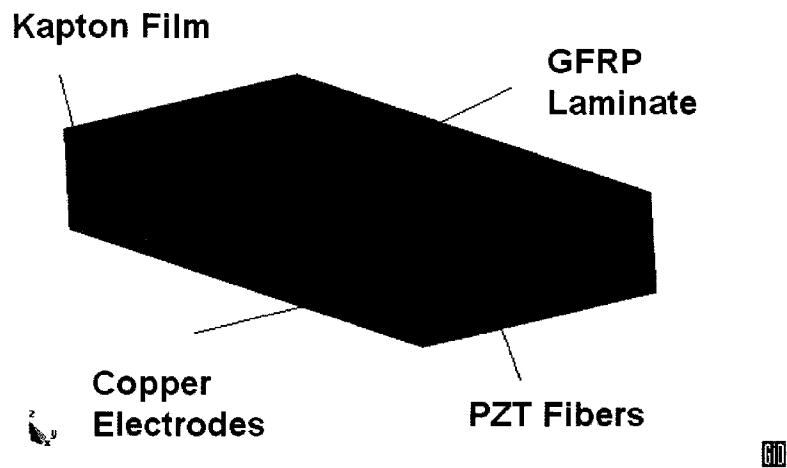


Figure 5.5: GFRP Constrained AFC.

Figure 5.6 shows a cross sectional view of the constrained AFC model.

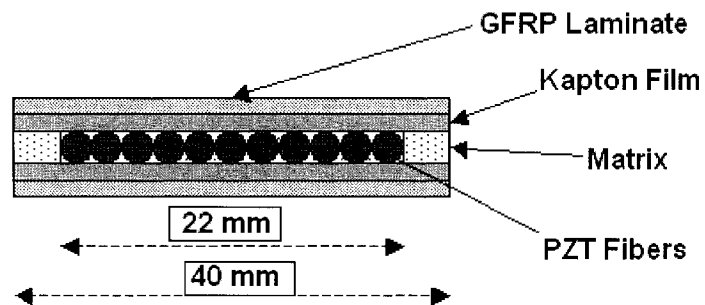
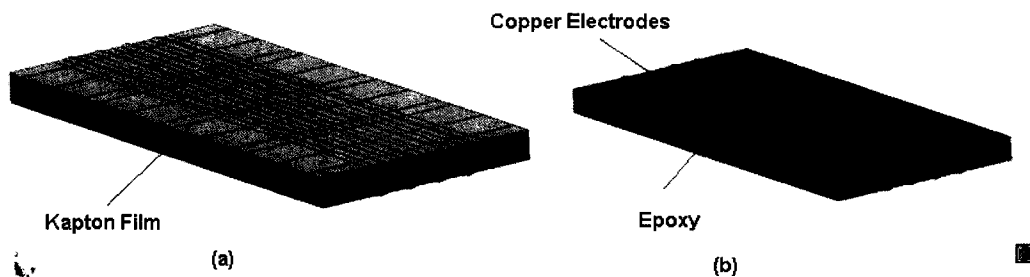


Figure 5.6: Constrained AFC [7].

In Figure 5.7-a, the GFRP laminate is hidden to expose the Kapton film. Simulations with and without the Kapton were carried out, which demonstrate (by comparison of the FEM and experimental results) the little effect that the Kapton layer has on the overall actuation performance of the AFC. Figure 5.7-b, shows the same model with a transparent Kapton layer, in order to visualize the copper electrodes.



**Figure 5.7:** (a) AFC with transparent GFRP layers, (b) Transparent Kapton and GFRP layer of the constrained AFC.

### 5.1.3 Unconstrained AFC with broken fibers (actuation tests)

Several models to study the effect of non-continuous fibers were also created. Figure 5.8 shows models with broken fibers. The non-continuous fiber model consists of small  $30\ \mu\text{m}$  gaps introduced in the AFC model. The number of gaps varied from one to five to ten and to twenty. The gaps were introduced in the space between the electrodes, at approximately  $450\ \mu\text{m}$  from the edge of an electrode (the electrode spacing is  $900\ \mu\text{m}$ ). The gaps were filled with epoxy matrix. The actuation voltage on the IDE was set to  $900\text{V}$  in each case. The spacing between fibers varied from  $300\ \mu\text{m}$  to  $270\ \mu\text{m}$  in order to maintain a constant volume fraction of approximately  $60\%$ . Simulation runs were conducted for non-continuous fibers under an

applied voltage that caused extension and shear of the AFC. In all cases, the 8-node brick piezoelectric elements were used.

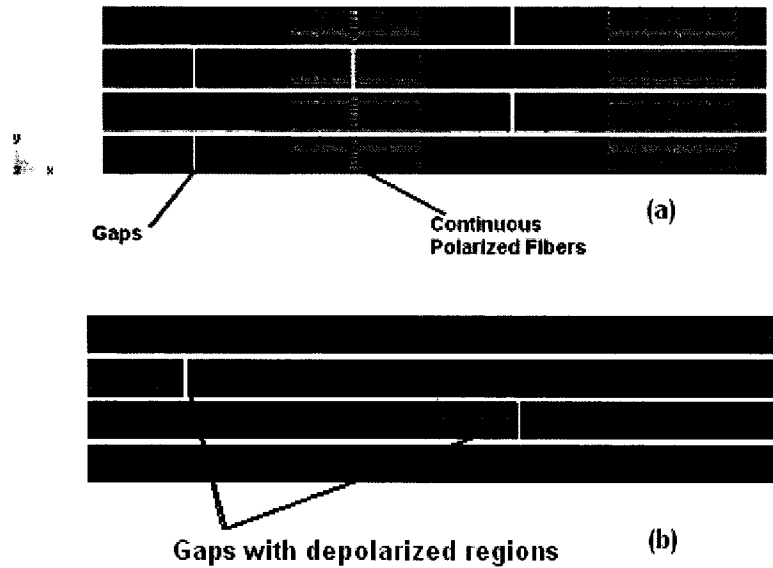


**Figure 5.8:** Non-continuous fiber model.

The study on non-continuous fibers also analyzed the effect of depolarization at the gap interface due to the presence of the gap. The presence of a gap in the fiber has been studied in [2,3]. In [3] the domain structure in the broken fiber was simulated using a phase field model developed in [17] for domain structures in ferroelectric materials. The results of these studies [2,3] indicate that the presence of a gap in the fiber can create depolarized regions that can be very large compared to the size of the gap. In this thesis we have assumed that the depolarized region approximates one fiber diameter. Results of the effect of fully polarized and depolarized fibers with gaps in actuation and sensing conditions are presented in the results section of this thesis.

#### **5.1.4 Unconstrained AFC with broken fibers (sensing tests)**

A model to study the effect of continuous and non-continuous fibers was also analyzed for sensing applications. The FEM model of the AFC was 2100  $\mu\text{m}$  by 1200  $\mu\text{m}$  by 243  $\mu\text{m}$  in size. Two scenarios for sensing were considered. In the first setup, the fibers of the AFC were polarized along the length of the fiber while in the second setup the fibers of the AFC were polarized along the diameter of the fiber. The AFC was cantilevered at one end while the second end was set to an extension of 0.9  $\mu\text{m}$ . In the case where the AFC fibers were polarized along the length of the fiber the electric potential difference was measured along the fiber length. The AFC that had the fibers polarized along the diameter of the fiber, the electric potential difference was measured along the diameter of the fiber.

The model of an unconstrained AFC with broken fibers was also used to analyze the performance of an AFC with broken fibers under an actuation voltage that causes the AFC to shear.

#### **5.1.5 Bi-layer AFC-GFRP system**

Figure 5.9 shows a model of a bi-layer structure consisting of an AFC and GFRP layer. The AFC was set to have electric potentials that caused the AFC to extend. The extension of the AFC layer on the GFRP causes the GFRP/AFC structure to bend. The AFC was modeled

with a length of 4600  $\mu\text{m}$ , a width of 1200  $\mu\text{m}$  and a thickness of 260  $\mu\text{m}$ . The GFRP beam was modeled with the same dimensions as the AFC (260  $\mu\text{m}$ ). The Kapton film on the AFC was modeled with a 10  $\mu\text{m}$  thickness. In this model, 20-node brick elements were used. This is the only model where 20-node brick elements are used because they are more suitable for the simulation of bending deformation that happens when the AFC layer extends under the effect of an applied voltage.

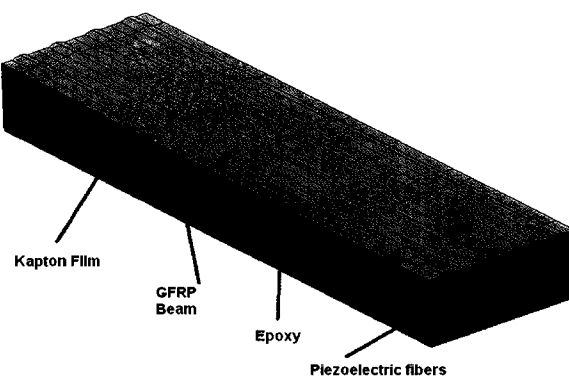


**Figure 5.9:** AFC on GFRP beam.

### 5.1.6 End Constrained AFC

The final model that was analyzed was of an AFC contracting and pulling on a GFRP section, as shown in Figure 5.10. In this model both ends were fully fixed as to cause for the GFRP part of the structure to extend while the AFC contracted due to an applied voltage. The simulations were conducted with continuous and non-continuous fibers.

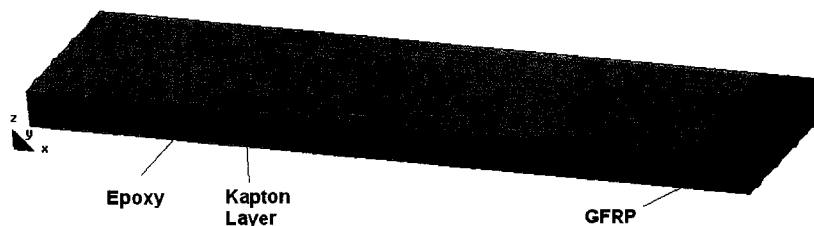


**Figure 5.10:** AFC pulling on a GFRP section of a beam due to an applied voltage.

The material properties for each material used for all of the above models are described in Tables 5.1, 5.2 and 5.3.

**Table 5.1:** Material properties for PZT-5A and epoxy [6].

PZT-5A Properties		Epoxy Properties	
PERMITTIVITY (F/m) p11	8.137E-9	PERMITTIVITY (F/m) p11	3.542E-11
PERMITTIVITY (F/m) p22	8.137E-9	PERMITTIVITY (F/m) p22	3.542E-11
PERMITTIVITY (F/m) p33	7.319E-9	PERMITTIVITY (F/m) p33	3.542E-11
PIEZOELEC COUPLING (sAm <sup>-2</sup> ) d31	-0.395	PIEZOELEC COUPLING (sAm <sup>-2</sup> ) d31	0.0
PIEZOELEC COUPLING (sAm <sup>-2</sup> )_d32	-0.395	PIEZOELEC COUPLING (sAm <sup>-2</sup> )_d32	0.0
PIEZOELEC_COUPLING_(sAm <sup>-2</sup> )_d33	23.101	PIEZOELEC_COUPLING_(sAm <sup>-2</sup> )_d33	0.0
PIEZOELEC COUPLING (sAm <sup>-2</sup> ) d24	12.295	PIEZOELEC COUPLING (sAm <sup>-2</sup> ) d24	0.0
PIEZOELEC COUPLING (sAm <sup>-2</sup> ) d15	12.295	PIEZOELEC COUPLING (sAm <sup>-2</sup> ) d15	0.0
STIFFNESS Q11 (N/m <sup>2</sup> )	1.203E11	STIFFNESS Q11 (N/m <sup>2</sup> )	6.52E9
STIFFNESS Q12 (N/m <sup>2</sup> )	7.518E10	STIFFNESS Q12 (N/m <sup>2</sup> )	3.98E9
STIFFNESS Q13 (N/m <sup>2</sup> )	7.509E10	STIFFNESS Q13 (N/m <sup>2</sup> )	3.98E9
STIFFNESS Q21 (N/m <sup>2</sup> )	7.518E10	STIFFNESS Q21 (N/m <sup>2</sup> )	3.98E9
STIFFNESS Q22 (N/m <sup>2</sup> )	1.203E11	STIFFNESS Q22 (N/m <sup>2</sup> )	6.52E9
STIFFNESS Q23 (N/m <sup>2</sup> )	7.509E10	STIFFNESS Q23 (N/m <sup>2</sup> )	3.98E9
STIFFNESS Q31 (N/m <sup>2</sup> )	7.509E10	STIFFNESS Q31 (N/m <sup>2</sup> )	3.98E9
STIFFNESS Q32 (N/m <sup>2</sup> )	7.509E10	STIFFNESS Q32 (N/m <sup>2</sup> )	3.98E9
STIFFNESS Q33 (N/m <sup>2</sup> )	1.109E11	STIFFNESS Q33 (N/m <sup>2</sup> )	6.52E9
STIFFNESS Q44 (N/m <sup>2</sup> )	2.105E10	STIFFNESS Q44 (N/m <sup>2</sup> )	1.27E9
STIFFNESS Q55 (N/m <sup>2</sup> )	2.105E10	STIFFNESS Q55 (N/m <sup>2</sup> )	1.27E9
STIFFNESS Q66 (N/m <sup>2</sup> )	2.257E10	STIFFNESS Q66 (N/m <sup>2</sup> )	1.27E9
POLARIZATION(X=1,Y=2,Z=3)	1 or 2 or 3	POLARIZATION(X=1,Y=2,Z=3)	1 or 2 or 3

Negatively polarized fiber sections have the same value of piezoelectric constant as the PZT-5A presented in Table 5.1, with the only difference being that negative one multiplies the values for piezoelectric constants. In the case of the zero polarized PZT-5A, the piezoelectric coupling values are set to zero.

Table 5.2 contains the material properties used for the Kapton film and for the inter-digitized copper electrodes.

**Table 5.2:** Material properties for copper and negative polarized PZT-5A [13].

Kapton Film		Copper	
PERMITTIVITY (F/m) p11	3.01E-11	PERMITTIVITY (F/m) p11	1.603E-10
PERMITTIVITY (F/m) p22	3.01E-11	PERMITTIVITY (F/m) p22	1.603E-10
PERMITTIVITY (F/m) p33	3.01E-11	PERMITTIVITY (F/m) p33	1.603E-10
PIEZOELEC COUPLING (sAm <sup>-2</sup> ) d31	0	PIEZOELEC COUPLING (sAm <sup>-2</sup> ) d31	0
PIEZOELEC COUPLING (sAm <sup>-2</sup> ) d32	0	PIEZOELEC COUPLING (sAm <sup>-2</sup> ) d32	0
PIEZOELEC_COUPLING_(sAm <sup>-2</sup> )_d33	0	PIEZOELEC_COUPLING_(sAm <sup>-2</sup> )_d33	0
PIEZOELEC COUPLING (sAm <sup>-2</sup> ) d24	0	PIEZOELEC COUPLING (sAm <sup>-2</sup> ) d24	0
PIEZOELEC COUPLING (sAm <sup>-2</sup> ) d15	0	PIEZOELEC COUPLING (sAm <sup>-2</sup> ) d15	0
STIFFNESS Q11 (N/m <sup>2</sup> )	3.848E9	STIFFNESS Q11 (N/m <sup>2</sup> )	1.801E11
STIFFNESS Q12 (N/m <sup>2</sup> )	1.982E9	STIFFNESS Q12 (N/m <sup>2</sup> )	9.277E10
STIFFNESS Q13 (N/m <sup>2</sup> )	1.982E9	STIFFNESS Q13 (N/m <sup>2</sup> )	9.277E10
STIFFNESS Q21 (N/m <sup>2</sup> )	1.982E9	STIFFNESS Q21 (N/m <sup>2</sup> )	9.277E10
STIFFNESS Q22 (N/m <sup>2</sup> )	3.848E9	STIFFNESS Q22 (N/m <sup>2</sup> )	1.801E11
STIFFNESS Q23 (N/m <sup>2</sup> )	1.982E9	STIFFNESS Q23 (N/m <sup>2</sup> )	9.277E10
STIFFNESS Q31 (N/m <sup>2</sup> )	1.982E9	STIFFNESS Q31 (N/m <sup>2</sup> )	9.277E10
STIFFNESS Q32 (N/m <sup>2</sup> )	1.982E9	STIFFNESS Q32 (N/m <sup>2</sup> )	9.277E10
STIFFNESS Q33 (N/m <sup>2</sup> )	3.848E9	STIFFNESS Q33 (N/m <sup>2</sup> )	1.801E11
STIFFNESS Q44 (N/m <sup>2</sup> )	9.328E8	STIFFNESS Q44 (N/m <sup>2</sup> )	4.366E10
STIFFNESS Q55 (N/m <sup>2</sup> )	9.328E8	STIFFNESS Q55 (N/m <sup>2</sup> )	4.366E10
STIFFNESS Q66 (N/m <sup>2</sup> )	9.328E8	STIFFNESS Q66 (N/m <sup>2</sup> )	4.366E10
POLARIZATION(X=1,Y=2,Z=3)	1 or 2 or 3	POLARIZATION(X=1,Y=2,Z=3)	1 or 2 or 3

Table 5.3 shows the material properties used for modeling the GFRP beam.

**Table 5.3:** Material properties for GFRP [6].

GFRP	
PERMITTIVITY (F/m) p11	6.375E-11
PERMITTIVITY (F/m) p22	6.375E-11
PERMITTIVITY (F/m) p33	6.375E-11
All PIEZOELEC COUPLING (sAm <sup>-2</sup> )	0.0
STIFFNESS Q11 (N/m <sup>2</sup> )	4.109E10
STIFFNESS Q12 (N/m <sup>2</sup> )	2.212E10
STIFFNESS Q13 (N/m <sup>2</sup> )	2.212E10
STIFFNESS Q21 (N/m <sup>2</sup> )	2.212E10
STIFFNESS Q22 (N/m <sup>2</sup> )	4.109E10
STIFFNESS Q23 (N/m <sup>2</sup> )	2.212E10

**Table 5.3-Continuation:** Material properties for GFRP [6].

STIFFNESS Q31 (N/m <sup>2</sup> )	2.212E10
STIFFNESS Q32 (N/m <sup>2</sup> )	2.212E10
STIFFNESS Q33 (N/m <sup>2</sup> )	4.109E10
STIFFNESS Q44 (N/m <sup>2</sup> )	9.481E9
STIFFNESS Q55 (N/m <sup>2</sup> )	9.481E9
STIFFNESS Q66 (N/m <sup>2</sup> )	9.481E9
POLARIZATION(X=1,Y=2,Z=3)	1 or 2 or 3

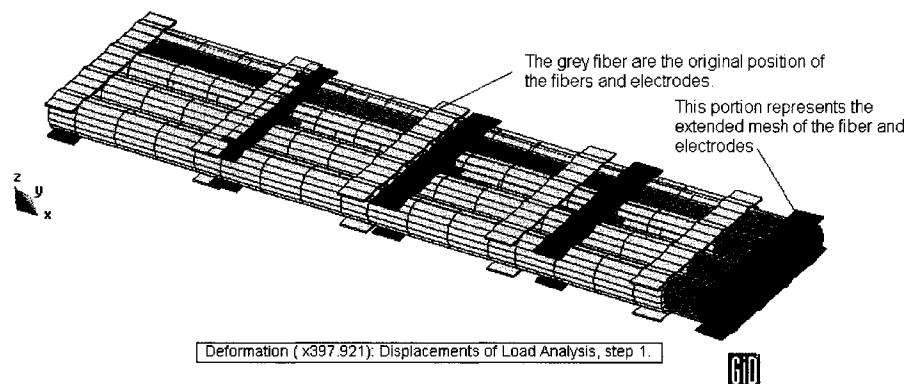
## 5.2 Results

This section summarizes the results obtained from all simulations of AFC systems. The section is divided into the following parts:

- Unconstrained AFC with continuous fibers
- AFC symmetrically constrained by GFRP layers (Constrained AFC) with continuous fibers
- Unconstrained AFC with broken fibers (actuation tests)
- Unconstrained AFC with broken fibers (sensing tests)
- Bi-layer AFC-GFRP System
- End Constrained AFC
- Analytical model for the deformation of bi-layer system.

### 5.2.1 Unconstrained AFC with continuous fibers

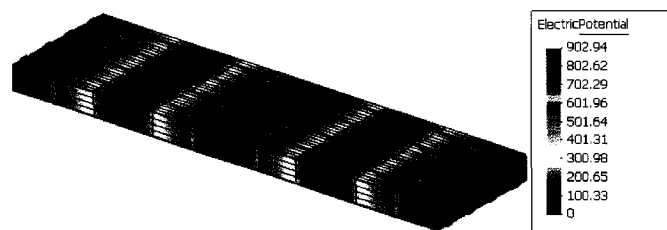
The figure below shows the original and extended AFC, where the epoxy has been hidden in order to see the deformation of the fibers.



**Figure 5.11:** Extended fiber and electrode (deformation not to scale).

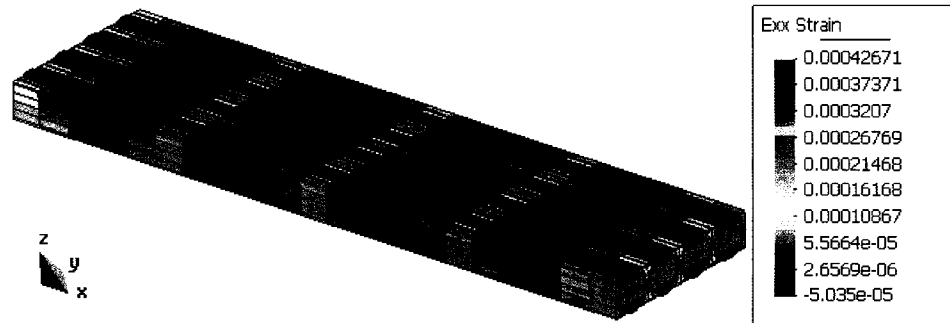
The finite element simulation of the AFC showed an extension of  $1.37 \mu\text{m}$  obtained in the model with 4 active sections. An active section is the space between two consecutive electrodes along the fiber length. The actual EMPA AFC has 28 active sections, which according to the FEM model, would produce an extension of  $9.59 \mu\text{m}$ .

Figure 5.12 shows the distribution of the electric potential in an unconstrained AFC with 900 volts applied to the IDE.



**Figure 5.12:** Electric potential of unconstrained AFC.

Figure 5.13 shows the longitudinal strain,  $\epsilon_{xx}$  in the AFC calculated by the FEM solver.



**Figure 5.13:** Computed strain field on unconstrained AFC.

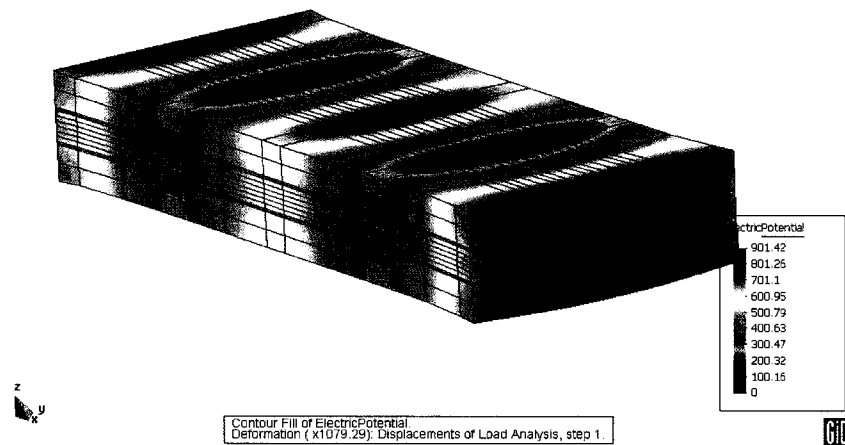
Table 5.4 shows the average strain computed by the FEM solver and the experimentally measured values. The difference between the strain values computed by the FEM solver and the measured strains are within 5% at higher voltages and better than 5% at lower voltages. At higher voltages the non-linearity in the material started affecting the strain and the overall actuation of the fibers. Although the FEM solver is a linear solver, simulations were run at different voltages in order to compare the experimental results. Thus, at higher voltages the percentage difference between the FEM and experimental strain values increased. It is also important to note that the models in this simulation replaced the Kapton layer with an epoxy layer and the results between experimental and FEM are still very close. This indicates that the Kapton layer does not significantly affect the performance of the AFC.

**Table 5.4:**  $\epsilon_{xx}$  strain values computed by the FEM solver and  $\epsilon_{xx}$  strain values measured at EMPA for an AFC under free strain conditions.

Applied Voltage (Volts)	$E_{xx}$ strain produced by FEM Solver	$E_{xx}$ strain measured EMPA Experimental	Difference, %
900	0.0004088	0.00041	0.29%
1350	0.0006135	0.00064	4.14%
1800	0.0008170	0.00086	5.00%

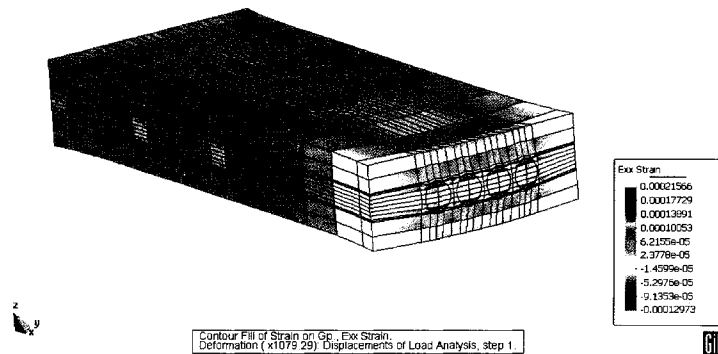
### 5.2.2 AFC symmetrically constrained by GFRP layers (Constrained AFC) with continuous fibers

Figure 5.14 shows the distribution of electric potentials in GFRP and epoxy layers obtained when actuation voltage was applied to the IDE.



**Figure 5.14:** Electric potential through the constrained AFC.

The simulations for constrained AFC were performed using 900, 1800, and 2250 Volts actuation potentials. The experimental strain  $\epsilon_{xx}$  values are computed from the measured displacement. The strain values  $\epsilon_{xx}$  are shown in the Figure 5.15. The average value of  $\epsilon_{xx}$  on the surface of the GFRP is approximately 0.00010 at 900 Volts.



**Figure 5.15:** Strain,  $\epsilon_{xx}$  in the constrained AFC at 900Volts.

The table below shows a summary of the experimental and FEM results.

**Table 5.5:** Summary of strain for EMPA's constrained AFC.

Voltage Applied (Volts)	Strain $\epsilon_{xx}$ Experimental	Strain $\epsilon_{xx}$ FEM.	% Difference
900	0.00010	0.00010	0.00%
1800	0.00019	0.00020	5.26%
2250	0.00023	0.00022	4.54%

### 5.2.3 Unconstrained AFC with broken fibers (actuation tests)

The introduction of gaps in fibers in the AFC produces a strong effect on the distribution of electric field. This effect causes a change in the performance of the AFC. The figure below shows the electric potential in AFC with continuous fibers (Fig. 5.16-a) and with five 30  $\mu\text{m}$  gaps (Fig. 5.16-b). As seen in Figure 5.16-b, the fibers with gaps create a large electric potential difference in the proximity of the gap, creating a capacitor effect in the gap. The region of

polarized fiber between the electrode and the gap has small electric potential difference, thus eliminating the contribution in extension or contraction for that active area of the AFC.

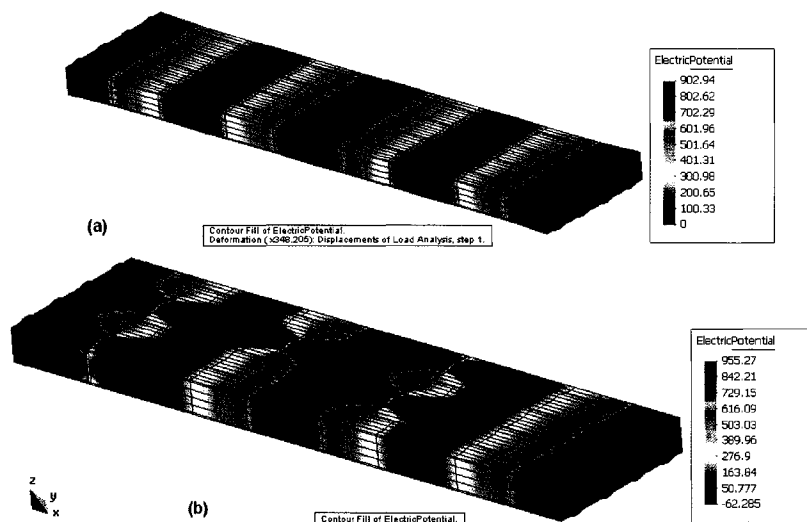


**Figure 5.16:** (a) Electric potential on AFC with continuous fibers. (b) Shows the electric potential on an AFC with 5 random 30  $\mu\text{m}$  gaps along the fiber length.

Several simulations were carried out in order to determine the effect of non-continuous fibers on the extension actuation of the AFC. Figure 5.17 shows that the application of an electric field on an unconstrained AFC with discontinuous fibers demonstrates that the loss of displacement for every non-continuous fiber is significant and almost linear.

The introduction of gaps in the fibers of the FEM model presented two possible cases. The first case was to look at the effect in actuation and sensing performance of the AFC due to the presence of a gap in the fibers of the AFC, neglecting the depolarization region created by the gap. The second case consisted in simulating the depolarization region at the interfaces of each gap.

The additional effect of a depolarized section of the fiber at the gap interface has little or no effect on the actuation performance of the AFC. This is assuming that the depolarized region at the gap interface is approximately one fiber diameter.

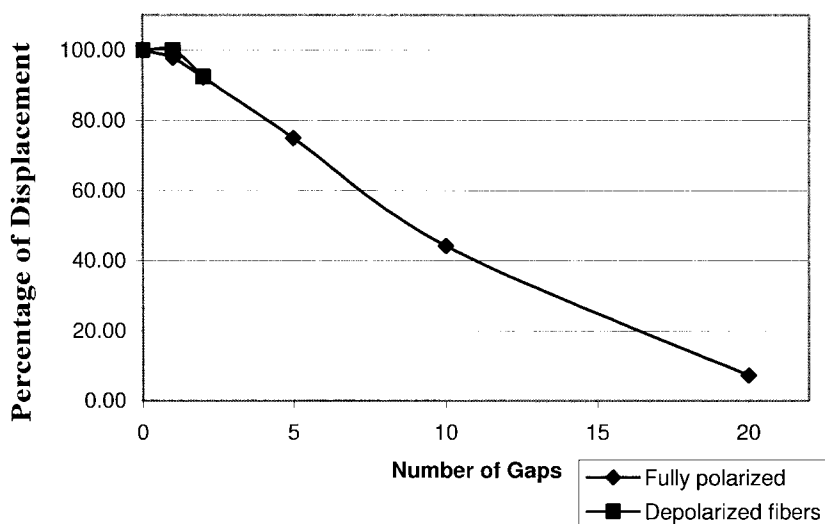


**Figure 5.17:** The simulated actuation displacement, obtained in an AFC with discontinuous fibers shown as a percentage of displacement obtained in an AFC with continuous fibers, vs. number of gaps.

#### 5.2.4 Unconstrained AFC with broken fibers (sensing tests)

A similar set of simulations for sensing applications of the AFC was also conducted. Figure 5.18 shows the effect of non-continuous fibers on the sensing performance of AFC. The AFC was cantilevered at one end while a displacement of  $0.9 \mu\text{m}$  was applied to the opposite end. The voltage across the fiber diameter was obtained from the simulation. The fibers for this simulation were poled through the diameter of the fiber. Figure 5.18 indicates that for a small number of discontinuities (long fiber limit), the expected effect of the loss in sensing is not

significant. A slight increase in the voltage difference between 0 and 5 gaps is due to numerical error. In the case of a large number of discontinuities (short fiber AFC) the sensing performance decreases rapidly with the increase in the number of gaps in fibers.

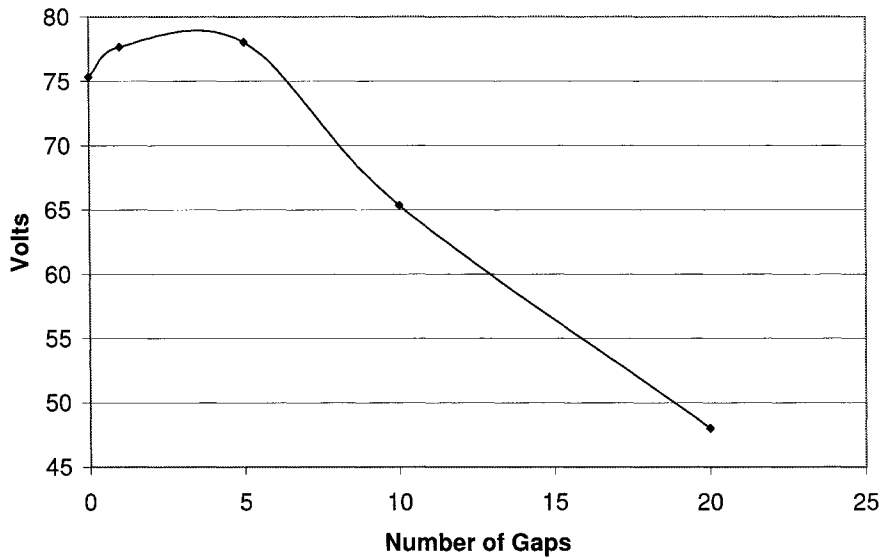


**Figure 5.18:** Simulated effect of non-continuous fully polarized fibers on the voltage produced by an AFC under applied deformation.

The effect of depolarization of the fiber near the gap is significant for sensing applications as seen in Figure 5.19-a. The results obtained in the sensing simulation indicate that the difference of electric potentials between the top and bottom surfaces of the AFC, in the proximity of the gap, drastically differs from the electric potential differences in other regions of the AFC.

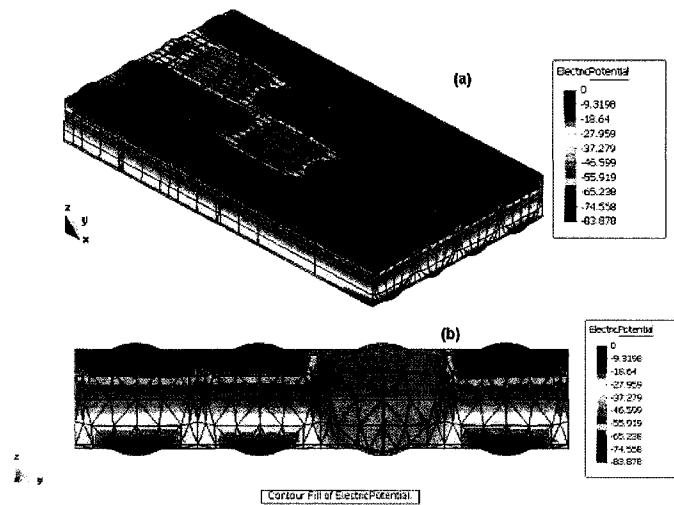


**Figure 5.19:** (a) AFC under an applied strain (b) AFC x-section near the gap.

Figure 5.19b shows a x-section of the AFC near the gap. As seen in this figure the electric potential difference near the gap is close to zero. This is a major point of concern since discontinuities in AFC tend to appear in the proximity of the electrodes. The electrodes would then sense an electric potential that is substantially less than the actual electric potential of the AFC. This would tend to indicate the need for dual electrode systems in sensing AFC. The first electrode group may be used for the creation of the polarization field through the piezoelectric fibers, while the second electrode would serve to monitor the electric potential distribution on the AFC under a specific strain condition. This second electrode group can then be compared to the first electrode group as a means of verification of the reading. Thus, the reliability of the piezoelectric AFC sensor could be validated and in the overall performance tracked for degradation.

Simulations where the polarization was set along the length of the fiber were also conducted. The simulations were carried out for an AFC with 1, and 2 gaps in the model. Figure 5-20 and

5-21 show the electric field on an AFC due to an applied strain for fibers with polarized and depolarized regions near the gaps and under the electrodes. As seen in these figures, the fibers that have a gap show a drop in the electric potential difference in comparison to the continuous fibers of the AFC for both fully polarized and depolarized regions in the fibers.

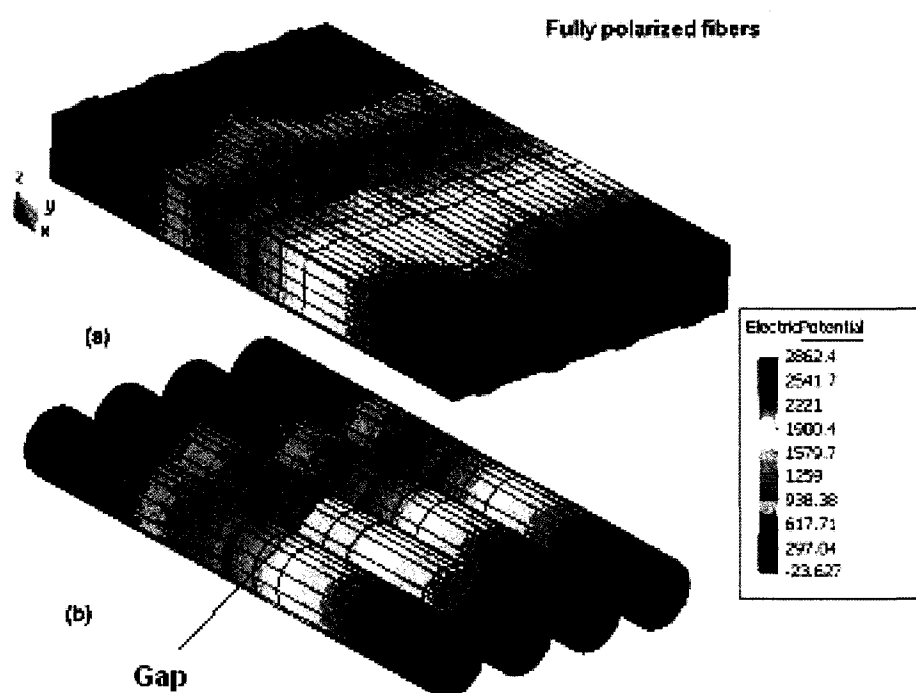


**Figure 5.20:** (a) AFC under an applied strain with fully polarized along the fiber length and 1 broken fiber. (b) AFC under an applied strain fully polarized along the fiber length and 1 broken fiber with a transparent epoxy matrix.

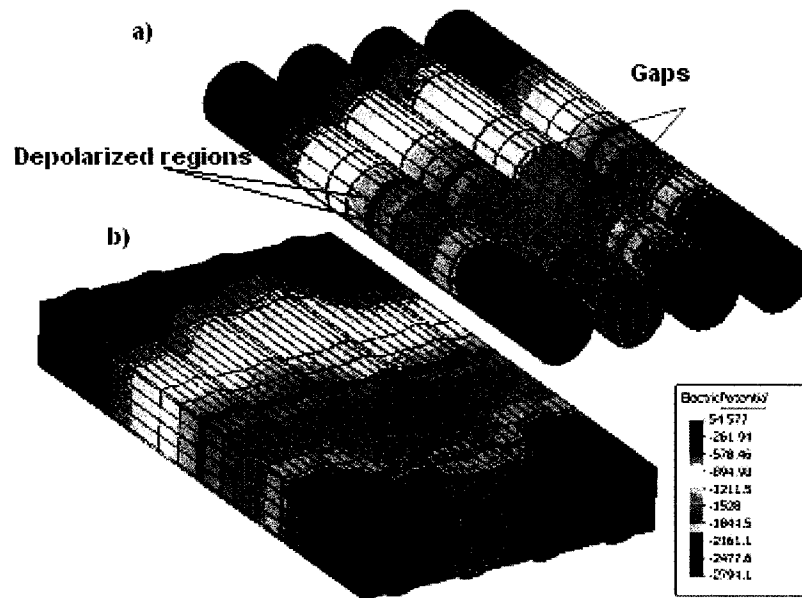


**Figure 5.21:** (a) AFC with 2 broken fibers and with depolarized regions at the gap interfaces with a transparent epoxy (b) AFC with 2 broken fibers and with depolarized region at the gap interfaces with the epoxy.

Table 5.6 shows the voltage difference along the broken and continuous fibers along the AFC for both polarized and depolarized regions in the fibers. In the case of the depolarized regions in the fibers the assumption that is made is that the depolarized region is one fiber diameter on each side of the gap interface. As seen in Table 5.6 for the fully polarized fibers with gaps, the voltage difference from opposite ends of the fiber decreases as the number of gaps are introduced into the system. It is also important to note that the difference between two fibers that have the same number of gaps is very similar (within 30 volts).

**Table 5.6:** Voltage difference along the AFC for piezoelectric fibers poled along the fiber length for polarized and depolarized fibers.

	<b>Polarized regions in fibers along the length of the fiber</b>	<b>Depolarized regions in fibers along the length of the fiber</b>	<b>Voltage difference between polarized &amp; depolarized regions</b>
<b>No. of Gaps</b>	<b>Voltage difference</b>	<b>Voltage difference</b>	<b>Voltage</b>
0+	2839.0	2789.0	50.0
0++	2832.0	2779.0	53.0
1	2442.0	2022.1	419.9
2 (1 <sup>st</sup> broken fiber)	2362.6	1884.8	477.8
2 (2 <sup>nd</sup> broken fiber)	2358.0	1913.5	444.5

+ Voltage on a continuous fiber in an AFC with 1 broken fiber

++ Voltage on a continuous fiber in an AFC with 2 broken fibers

The third column in Table 5.6, indicates the voltage difference for those fibers that have a depolarized regions on each side of the gap. The voltage difference for the fibers with depolarized regions is consistently lower than for fibers, which contain only gaps without depolarized regions. The comparison of continuous fibers in the AFC containing fibers with gaps with depolarized regions and continuous fibers in the AFC containing gaps in fibers without accompanying depolarized regions, demonstrates that the former produces a smaller voltage by approximately 50 Volts. For fibers containing gaps the introduction of depolarized region results in the decrease in the voltage by approximately 420 Volts (the presence of the gap itself without depolarized region reduces voltage by approximately 400 Volts compared to a continuous fiber). An addition of a second gap into the AFC results in the further decrease of the voltage in the broken fibers by 80 Volts in the system without depolarized regions and by 140 Volts in the system with gaps in fibers accompanied by depolarized regions. These results indicate that the voltage loss, due to the presence of a gap, and the depolarized region at the interfaces of the gap in sensing applications can be significant. These results also indicate that for the analysis of the effect of damage in fibers on sensing performance it is important to take

into account the actual size of gaps in fibers and possible existence of regions with changed polarization.

### 5.2.5 Unconstrained AFC with broken fibers model under shear actuation

The shear actuation simulations were run on the FEM model of an unconstrained AFC with broken fibers which was also used for the simulation of sensing tests (Section 5.2.4). The electric potential was set to 1,000V along the complete top surface of the AFC and 0V along the bottom surface. The top and bottom layers of the AFC were set to be of Kapton material. Figure 5.22 shows a render picture of the AFC.

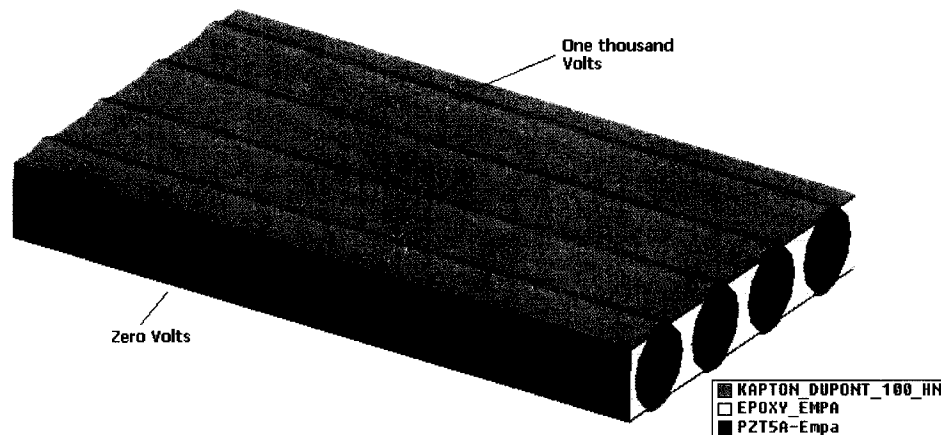
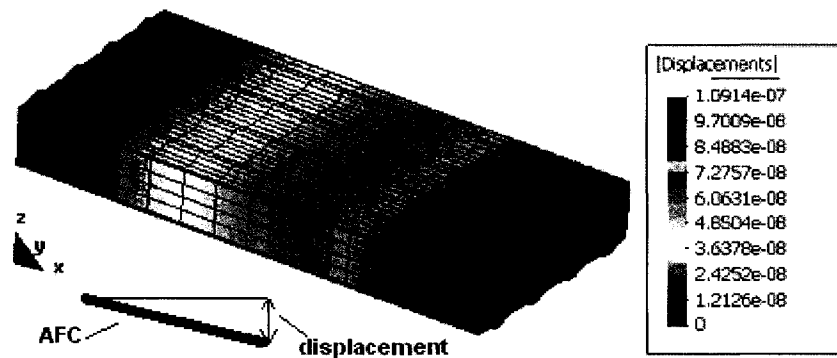


**Figure 5.22:** Applied electric potential on AFC for shear actuation.

Under shear deformation the IDE was not modeled and the complete upper and lower Kapton layers of the AFC were assigned electric potentials of 1,000V and 0V respectively. This

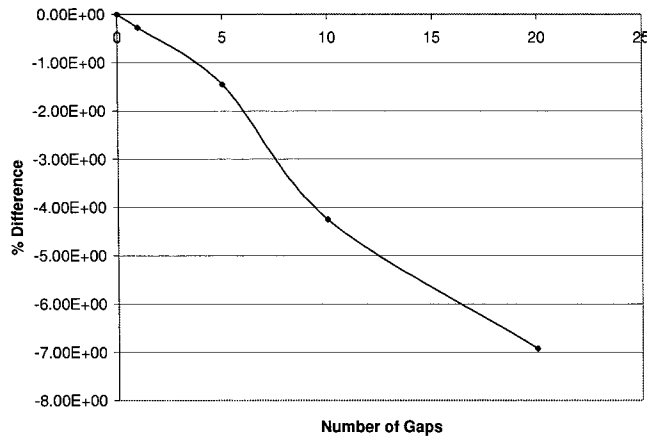
creates an electric field through the fiber that causes a shear deformation of the AFC. The fibers were set to have a polarization vector along the fiber length.

Figure 5.23 show the displacement field of an AFC with continuous fiber under the applied voltage.



**Figure 5.23:** AFC displacement field, deformed in shear due to an electric field across the fiber diameter.

Figure 5.24 shows the percentage difference in shear actuation for an AFC that has no gaps to an AFC that has up to 20 gaps. In this case the simulations were carried out for fibers with fully polarized regions. As seen in Figure 5.24, the loss of performance due to the presence of gaps is not significant in comparison to the effect in extension actuation and sensing tests. This is due to the fact that the electric field is through the fiber diameter and not along the length of the fiber, as in the case of the extension model described above. Thus, shear actuation is more “forgiving” when non-continuous fibers are used.



**Figure 5.24:** Shear deformation displacement vs. gap fiber presence along the fiber length.

### 5.2.6 Bi-layer AFC-GFRP system

The focus of this simulation is to demonstrate the effect of the extension of an AFC on GFRP beam. This simulation was carried out with 20-node brick elements. The figure below shows the bending effect of the beam. Twenty node brick elements were used in order to avoid the locking effect of 8-node brick under bending conditions. The use of 8-node brick would require a greater number of elements than the one allowed by our FEM solver as was demonstrated in Chapter 4.

Figure 5.25 shows the displacement field in bending due to the extension of an AFC on a GFRP beam of similar thickness.

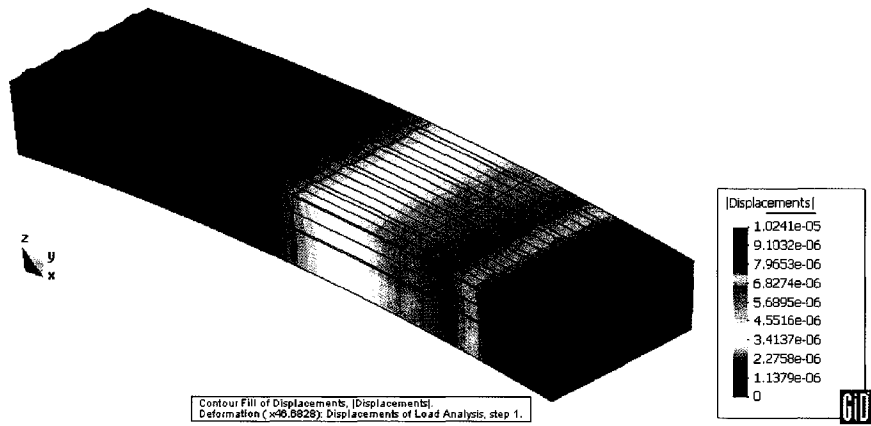


Figure 5.25: Displacement field of AFC on a GFRP beam at a 900V.

Figure 5.26 shows the applied voltage in order to obtain the bending of the beam.

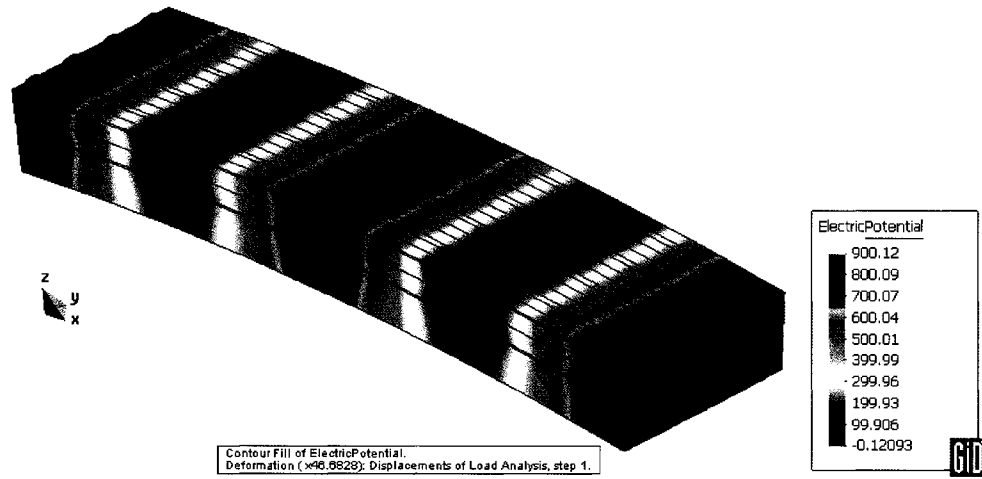
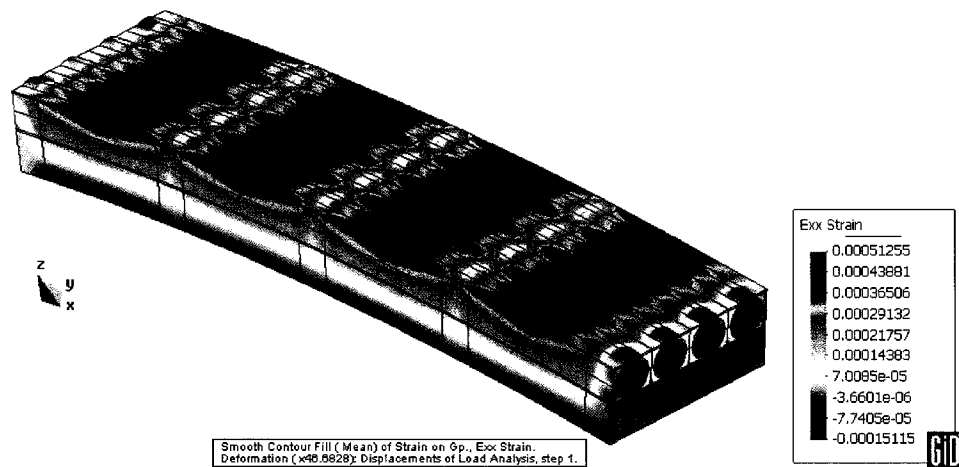


Figure 5.26: AFC on a GFRP at 900V electric potential field.

Figure 5.27 shows the strain  $\epsilon_{xx}$  produced due to the bending of the structure.



**Figure 5.27:** Strain,  $\epsilon_{xx}$  of AFC on beam.

### 5.2.7 Analytical model for the deformation of bi-layer system

The following section describes the analytical equations for the bi-layer AFC-GFRP specimen [5]. The basis of this theory consists of describing the bending of a lamella when a voltage is applied to the AFC. The AFC is assumed to be perfectly adhered to the lamella as shown in Figure 5.28. The analytical model assumes an isotropic elastic beam (since we have modeled a GFRP plate we are assuming the homogenized version of the composite). The third assumption is that the strain distribution in the AFC is linear and has a constant slope. It is also assumed that both the AFC and the lamella are thin and finally that the piezoelectric material constant  $d_{33}$  is much greater than  $d_{31}$ .

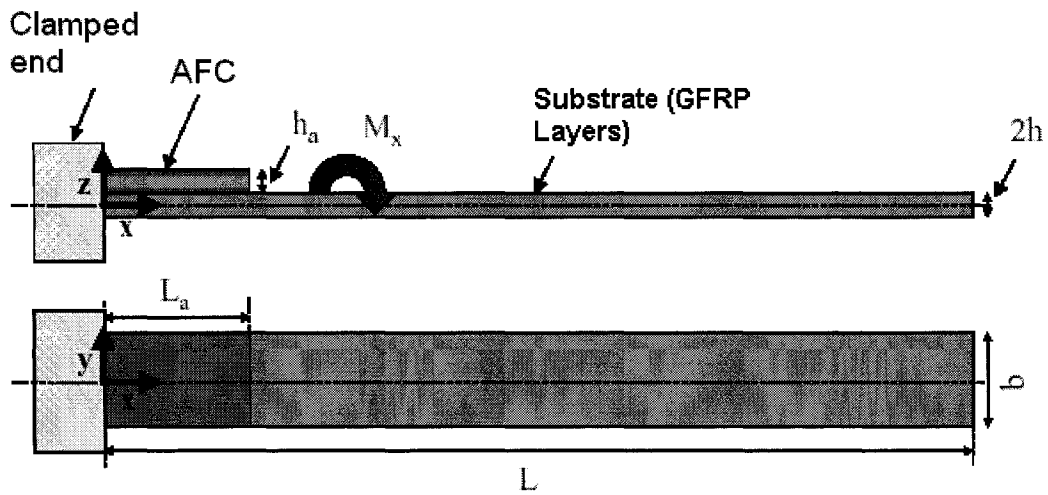


Figure 5.28: AFC on a lamella [5].

The stress/strain state in the lamella is described by equation 5.1 and 5.2:

$$\varepsilon_{x(z)} = Cz \quad (5.1)$$

where,

- $C$  is obtained by multiplying the overall lamella stiffness with the AFC strain
- $z$  is the coordinate direction through the AFC and lamella.

$$\sigma_{x(z)} = YCz \quad (5.2)$$

where,

- $Y$  is the Young's Modulus of Elasticity of the lamella.

Similarly, the piezoelectric longitudinal strain (unconstrained) in the AFC is given by equation 5.3 and 5.4

$$\epsilon_a = \frac{d_{33} \cdot U_e}{s} \quad (5.3)$$

where,

- $U_e$  describes the voltage at the electrodes of the AFC
- $D_{33}$  is the piezoelectric constant of the piezoelectric fibers
- “ $s$ ” is the inter-digitized spacing

The stress of the actuator is:

$$\sigma_{a(z)} = Y_a \cdot (Cz - \epsilon_a) \quad (5.4)$$

where  $C$ , is defined by equation 5.6.

The Moment of equilibrium at the center of the beam is provided by equation 5.5:

$$\int_{-h}^h \sigma_{(z)} z dz + \int_h^{h+h_2} \sigma_{a(z)} z dz = 0 \quad (5.5)$$

From equation 5.5,  $C$  can be found as:

$$C = K_f \epsilon_a \quad (5.6)$$

where,

$$K_f = \left( \frac{h_a}{2hh_a + h_a^2} \right) \cdot \left( 2 - \frac{\frac{2}{3}YY_a hh_a^3 + \left( \frac{16Y^2}{3} \right) h^4 + \frac{1}{3}Y_a^2 h_a^4 + \frac{8}{3}YY_a h^3 h_a}{\frac{Y_a h^4}{6} + \frac{8}{3}Y^2 h^4 + \frac{4}{3}YY_a (4h^3 h_a + 3h^2 h_a^2 + hh_a^3)} \right) \quad (5.7)$$

where,

- $h$  is the height of the lamella
- $h_a$  is the height of the AFC
- $Y_a$  is the homogenized Young's modulus of the AFC.

The piezoelectric moment  $M_x$  induced into the Beam by the AFC is calculated as:

$$M_x = YIK_f \varepsilon_a \quad (5.8)$$

Where

- $I$  is the moment of inertia  $bh^3/12$ .

The displacements and strains in the beam are given by the following equations:

$$[u_{(z)}] = \left[ -z \frac{\partial w}{\partial x} \quad -z \frac{\partial w}{\partial y} \quad w \right]^T \quad (5.9)$$

$$[\boldsymbol{\varepsilon}_{(z)}] = \left[ -z \frac{\partial^2 w}{\partial x^2} \quad -z \frac{\partial^2 w}{\partial y^2} \quad 2z \frac{\partial^2 w}{\partial x \partial y} \right]^T \quad (5.10)$$

Where,

- $w$  is the flexural displacement.

The internal beam bending moment is calculated using equation 5.11:

$$M_{x(x)} = \int \sigma_{(z)} z dz = -YI \frac{\partial^2 w}{\partial x^2} \quad (5.11)$$

The boundary conditions are set by equation 5.12, due to the clamped end shown in Figure 5.28:

$$\begin{aligned} w(0) &= 0 \\ \left( \frac{\partial w}{\partial x} \right)_0 &= 0 \end{aligned} \quad (5.12)$$

The flexural displacement is obtained from equation 5.8, 5.11 and 5.12. The flexural displacement as a function of  $x$  (coordinate along the length of the lamella) is:

$$w(x) = \frac{-K_f \varepsilon_a x^2}{2} \quad (5.13)$$

Figure 5.29 shows the constant slope that the lamella would take in this theoretical model past the AFC length. The flexural displacement of the lamella would be of the form of:

$$w(x) = Ax + B \quad (5.14)$$

where  $A$  is defined as:

$$\left(\frac{\partial w}{\partial x}\right)_{L_a} = -K_f \varepsilon_a L_a = A \quad (5.15)$$

and  $B$  is defined as:

$$B = w_a - AL_a = w_a - K_f \varepsilon_a L_a^2 \quad (5.16)$$

Thus, the maximum deflection of the beam would be given by equation 5.17

$$w_{\max} = K_f - \varepsilon_a L_a L + w_a - K_f \varepsilon_a L_a^2 \quad (5.17)$$

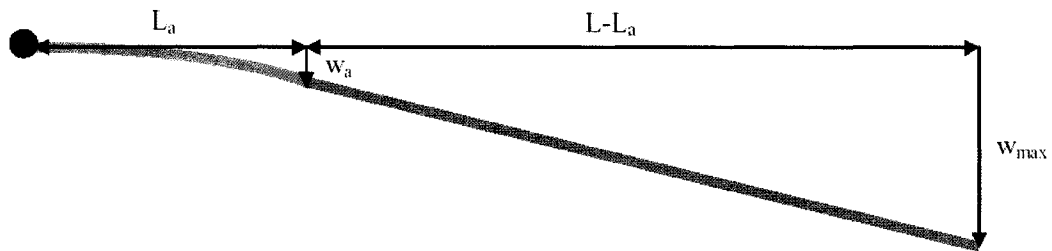


**Figure 5.29:** Maximum deflection of an AFC on a Lamella [5].

The  $w_{\max}$  obtained by our FEM solver on the Bi-layer AFC-GFRP System, with respect to the analytical equations described above, show an error of 17%. This error is mostly due to the assumptions that the strain distribution in the AFC is linear and has a constant slope, which clearly it is not, as seen in the FEM model.

### 5.2.8 End constrained AFC

A set of simulation runs that caused the AFC to contract under the influence of an electric potential, pulling on a section of GFRP were performed. The simulation consisted in having a cantilevered AFC contract due to an applied electric voltage attached to a section of GFRP that was also cantilevered. As the AFC contracted due to the applied voltage it caused a pull on the GFRP section of the beam. The potential of GFRP section of the structure was set to zero volts. The results of these simulations are presented next. Figure 5.30 shows the application of the electric potential on the AFC.

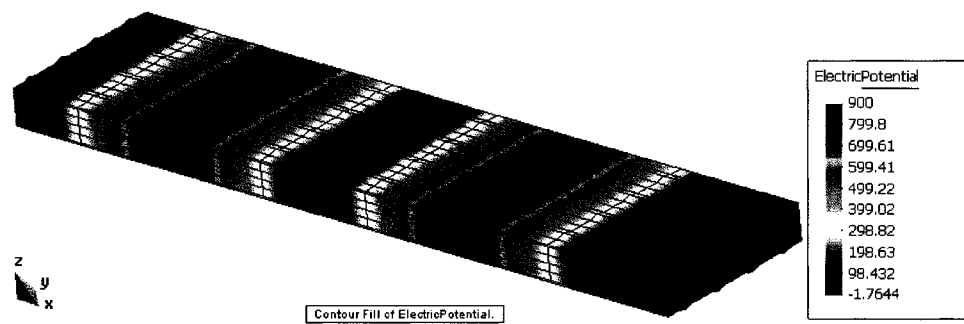
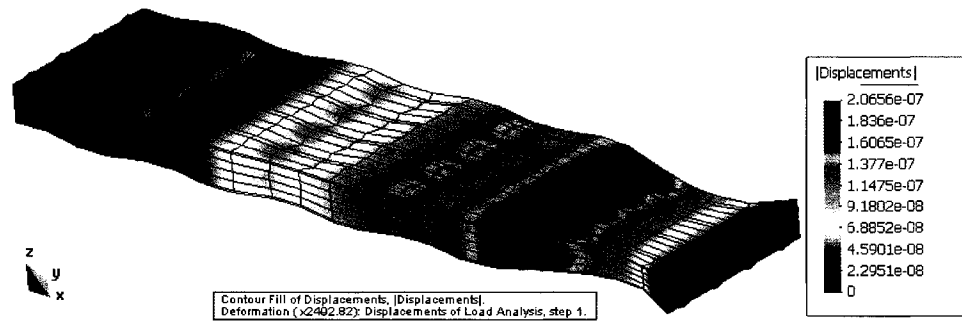


Figure 5.30: AFC pulling on GFRP X-Section.

The polarization of the fibers was set, as shown in Figure 5.4. The electric potential was started with electrode *E1* set to 0V instead of 900V. The result of this change in voltage is a contraction effect on the AFC (the polarization vector remained the same as shown in Figure 5.4). Both ends of the AFC were set to zero displacement in all directions. The displacement at the interface of the AFC and the GFRP section was analyzed. The value of displacement at

this interface was taken at the fiber and not at the epoxy layer. The results on displacement are show in the figure 5.31.



**Figure 5.31:** Displacement field on the deformed mesh.

The displacement field taken at the fiber interface with the GFRP, was obtained from the results provided by the solver. The result of displacement as a function of the number of gaps was graphed in the figure below. As seen Figure 5.32, it can be concluded that the effect of a single gap in the fiber has little degradation effect on the ability of the AFC to contract and pull on the GFRP cross section. As the number of gaps in the fiber increases in the model the strain/displacement dropped linearly between 1 and 10 gaps.

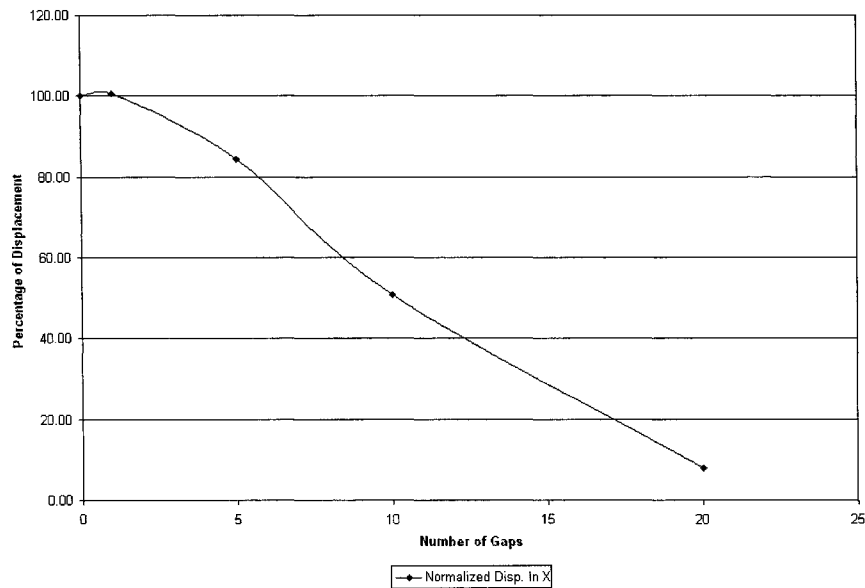


**Figure 5.32:** Effect of non-continuous fibers on displacement of the GFRP beam section.

### 5.3 AFC homogenization

The analysis of piezoelectric fiber composites in a large system requires the use of finite elements that have the same average properties as the AFC. None of our simulations make use of this type of element. In our simulations every fiber was modeled in detail. This provides a limitation on the number of fibers that can be modeled due to the memory consumption in solving large AFC systems. In order to develop 8 and 20-node brick elements with the same properties as an AFC, a represented volume element (RVE) as the one shown in Figure 5.33 can be modeled. The RVE is presented in this thesis as future work that can be performed to optimize the capabilities of our solver.

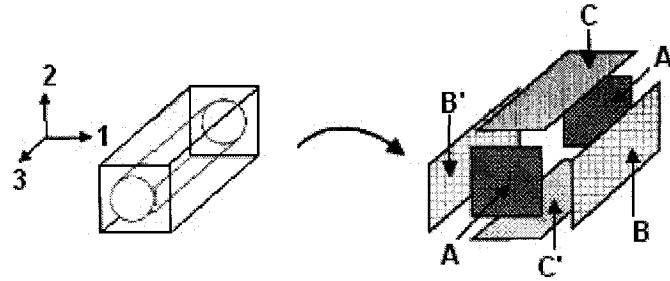


**Figure 5.33:** RVE of an AFC [14].

The RVE consists in a unit cell of the structure that is being considered. For every type of AFC an RVE would be required, since any change in the fiber diameter will have an impact on the volume fraction of the AFC. Changes in volume fraction have an effect on the effective material coefficients calculated.

**Table 5.7:** Shows boundary conditions applied to the RVE in order to compute the effective material properties of the AFC unit cell. [14].

Constant	Forces Direction	Electrical Field direction	Calculation	Electrodes
$S_{11}^{E\text{eff}}$	1	....	$S_1/T_1$	....
$S_{12}^{E\text{eff}}$	2	....	$S_1/T_2$	....
$S_{13}^{E\text{eff}}$	3	....	$S_1/T_3$	....
$S_{33}^{E\text{eff}}$	3	....	$S_3/T_3$	....
$S_{44}^{E\text{eff}}$	3	....	$S_4/T_4$	....
$S_{66}^{E\text{eff}}$	1	....	$S_6/T_6$	....
$d_{31}^{\text{eff}}$	....	3	$S_1/E_3$	A, A'
$d_{33}^{\text{eff}}$	....	3	$S_3/E_3$	A, A'
$d_{15}^{\text{eff}}$	3	....	$D_1/T_5$	....
$\epsilon_{11}^{T\text{eff}}$	....	1	$D_1/E_1$	B, B'
$\epsilon_{33}^{T\text{eff}}$	....	3	$D_3/E_3$	A, A'

In order to determine the effective material property for an AFC, a series of finite element simulations on the unit cell model are required. The boundary conditions for each simulation on the unit cell are found in Table 5.7. In Table 5.7,  $S_x$  represents the strain,  $T_x$  the stress,  $D_x$  the electric displacement and  $E_x$  the electric field in the RVE.  $S_{xx}^{E\text{eff}}$  represents the effective elastic constants,  $d_{xx}^{\text{eff}}$  the effective piezoelectric constant and  $\epsilon_{xx}^{\text{eff}}$  the effective permittivity constant.

In order to compute the  $S_{11}^{E\text{eff}}$  a force in the direction of 1 is applied to the unit cell (Figure 5.33). The stress is calculated by dividing the force applied by the surface area of the plane normal to coordinate direction 1. The overall displacement is obtained from the FE solver. The value of  $S_{11}^{E\text{eff}}$  in the 1 direction can be computed by dividing the overall strain in 1 by the overall stress in 1. The calculation column in Table 5.7 indicates that the calculation performed ( $S_1/T_1$ ) in order to obtain the  $S_{11}^{E\text{eff}}$  constant with a constant electric field (E).

As the volume fraction of the RVE is decreased the effective material properties computed approximates that of the epoxy, while as the volume fraction of the fiber (PZT-5A) increases the effective material properties approach that of the fiber material (PZT-5A). A similar approach is used in order to obtain the other material properties.

The method described above is an effective method for obtaining all effective constants for a represented volume element. This method requires the use of FEM to obtain the effective properties. Analytical equations presented in [15,16] provide the equations to calculate the relationship between the effective properties of the piezoelectric composites by means of the

fiber volume fraction and material properties. The use of analytical equations in [15,16] does not allow obtaining every effective property, but it is a simpler means of obtaining some of the effective properties of the AFC element.

#### 5.4 References for Chapter 5

- [1] R. Sridhar, Thirupathi, P. Seshu, and Nagi G. Naganathan, A finite element static analysis of smart turbine blades, *Smart Materials and Structures*, Vol 6, 607-615, 1997.
- [2] M. Martinez, M. Melnykowycz, A. Artemev, F. Nitzsche, Finite Element Analysis of Actuated Fiber Composites, *Cansmart 2005, International Workshop, Smart Materials and Structures*, 13 - 14 October 2005, Toronto, Ontario, Canada, (2005) 231.
- [3] M. Martinez, A. Artemev, F. Nitzsche, B. Geddes, Finite Element Modeling of Actuated Fibre Composites, accepted for publication in Conference proceeding for HSPM 2006, Ostend-Belgium May 3-4, 2006.
- [4] Roman Solecki, R. Jay Conant, *Advanced Mechanics of Materials*, New York, Oxford University Press, 2003.
- [5] EMPA Internal Report: EMPA, Abteilung: Kunststoffe/Composites Seite 10 von 85  
Auftraggeber: EMPA Abt. 114 Bericht-Nr. 880'075.
- [6] Benedetto Castelli, Ph.d Thesis, Modeling and Characterization of Active Fiber Composites, Diploma Thesis at the Centre of Structure Technologies, Institute of Mechanical Systems, Department of Mechanical and Process Engineering, ETH Z"urich, Prof.Dr.Paolo Ermanni in cooperation with EMPA D"ubendorf, IMES Ref.-Nr: 08-183.
- [7] Email correspondence between M. Martinez and Mark Melnykowycz  
[Mark.Melnykowycz@empa.ch](mailto:Mark.Melnykowycz@empa.ch) (2005).

- [8] Melnykowycz M., et al., Performance of Integrated Active Fibre Composites in Fibre Reinforced Epoxy Laminates. to appear in Smart Materials Structures, 2006.
- [9] Viresh K Wickramashinghe, Nesbitt W Hagoood, Material Characterization of active fiber composites for integral twist-actuated rotor blade application, Smart Material and Structures, 13, (2004) 1155-1165.
- [10] Robert D. Cook, David S. Malkus, Michael E. Plesha, Concepts and Applications of Finite Element Analysis, 3<sup>rd</sup> Edition, Published by John Wiley & Sons 1989.
- [11] Goldak, "Piezoelectric Formulation" Course Notes for Prof. Goldak Finite Element II course, Carleton University, Dept. of Mechanical and Aerospace Engineering, 2003.
- [12] O.C. Zienkiewicz, K. Morgan, Finite Elements and Approximation, John Wiley and Sons, 1983.
- [13] [www.efunda.com](http://www.efunda.com) (Last accessed on February 4-06).
- [14] Anne-Christine Hladky-Hennion and Jean Cladue Debus, Numerical homogenization techniques applied to piezoelectric composites, J. Acoustical Society of America, February 2003, Pages 826-833.
- [15] K. Schulgasser, Relationship between the effective properties of transversely isotropic piezoelectric composites., Pergamon Press 1992, J. Mech. Phys. Solids vol 40 No. 2, pp. 473. 479, 1992.
- [16] K. Shculgasser, CE-Wen Nan, Comment on "Relationship between the effective properties of transversely isotropic piezoelectric composites", J. Mech. Phys. Solids Vol 40, 473-479.
- [17] S. Semenovskaya, A.G. Khachaturyan, *J. Appl. Phys.*, 83 (1998) 5125.

## DISCUSSION AND CONCLUSIONS

### **6.0 Discussion and Conclusions**

The FEM solver for the analysis of structures with piezoelectric components has been developed. The solver was tested for elastic and piezoelectric problems and very good agreement between the numerical solutions produced by the solver and analytical results was demonstrated. For elastic problems the relevant tests from MacNeal and Harden test set [4] were used. The validation of the solver for piezoelectric problems was performed using simple systems for which analytical solutions are available [5, 6]. The results of the elastic tests indicate that while 8-node brick elements can provide a good accuracy in simple extension tests, but they are not efficient for the solution of the problems in which deformation produces any significant curvature effect. For example, a simple bending test demonstrated that we need 1,200 8-node brick elements to approach a reasonable level of accuracy (error within 13%) while just 6 20-node brick elements provided a very accurate solution (error within 3%). These results agree with literature [7]. Even though that 20-node bricks require more resources per element, they can be more efficient for the solution of problems where deformation produces significant curvature. From these results it can be concluded that it is better to use 20-node brick elements whenever possible and that when using 8-node brick elements it is necessary to add sufficient 8-node brick elements in order to guarantee mesh convergence. In other words

a mesh convergence test when using 8-node brick elements is required in order to feel confident with the obtained solution.

The FEM solver was also validated using experimental results obtained for Actuated Fibre Composites (AFC) by Swiss Federal Laboratories for Materials Testing and Research (EMPA). The very good agreement between experimental results and simulation results for actuation tests was obtained [1,2]. Problems with non-linearity at high voltages were shown, due to the non-linear behaviour of piezoelectric materials at high electric fields [3]. In order to represent accurately these non-linearities a non-linear solver is required. The AFC strains obtained under the applied voltages in experiments with both free AFC and AFC constrained in AFC-GFRP symmetrical laminate are very close to the computed strain values produced by our solver. All of the results agreed within 5% of experimental results for different actuation voltages. In the case where the actuation voltage (10 kV/cm) was lower, the results were within 1% of the experimental value. The higher errors at higher voltages (20kV/cm) can be attributed to the non-linear behavior of piezoelectric materials, as described in [3]. Thus, it was shown that the developed FEM solver could be used to model the actuation performance of AFC for both constrained (laminated) and un-constrained systems.

The structure with AFC applied as an actuator to the surface of elastic beam was also simulated and obtained results were compared to analytical solution [5,9]. The results indicate a difference of approximately 17% between the analytical and FEM models. It is necessary to note that in the analytical model the number of simplifications made (the AFC is replaced by the homogeneous piezoelectric material and piezoelectric constants of this effective replacement

are approximated by the corresponding values of the AFC fiber materials and are not obtained through the proper analysis of the representative volume element) and the analytical results themselves are only approximate. The use of AFC as actuators applied to elastic beams is currently being researched for rotor blade applications being developed with the purpose of the control of the blade vortex interaction phenomena common in helicopters [8,9].

Analysis of the effect of discontinuities in fibers on the performance of AFC systems was performed using our FEM solver. The results demonstrate that the transition from a continuous fiber AFC (or long fiber AFC) to a short fiber AFC can result in a significant degradation of both the actuation and sensing capabilities when AFC operates in the extension mode. In particular, such degradation can be the result of the fiber damage produced by the excessive mechanical deformation of AFC. Experimental results show that mechanical straining of AFC results in a large decrease in the sensing performance [10]. The range of degradation values obtained in these experiments is the same as the one obtained in our simulations for AFC with different number of fibers in the systems. The maximum degradation of about 80% was obtained experimentally. It is necessary to note that our simulations indicate that such degradation can be obtained from the gaps in fibers only when a very large number of gaps is formed and material is effectively transformed into short fiber composite. It is unlikely that such severe damage can be achieved without producing an overall failure of composite. Thus, it is possible to suggest that some additional mechanisms (other than just formation of gaps in fibers, such as for example the change of the polarization state in fibers near the gaps) can provide contributions into the degradation of the AFC performance.

It is possible that the formation of gaps is accompanied by local changes to the polarization state resulting from the depolarizing field near the gap and the strain effect on the domain structure. Such changes of polarization can attenuate the degradation of performance produced by the defects in fibers. The FEM analysis was performed for AFC with broken fibers depolarized regions near the gaps in the fibers. It was assumed that the length of such depolarized regions is equal to one fiber diameter at each side of the gap. Our simulations demonstrate that when AFC is used as an actuator in the extension mode the addition of depolarized region to gaps in fibers produces almost no change in the performance of AFC. We observed that once the gap is formed in the fiber the whole length of the fiber between to adjacent electrodes is effectively switched off and any further changes in this section of the fiber produce very little or no effect. In case of the sensing application of the AFC the addition of depolarized regions to the gaps in fibers produces very significant effect on the performance of AFC. Our results show that the addition of depolarized regions to gaps can increase the degradation of sensing performance by up to two times.

Recent experimental observations produced by EMPA demonstrate that these gaps in fibers appear predominantly near the electrodes when the AFC are put under large mechanical strains. Our simulations for AFC with fibers poled along the fiber diameter demonstrate that the electric potential difference near such gaps can be significantly reduced (almost to zero) if depolarization region is added to the gap. If the narrow gap (gap length much smaller than the diameter of the fiber) is formed without depolarized region it produces very little effect on the voltage developed in such AFC. Thus, the possibility of the depolarization effect near the gaps in fibers can be very important if the AFC with these type of poling is used for sensing. In

particular, it can require dual electrode system to validate the strain measurements. Of course, the extent of the gap effect on the polarization state (the length of depolarized region) is very important parameter that is not well defined at the present time. Further studies are being carried out in order to understand the size of the depolarized regions due to the size of the gap.

AFC with the shear mode of actuation was also analyzed. It was shown that the loss of actuation performance, due to the presence of gaps, is not as significant in the case of shear actuation as in the case of the extension actuation. This is due to the fact that the electric field is through the fiber diameter and not along the length of the fiber, as in the case of the extension model. Thus, shear actuation is more “forgiving” when non-continuous fibers are used or when significant amount of damage can be produced in fibers. These results could serve useful when proposing the use of AFC for “Smart Blades” in rotor wing aircrafts [8,9].

The degradation of the actuation performance of AFC by broken fibers when it is used as component in elastic structure can be resulting from two factors: the loss of effective piezoelectric constants of AFC materials and the loss of stiffness. The results obtained in the simulation of the actuation of unconstrained AFC (section 5.2.3) and end constrained AFC (section 5.2.8) can be used to estimate the relative importance of these two factors. If the loss of stiffness produces significant effect then a larger effect of broken fibers should be observed in the end-constrained system than in the unconstrained AFC.

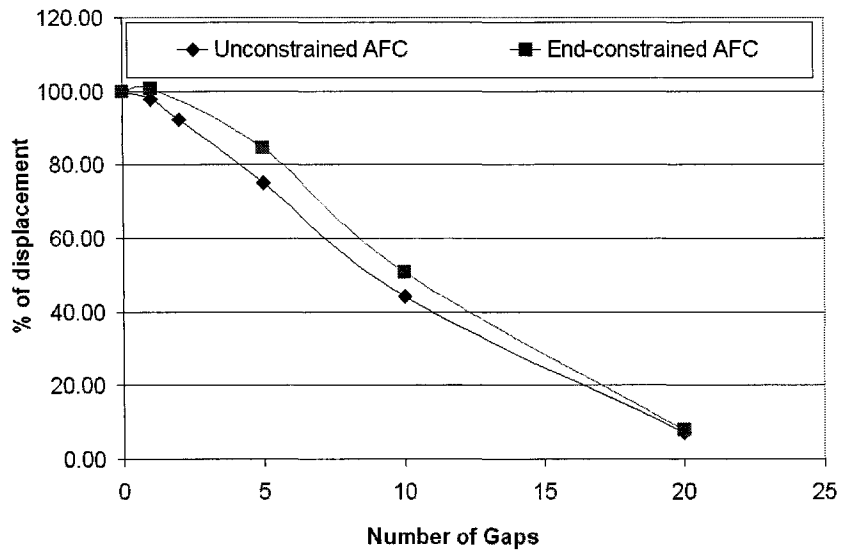


**Figure 6.0:** Normalized AFC extension and contraction displacement vs. the number of gaps.

Figure 6.0 shows the displacement obtained in AFC systems (unconstrained and end constrained) with different number of gaps and fibers as percentage of displacements obtained in systems with continuous fibers (100% represents displacement in system with continuous fibers). The results indicate that the loss of performance is very similar (and the difference is within expected error of our method) both for free strain and for the end constrained AFC model. Thus, these results suggest that the loss of performance is mostly due to the loss of piezoelectric constants and not to the decrease in effective stiffness.

## 6.1 References of Chapter 6

- [1] M. Martinez, M. Melnykowycz, A. Artemev, F. Nitzsche, Finite Element Analysis of Actuated Fiber Composites, Cansmart 2005, International Workshop, Smart Materials and Structures, 13 - 14 October 2005, Toronto, Ontario, Canada, (2005) 231.
- [2] M. Martinez, A. Artemev, F. Nitzsche, B. Geddes, Finite Element Modeling of Actuated Fibre Composites, Conference proceeding for HSPM 2006, Ostend-Belgium May 3-4, 2006.
- [3] Thomas R. ShROUT, Relaxor based ferroelectric single crystals for electro-mechanical actuators, Springer-Verlag 1997.
- [4] Richard H Macneal and Robert L. Harder, A proposed Standard Set of Problems to test finite element accuracy, The MacNeal Schwendler Corporatinos, 815, Colorado Boulevard, Los Angeles, CA 90041, USA.
- [5] Roman Sulecki, R. Jay Conant, Advanced Mechanics of Materials, New York, Oxford University Press, 2003.
- [6] Nye, "Physical Properties of Crystals", Oxford University Press, Amen House, London E.C.4. 1964.
- [7] J.M.J. McDill, K.H. Runnemalm, A.S. Oddy, An 8- to 16-Node Solid Graded Shell Element for Far-Field Applications in Adaptive 3-D Thermal-Mechanical FEA, Mathematical Modeling and Scientific Computing Vol 13., No. 3, pp. 177-190, Principia Scientia 2001.

- [8] M. Melnykowycz, M. Martinez, F. Nitzsche, M. Barbezat, A. Artemev, Active Airfoil Design and Finite Element Analysis of Smart Structures for Rotor Blade Applications, ICAST Conference proceedings, Paris 2005.
- [9] Viresh K Wickramasinghe, Nesbitt Hagood, Material Characterization of Active Fiber Composites for Integral Twist-Actuated Rotor Blade Applications, Smart Material Structures, 13, (2004) 1155-1165.
- [10] M. Melnykowycz, et al., Performance of Integrated Active Fibre Composites in Fibre Reinforced Epoxy Laminates. to appear in Smart Materials Structures. 2006.